Morphological coupling in a double sandbar system

Morfologische koppeling in een systeem van twee zandbanken

(met een samenvatting in het Nederlands)

P R O E F S C H R I F T

ter verkrijging van de graad van doctor aan de Universiteit Utrecht
op gezag van de rector magnificus, prof.dr. G.J. van der Zwaan,
ingevolge het besluit van het college voor promoties in het openbaar te verdedigen

op vrijdag 15 februari 2013 des middags te 2.30 uur

door

Timothy David Price

geboren op 2 juli 1982 te Utrecht

Promotor:
Prof.dr. P. Hoekstra

Co-promotor:
Dr. B.G. Ruessink

Morphological coupling in a double sandbar system

Utrecht Studies in Earth Sciences

ISSN 2211-4335

Utrecht Studies in Earth Sciences 029

Morphological coupling in a double sandbar system

Timothy D. Price

Utrecht 2013

Department Physical Geography
Faculty of Geosciences - Utrecht University

Promotor
Prof. dr. P. Hoekstra

Co-promotor
Dr. B.G. Ruessink

Examination committee
Dr. B. Castelle, University of Bordeaux 1
Prof. dr. G. Masselink, Plymouth University
Prof. dr. ir. J.A. Roelvink, Delft University of Technology
Prof. dr. ir. M.J.F. Stive, Delft University of Technology
Prof. dr. H. de Swart, Utrecht University

This work was financially supported by the Netherlands Organisation for Scientific Research (NWO) under contract number 818.01.009.

ISBN 978-90-6266-321-7

Cover: Sandbars and rip channels at Zarautz, Spain. Photograph by Timothy Price.

Printed in the Netherlands by WPS, Zutphen.

Contents

Preface

My fascination for coasts, and sandbars in particular, stems from the combination of spending numerous days off at the beach among the breaking waves, while studying coastal processes during my Master's degree in Physical Geography. After graduating, I decided to pursue this interest by applying for a PhD position resulting from Gerben Ruessink's proposal on crescentic sandbar behaviour being granted. I was chuffed to get the position, and the four years that followed are now condensed into this thesis. This period would certainly not have been the same without the many people who crossed my path on the way, and I would like to thank those who contributed either directly or indirectly to the realisation of this thesis.

Of the people directly involved, I first and foremost want to thank my co-promotor and daily supervisor Gerben Ruessink. Gerben, your well-balanced guidance and genuine enthusiasm provided me with the best imaginable backdrop throughout my research. I learnt a lot from you during the past 4 years. Thank you for giving me enough freedom to wander off into the unknowns of nearshore science (at least, unknown to me), while supplying me with the necessary deadlines, and extensions thereof. I would like to thank my promotor Piet Hoekstra for his advice, his constructive feedback on the manuscript of my thesis and, above all, his ability to get straight to the point. Part of my PhD involved a 6-month stay at the Université de Bordeaux 1, during which I had the opportunity to work with Bruno Castelle on the numerical modelling of sandbar behaviour. Bruno, the combination of your common sense approach, based on your own field observations, and morphodynamic modelling were truly refreshing. Thank you for introducing me to the (almost) unlimited possibilities of your model, your unlimited help, and your advice in my research. Philippe Bonneton, thank you for welcoming me into the METHYS team. Furthermore, I thank Ap van Dongeren for providing and helping out with the XBeachWizard code, Robert McCall for the XBeach support and our irregular outings, Martijn Henriquez for the help on quantifying cell-circulation patterns and his insightful conversations, and Rosh Ranasinghe for his constructive feedback and input for Chapter 4 of this thesis.

The research field of nearshore video monitoring would not have got as far as it is without the pioneering work of Rob Holman, and the ongoing efforts of everyone involved in the Argus program. I am grateful to Rob Holman for instigating the Argus workshops and continuing to push the limits of Argus. I much enjoyed the workshops in Plymouth and Corvallis and, for me, these workshops were the most valuable get-togethers during my PhD period. I wish to thank the Gold Coast City Council for funding support that enabled the operation of the Argus station at the northern Gold Coast, and Ian Turner for providing the Gold Coast wave, water-level and Argus data.

My direct working environment over the past 4 years in room 204 of the Zonneveld-vleugel would not have been the same without my room-mates. During the first year

of my research, Leo Pape immediately set me off in the right intellectual and scientific direction. Leo, your constant feed of stimulating discussions on all sorts of topics and your legacy of Matlab tools (BLIM toolbox!) and written materials continued to inspire me throughout my research. For two and a half years I shared my office with Florent Grasso, whose charisma and highly-structured approach to research I much appreciated. Florent, we had a great time playing football on Thursdays, going to the beach for some surf, having a BBQ in my garden, re-organising hotel rooms during conferences, and trying to improve my French. Merci pour tout, mon pote! Many thanks to Jantien Rutten, who during her BSc performed part of the analysis leading to Chapter 3 of this thesis. I thank Quentin Quera for sharing his creative ideas, Florin Tătui for his modesty and amusing stories, and Florine Gongriep for bringing extra cheer to the office during the final months of my research.

The coastal research group within the department of Physical Geography in Utrecht formed a comfortable working environment. I would like to thank my (former) colleagues Marion Tissier, Renske de Winter, Anouk de Bakker, Adrien Lambert, Frans Buschman, Jasper Donker, Nynke Vellinga, Ton Hoitink, Maarten van der Vegt, Thijs van Kessel, Leo van Rijn, Susanne Quartel, Ayi Tarya, Amanda Sancho García and Wei Zhang for their advice, insightful discussions, weekly Italian lunches and monthly (well, sort of monthly) coastal group gatherings. Marion, thanks for our regular outings in Bordeaux and your ongoing teachings on French cuisine! I much appreciated your support during the final year of my thesis. Renske, I really enjoyed discussing each other's research, our regular exchange of work-related personal observations, and our ice-skating Mondays. Anouk, thanks for taking the time to help me understand waves, accompanied by biscuits. Adrien, thanks for your advice on buying the right mountainbike!

Besides the coastal group, the coffee corner of the department of Physical Geography provided the perfect spot for some social (and cross-disciplinary) interaction. I wish to thank all my colleagues at the department for the entertaining conversations on a wide variety of topics. I thank Juul Beltman for her personal touches in the coffee corner (the Christmas tree!) and for her administrative support. I want to thank Paul Hiemstra for his open-hearted discussions. Noemí Lana-Renault, our Nederfranspaans evenings together with Kris, Adèle, Florent and Gemma are legendary. Muchas gracias! Furthermore, I would like to thank Margot Stoete and Ton Markus for the lay-out of my research posters and for preparing the figures in this thesis.

The major drawback of remote sensing is the fact that it's remote, especially when it involves studying a beach on the Australian Gold Coast. The opportunity to walk on this mysterious beach on the other side of the world (does it actually exist?) has not yet arisen, but fortunately my research took me to places other than my desk in Utrecht. Special gratitude is due to my colleagues and friends in Bordeaux: Benjamin Dubarbier for his appetite for knowledge as well as for our Aquitanian surf sessions, Florent Birrien for his eye for all sorts of peculiarities, Camille Enjalbert for sharing her after-school activities, Barend van Maanen for living just 300 m away from my apartment (Pessac!) and providing me with a familiar face, Lisa Bethke for making groups of people get a move on, and Gesa Milzer for her observational wit.

I wish to thank Cesca Ribas for her encouragement and hospitality during visits to Barcelona, and Elena Ojeda and Tonatiuh Mendoza for their hospitality, friendship and tour-guiding, albeit in Spain or in Mexico.

A big thank you goes out to Sierd de Vries and Matthieu de Schipper, my scientific brothers of another mother, Marije Smit and Carola van der Hout. I truly enjoyed sharing our passion for coastal processes and surfing.

I also spent my time on a different type of bar dynamics, mostly involving glasses of beer. I especially want to thank Boudewijn for infecting me with his enthusiasm, Nicolai for keeping it real (i.e. his authentic compassion), Témy for his non-verbal communication skills and Rogier for his ever-evolving list of words and expressions. Thanks for the good times and for creating music together during our time as Kismet. I would also like to thank Peter (yoyoyo!), Ewout (is that your real name?!) and Nick (dorst!) for regularly discussing the latest matters over a drink.

I want to thank my family for believing in me and giving me the confidence to pursue my scientific career. Mum and Dad, thank you for your interest, patience and/or support (depending on how busy I was at the time). Chris, it's a true pleasure having such a great brother by my side during my defence, and Annika, thanks for your support. I also want to thank my (unofficial) parents-in-law, Marlies and Ger, for their interest and kindness.

Gemma, you mean a lot to me. There's a list of reasons why I wouldn't have ended up with this thesis without you, such as your unconditional support, down-to-earth view on things and the occasional kick up the derrière. Above all, I want to thank you for all the good moments we have together.

Timothy Price
Bunnik, January 2013

1 Introduction

1.1 Background

The nearshore zone of sandy coasts contains a variety of processes and morphological patterns acting over various temporal and spatial timescales (De Vriend, 1991; Holman, 2001). A ubiquitous morphological feature along many sandy coasts is the nearshore sandbar. Sandbars are approximately shore-parallel ridges of sand, located in shallow water along wave-dominated coasts with tidal ranges up to several metres. They have multi-annual lifetimes and can occur as a single bar or as a multiple (most often 2, sometimes up to 5) bar system (e.g., Wijnberg and Kroon, 2002; Ruessink et al., 2003). Sandbars often exhibit remarkable alongshore periodic undulations in their height and cross-shore position (e.g., Wright and Short, 1984; Lippmann and Holman, 1990; Van Enckevort et al., 2004). These so-called crescentic sandbars can be viewed as a rhythmic sequence of shallow shoals and deeper bays alternating shoreward and seaward of an imaginary line parallel to the coast (Figure 1.1). Depending on the wave conditions and the currents they induce in the nearshore zone, these sandbar patterns continuously change, vanish or reappear. It is this perpetual variability of nearshore sandbars that continues to draw the attention of nearshore researchers, just as it has done over the past decades (e.g., King and Williams, 1949; Hom-ma and Sonu, 1962; Sonu, 1973; Goldsmith et al., 1982; Coco and Murray, 2007).

Besides their intriguing morphological appearance, sandbars are also of significant societal importance. The nearshore zone of sandy coasts, comprising sandbars, forms a natural barrier between the hinterland and the ocean. Not only do nearshore sandbars safeguard beaches by dissipating wave energy before it impacts the shore, they also constitute a sediment buffer within the nearshore zone. The protection of low-lying, densely-populated coastal areas against flooding, such as those of The Netherlands, mostly involves engineering measures consisting of the upkeep of this natural sediment buffer within the nearshore zone (see e.g., Hoekstra et al., 1994). These shoreface nourishments lead to indirect modifications of nearshore sandbars (e.g., Grunnet and Ruessink, 2005). Increasing our understanding of nearshore sandbar behaviour will facilitate more efficient nourishment programs, both in terms of time and money, compared to current practices. In addition to their protective aspect, nearshore sandbars also affect recreational beach users. The strong offshore currents through the bays (i.e. rip currents) form the main hazard to unaware swimmers (Brander and MacMahan, 2011), leading to over 100 drownings annually in the United States alone (www.usla.org). To surfers, crescentic sandbars are generally favourable, with the alongshore variability of these bars enhancing the surfability of waves as they break over the sandbar (Scarfe et al., 2009, and references therein). Globally, the number of people living on the coast is increasing, and the average density of people living in coastal regions is 3 times higher than the global average density (see Small and Nicholls, 2003). A comprehensive understanding of the processes that

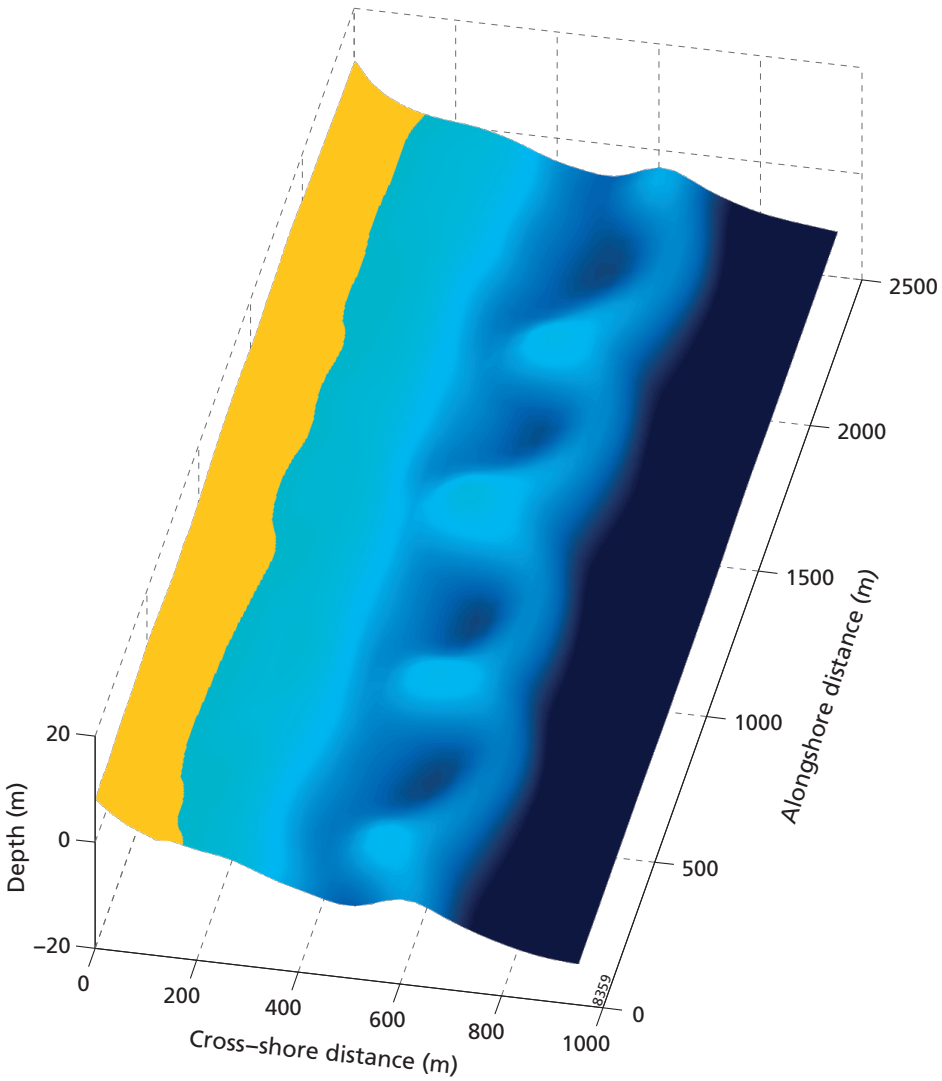

Figure 1.1 Bathymetry of a beach with a crescentic sandbar. This bathymetry was measured during the ECORS-Truc Vert'08 field experiment (adapted from Sénéchal et al., 2011).

govern nearshore sandbar behaviour and the development of the capability to predict this behaviour are thus of significant importance when it comes to minimising human and economic losses.

A key element to the understanding of morphological sandbar behaviour is frequent (daily), and long-term (∼years) monitoring of the nearshore zone, and the subsequent investigation of patterns and regularities in behaviour emerging from this observational data. Previous observations of nearshore sandbars vary from sporadic aerial photographs (e.g., Short and Aagaard, 1993; Castelle et al., 2007a), through yearly measurements of cross-shore profiles (Kuriyama, 2002), to daily images of the entire nearshore zone for a limited duration (e.g., Ruessink et al., 2007a; Almar et al., 2010). While these observations each provide a varying amount of insight into sand-

bar behaviour, the use of scarce data or the selective use of data carries the risk of assuming the identified behaviour to be representative of the characteristic system dynamics. Nowadays, with the rise of video-monitoring of the nearshore zone over the last 3 decades (Holman and Stanley, 2007), the trend towards frequent, long-term monitoring is increasing. Another key approach to the understanding of sandbar dynamics is the development, use, and validation of simplified exploratory and detailed simulation models. In contrast to observations from natural beaches and numerical modelling exercises, laboratory experiments have been used only scarcely to investigate the regularities underlying alongshore-variable sandbar behaviour (e.g., Bowen and Inman, 1971).

Most of the current research in this area has focussed on the initial formation of crescentic patterns, and to a lesser extent on the behaviour of existing crescentic sandbars, their finite-amplitude behaviour. Initially, it was believed that alongshore phase-locked (30-300 s) edge waves formed a *hydrodynamic* template that generated the alongshore variability in sandbar morphology (Bowen and Inman, 1971; Holman and Bowen, 1982). As reviewed in Van Enckevort et al. (2004), the basic assumptions underlying this approach have been proven to be incorrect. Nowadays, models rely on the principle of self-organisation (Hino, 1975; Sonu, 1972; Coco and Murray, 2007), in which crescentic sandbars are thought to form spontaneously as a result of the positive feedback between horizontal cell circulation patterns, including rip currents, sediment transport, and the morphology itself (Hino, 1975; Falqués et al., 2000). This feedback has been mainly explored through linear stability analysis (e.g., Hino, 1975; Deigaard et al., 1999; Falqués et al., 2000; Calvete et al., 2005; Van Leeuwen et al., 2006; Ribas et al., 2012), in which the temporal development of small, periodic perturbations superimposed on an initially uniform morphology is investigated using linearised, depth-integrated equations for mass and momentum conservation. Wave breaking on the bar induces circulation currents and sediment transports that reinforce the perturbations and lead to the initial growth of rhythmic crescentic bed patterns. Non-linear models (e.g., Damgaard et al., 2002; Reniers et al., 2004; Castelle et al., 2006; Garnier et al., 2006; Drønen and Deigaard, 2007; Garnier et al., 2008b) corroborate this self-organisation mechanism and additionally simulate the small alongshore variation in wavelength typical of natural crescentic sandbar systems (Van Enckevort et al., 2004; Holman et al., 2006).

In a double sandbar system, with a more landward inner bar and a more seaward outer bar, the distinction between a forcing template and self-organisation becomes blurred (Castelle et al., 2010a,b). In this case, the crescentic outer-bar morphology acts as a *morphological* template for the inshore flow patterns through the breaking and focussing of waves across the outer bar. Consequently, outer crescentic sandbars are often associated with similar rhythmic perturbations in onshore morphology, such as an inner sandbar (Castelle et al., 2007a; Ruessink et al., 2007a) and the shoreline (Sonu, 1973). This can lead to localised, severe beach and dune erosion (Komar, 1971; Thornton et al., 2007), and subsequent property losses during storms. It is obvious that this morphological coupling no longer relates to the initial formation of patterns, but relates to finite-amplitude behaviour instead. Here, the morphological template of

the crescentic outer bar may suppress local self-organisation mechanisms at the inner bar and hence govern the shape of the inner bar. Although morphological coupling has been observed and finite-amplitude behaviour of sandbars has been shown to be one of the largest sources of nearshore morphodynamic variability, it is not understood *when* and *why* morphological variations in an outer bar impact the geometry of the inner bar.

The main objective of this thesis is to increase our understanding of existing crescentic patterns in double sandbar systems, with a focus on morphological coupling. I do this through both field observations and numerical modelling, and aim to bring these two together.

1.2 Double sandbar systems in the nearshore

1.2.1 Morphodynamic states

Numerous observations and long-term monitoring of the nearshore zone have revealed the wide range of shapes that nearshore sandbars may attain. Despite each observed sandbar configuration being unique, and the continuous change in shape under the influence of waves and currents, a certain regularity in sandbar morphology has been observed. Accordingly, sandbar morphology is often aggregated into several discrete sandbar states, each with a characteristic morphological appearance. Such an aggregation facilitates answers as to *when* certain behaviour, such as morphological coupling, actually happens. The occurrence of each sandbar state is also often associated with the intensity or energy of the incoming wave field.

For single-barred beaches, Wright and Short (1984) developed the most widely accepted and applied beach state classification model, based on observations of beaches with contrasting environmental conditions over a period of 3 years (Figure 1.2). They identified two end members, the dissipative (D) and the reflective (R) state, which were found to be related to persistent high and low energetic conditions respectively. A sandbar is generally found in intermediate states, identified by Wright and Short (1984) as longshore bar and trough (LBT), rhythmic bar and beach (RBB), transverse bar and rip (TBR) and low tide terrace (LTT), resulting in a total of six beach (or, bar) states. During an accretionary (downstate) sequence (Short, 1979), associated with low-energetic conditions, a bar mostly advances through each of the intermediate states toward the reflective state over a number of days to weeks (Ranasinghe et al., 2004). However, the larger amount of energy inherent to erosional (upstate) sequences (Short, 1979, 1999), often causes the bar to jump to a higher state within hours (e.g., Lippmann and Holman, 1990; Van Enckevort and Ruessink, 2003; Ranasinghe et al., 2004), with the bar briefly acquiring the erosional intermediate states described by Short (1979). An erosional sequence where all pre-existing alongshore variability is erased, resulting in the alongshore-uniform longshore bar and trough state, is often referred to as a morphological reset.

Although the Wright and Short (1984) classification model is essentially applicable to single-barred beaches only, Short and Aagaard (1993) devised a multi-bar state

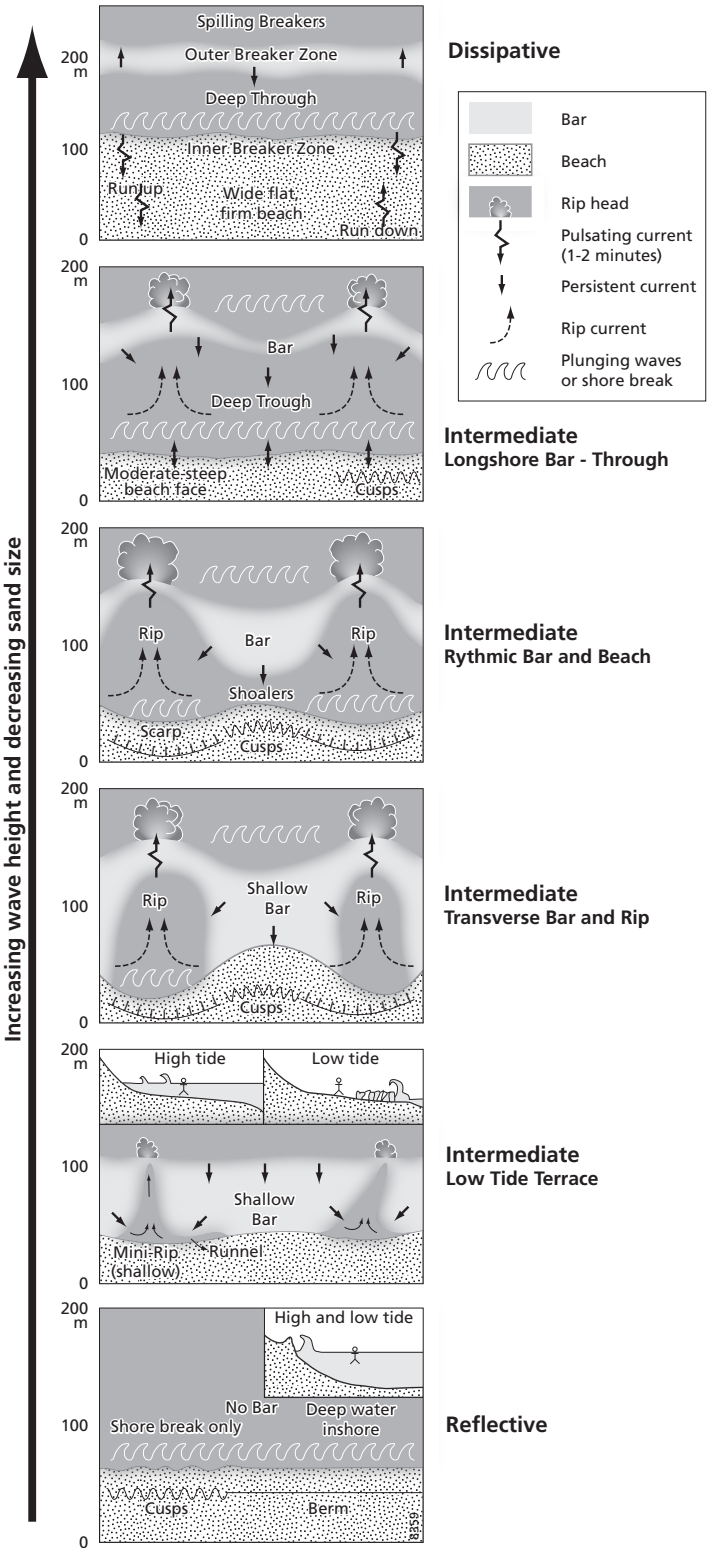

Figure 1.2 The Wright and Short (1984) morphodynamic classification of beach states. Adapted from Wright and Short (1984).

model where each bar can go through the same states as in the single bar model. The sandbars are essentially treated as independent features and the role of coupling between the bars for the behaviour of the composite double sandbar system is thus disregarded. Ruessink et al. (2007a)'s 8-week data set already shows the inner-bar LTT state in case of coupling to be different from a typical (uncoupled) single bar LTT, indicating Short and Aagaard (1993)'s schematisation to be incomplete. An important first step in addressing the overall aim of this thesis will therefore be to thoroughly test validate and extend Short and Aagaard (1993)'s conceptual bar-state model.

1.2.2 Observations of sandbar coupling

In the aforementioned study by Ruessink et al. (2007a), the inner bar increasingly coupled to the outer-bar shape as the outer bar became more crescentic and migrated onshore, i.e. during a downstate transition of the outer bar from the alongshore uniform longshore bar and trough (LBT), through the rhythmic bar and beach (RBB) to the transverse bar and rip (TBR) state (Wright and Short, 1984). The initially featureless terrace-shaped inner bar, i.e. low-tide terrace (LTT), developed an alongshore variability coupled to the outer-bar shape. Intriguingly, the coupled inner-bar pattern was displaced alongshore with respect to the outer-bar pattern by 100 to 200 m. With a wavelength of some 800 m of the outer-bar pattern, this corresponds to a 90° phase shift.

Other observations of double sandbar systems indicate that sandbars do not necessarily couple at 90°. In fact, coupling appears to have been most often observed at 0° and 180°. For example, in the observations by Van Enckevort and Wijnberg (1999) seaward protrusions of the inner bar faced the so-called horns (the more landward, shallow areas) of the crescentic outer bar (Figure 1.3a). This situation is reminiscent of the commonly observed (180°) out-of-phase coupling between bar patterns and shoreline perturbations (e.g., Komar, 1971; Sonu, 1973; Orzech et al., 2011), as given in Figure 1.3b. In-phase (0°) coupling has also been observed for both the shoreline (e.g., Komar, 1971) as the inner bar (e.g., Bowman and Goldsmith, 1983; Castelle et al., 2007a), in which case inner-bar rip channels face outer-bar bays (Figure 1.3c). Castelle et al. (2007a) even noted the systematic occurrence of two inner-bar rip channels within one outer-bar bay, or crescent (Figure 1.3d). In addition to the 90° phase shift in coupled sandbar patterns observed by Ruessink et al. (2007a), Quartel (2009) observed phase shifts to vary between 0° and 180°. An existing crescentic outer bar, however, does not necessarily lead to coupled inshore morphology. Hom-ma and Sonu (1962) and Bowman and Goldsmith (1983), for example, did not observe any phase coupling, despite the outer-bar horns being welded to an inner bar.

These current observations of sandbar coupling were either based on sporadic observations (e.g., Bowman and Goldsmith, 1983; Castelle et al., 2007a) or on a short single event (e.g., Ruessink et al., 2007a). Consequently, the representativeness of these findings, in particular as to *when* and *how often* certain coupling types develop, is not known. Furthermore, as a first step towards understanding *why* a

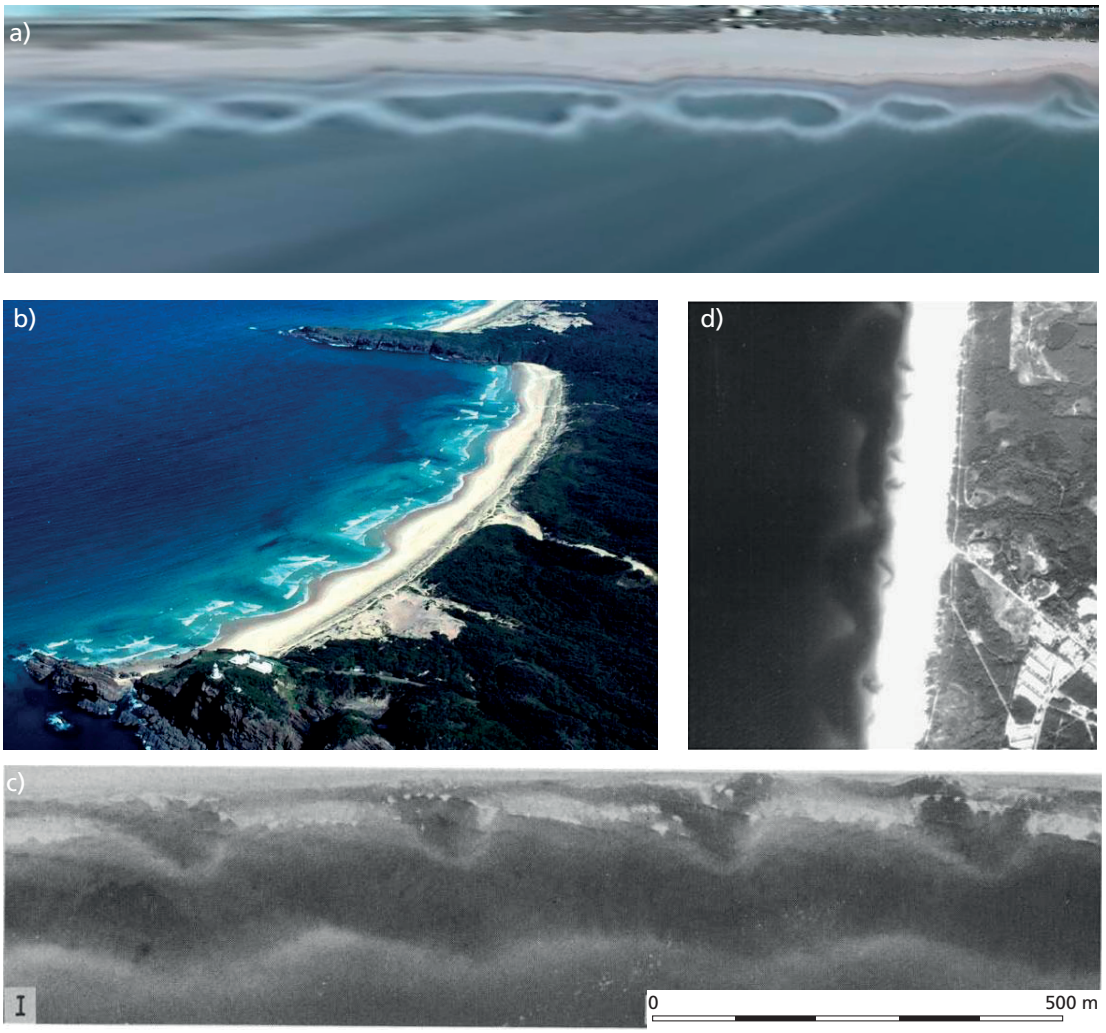

Figure 1.3 Examples of coupled morphology, showing (a) out-of-phase (180°) coupled sandbars, (b) out-of-phase coupling between sandbar and shoreline (courtesy of A. D. Short), (c) in-phase (0°) coupled sandbars (taken from Bowman and Goldsmith, 1983), and (d) two inner-bar rips channels for each single outer-bar bay (IGN, 1978; courtesy of B. Castelle).

certain coupling type occurs, it is not known whether the type of coupling depends on environmental conditions such as the wave conditions preceding coupling.

1.2.3 Modelling sandbar coupling

Although observations of sandbar morphology provide information as to *when* sandbars couple, the question as to *why* sandbars couple remains largely unexplored. At most, a relation between the occurrence of coupling and representative wave conditions can be established. Ruessink et al. (2007a) and Quartel (2009), for example, both suggested their observed phase shift in coupled sandbar patterns to be related

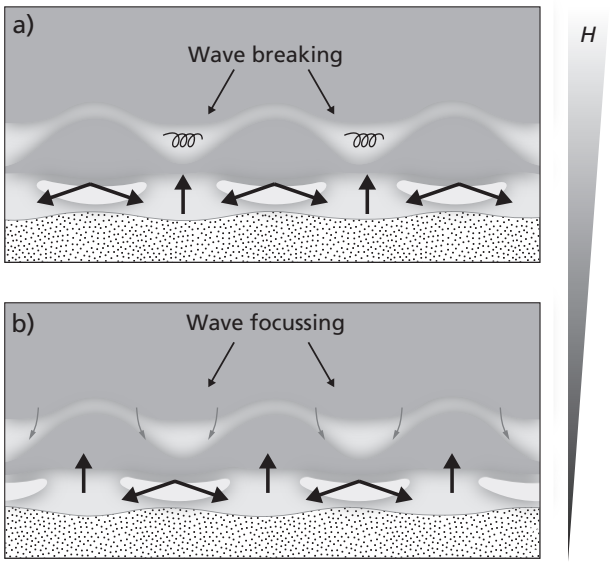

Figure 1.4 Coupling patterns found by Castelle et al. (2010a), showing (a) out-of-phase coupling and (b) in-phase coupling, depending on the wave height H. The black arrows indicate the associated flow pattern, whereas the gray arrows indicate wave refraction.

to the nonzero angles of wave incidence at their respective study sites, although it remains unclear *why* oblique wave incidence leads to this shift.

Using a numerical model with synthetic boundary conditions, Castelle et al. (2010a,b) recently shed light on the processes leading to morphological sandbar coupling under shore-normal wave conditions. They found that coupled inner-bar features arise from horizontal circulation patterns driven by alongshore variations in wave breaking and wave refraction across a crescentic outer bar. A large fraction of wave breaking over the outer bar leads to out-of-phase coupled sandbars (Figure 1.4a). For a small fraction of wave breaking, wave focussing by refraction over the outer-bar horns overwhelms the effect of wave breaking, leading to in-phase coupled sandbars (Figure 1.4b). The alongshore variability in outer-bar depth was found to be crucial for the turning point between in-phase and out-of-phase coupling.

Whereas the simulations of Castelle et al. (2010a,b) were performed for shore-normal wave incidence, angles of wave incidence are more often non-zero at natural open coast beaches. In this case, the circulatory flow, with feeder currents and rip channels (Figure 1.5a), becomes more alongshore-oriented. Over a crescentic bar, the alongshore flow may be deflected landward and seaward, creating a meandering alongshore current (Sonu, 1972; MacMahan et al., 2010), as given in Figure 1.5b. Thiébot et al. (2012) performed numerical simulations of a double-barred system for varying angles of wave incidence with initially alongshore-uniform sandbars. For small angles of wave incidence, they found that the inner bar initially does not develop any alongshore variability due to the significant alongshore current at the inner bar. Once the outer bar starts to develop alongshore variability, however, the alongshore current and the incoming wave field at the inner bar become perturbed, leading

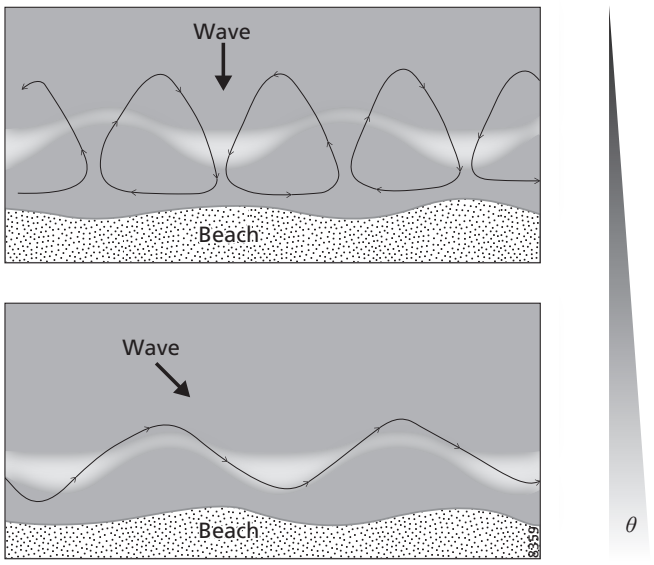

Figure 1.5 Dependence of flow patterns on angle of wave incidence θ, with (a) circulatory flow under shore-normal wave incidence, and (b) meandering alongshore flow under oblique wave incidence (after Sonu, 1972).

to the appearance of inner-bar features. This prerequisite of an existing crescentic outer bar for the development of inner-bar variability under obliquely incident waves corroborates the observations of Ruessink et al. (2007a).

Thus, while the genesis of crescentic sandbars is reasonably well understood, the morphodynamic mechanisms underlying their subsequent finite-amplitude behaviour, and coupling in particular, remain largely unknown to date. Furthermore, it remains unclear how, for a given crescentic outer bar, the angle of wave incidence affects the coupling processes at the inner bar. Existing modelling efforts of double sandbar systems used synthetic or highly-idealised bathymetries. Given the importance of the alongshore variability of the outer bar to coupling processes (Castelle et al., 2010a), the incorporation of observational data would ensure a more comprehensive modelling exercise than the synthetic simulations done so far.

1.3 Objectives and thesis outline

The general objective of the research presented herein is to understand the morphodynamic behaviour of existing crescentic sandbars in a double sandbar system. By behaviour, I mean the change in alongshore variability of the double sandbar system under the influence of wave forcing. The work in this thesis is based on observations from a natural, double-barred beach: Surfers Paradise, The Gold Coast, Queensland, Australia (Figure 1.6). From 1999 to 2008, an Argus video system collected images (Turner et al., 2006), providing 9 years of daily observations of the alongshore sandbar patterns (Figure 1.7). Measurements from nearby wave buoys provide concurrent

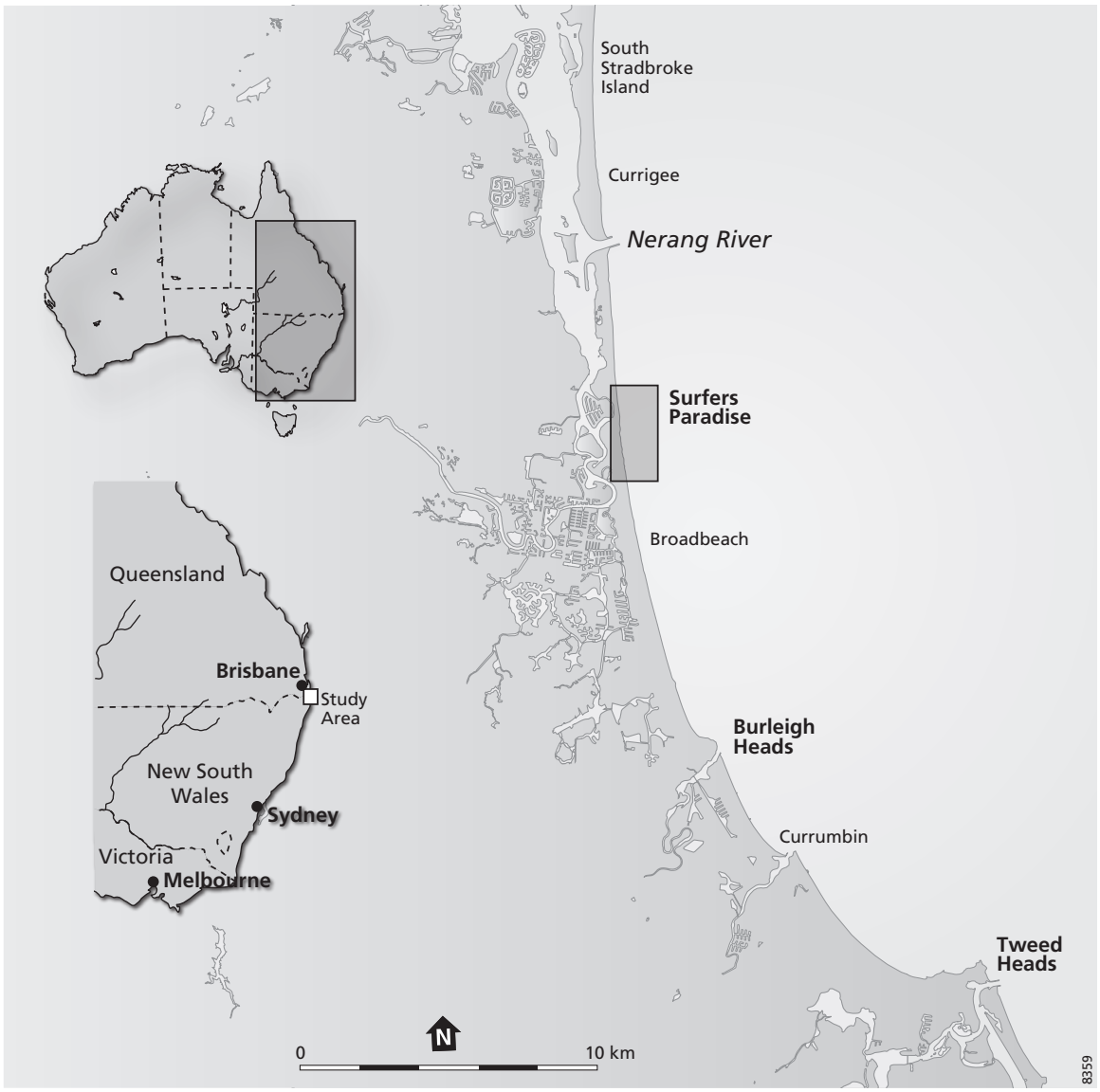

Figure 1.6 Location of the study site: Surfers Paradise, Gold Coast, Queensland, Australia.

wave data (i.e. wave height, wave period and angle of wave incidence). An event of sandbar coupling has been observed previously at this beach (Ruessink et al., 2007a), and the incoming waves are generally obliquely incident. To reach the general objective, different aspects of the double sandbar system are studied, using a number of approaches. The structure of this thesis and the research goals I aim to answer, are as follows:

1. *Establish the morphodynamic states that characterise a double sandbar system.* As described above, a bar-state approach facilitates answers as to *when* certain behaviour is observed, but the existing multiple bar-state model of Short and

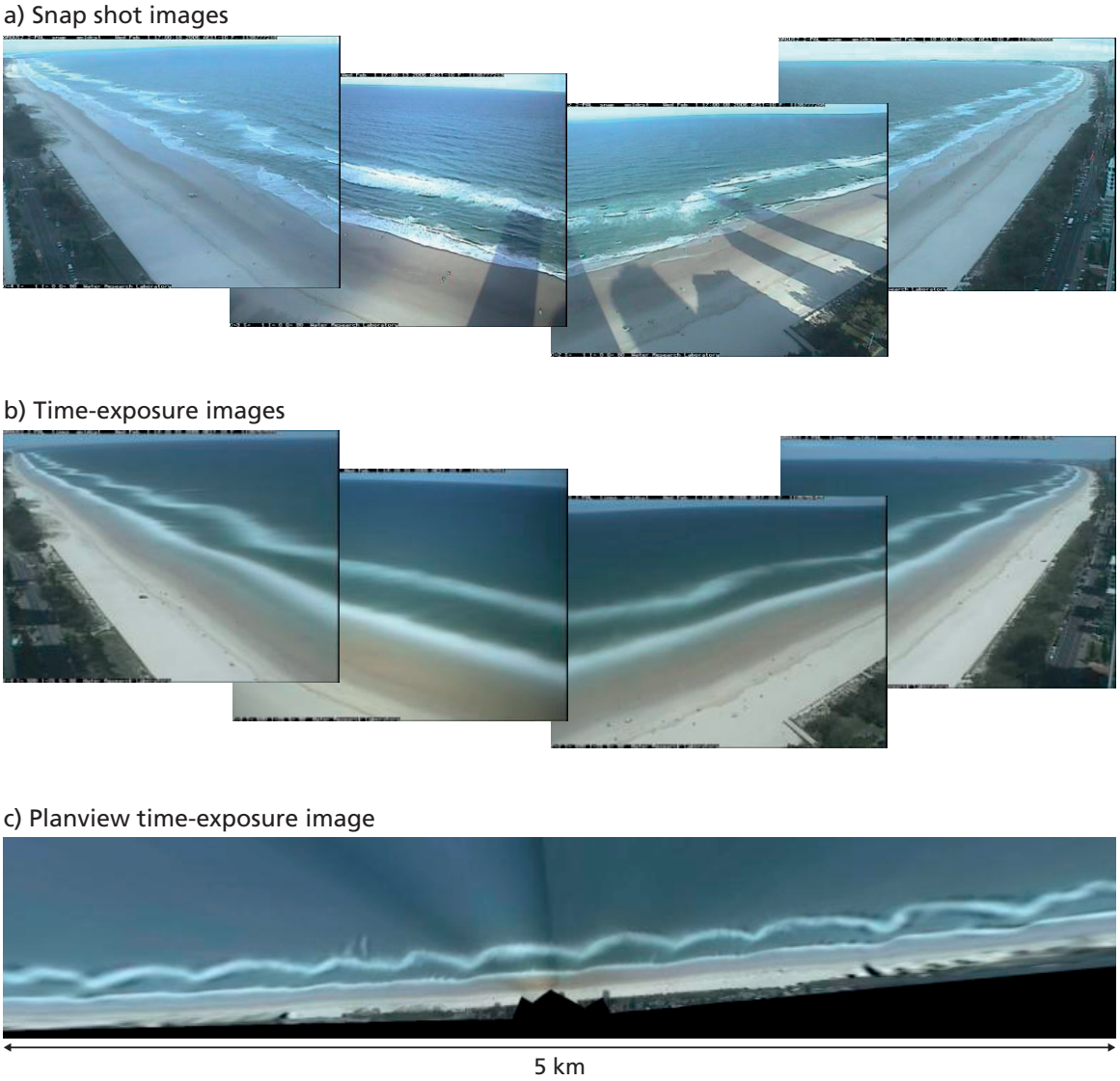

Figure 1.7 Images obtained with the Argus video system. Four cameras provided hourly (a) snap shot images and (b) time-exposure images. Merged and rectified images of the four time-exposure images (c) were used herein.

Aagaard (1993) disregards coupling. In Chapter 2, I first devise a method to objectively classify the double-sandbar states from the 9 years of video images. I then explore how changes in outer-bar state relate to the preceding wave conditions, and subsequently study the inner-bar state in relation to that of the outer bar.

2. *Determine the importance of morphological coupling for the overall behaviour of a double sandbar system.*
   The frequency of morphological coupling and the predominant appearance of coupling patterns within a double sandbar system remain unknown to date. In

Chapter 3 I quantify the occurrence of coupling from the video images, and investigate the phase differences between the coupled sandbar patterns. Thereupon, I determine *when* different coupling patterns are found in relation to the morphodynamic states defined in Chapter 2. As a first step towards understanding *why* these different patterns develop, I explore the dependence on offshore wave conditions, in particular the angle of wave incidence. Castelle et al. (2010a) suggested the alongshore depth variation of the outer bar to be an important parameter leading to coupled sandbar morphology. As bathymetric data was collected too infrequently at the site studied, I apply an assimilation model to estimate the alongshore depth variations of the outer bar from the video images. Finally, I put forward hypotheses as to *why* different coupling patterns arise.

3. *Analyse how the angle of wave incidence affects the coupling processes within a double sandbar system.*
   For shore-normally incident waves, Castelle et al. (2010a,b) illustrated the effect of varying wave heights for coupling patterns. For obliquely incident waves, however, an alongshore current comes into play. In Chapter 4 I analyse how the angle of wave incidence over an existing crescentic outer bar affects the inner-bar morphodynamics. Building upon the hypotheses from Chapter 3, I use a numerical model to study *why* the coupling processes at the inner bar change, with a focus on the effect of the angle of incidence on inshore flow patterns. In contrast to existing modelling efforts of double-barred systems, which use synthetic or highly-idealised bathymetries, I force the model with realistic bathymetrical data derived from the video observations. Besides ensuring a more comprehensive modelling exercise with this approach, I also aim to bridge the gap between field observations and numerical modelling.

In Chapter 5, I combine the findings of the preceding chapters to form an integrated view of the finite-amplitude (coupling) behaviour of nearshore crescentic sandbars in a double sandbar system. This final chapter also includes a discussion on open issues and recommendations for future research.

2 State dynamics of a double sandbar system

Based on: Price, T. D. and Ruessink, B. G. (2011), State dynamics of a double sandbar system. Continental Shelf Research, 31, 659–674.

2.1 Introduction

The nearshore zone along many sandy beaches is characterised by the presence of (ir)regular patterns of local shallows. These shallows, referred to as sandbars, exhibit intriguing spatial and temporal variations in morphological states, ranging from alongshore continuous ridges (linear bars), through alongshore sequences of shoals and bays (crescentic bars) to low-relief terrace-shaped bars (King and Williams, 1949; Sonu, 1973; Wright and Short, 1984; Van Enckevort et al., 2004, among others). Despite extensive observations and conducive modelling efforts, the perpetual variability of sandbar morphology continues to draw the attention of nearshore researchers.

For single-barred beaches, Wright and Short (1984) developed the most widely accepted and applied bar state classification model, based on observations of bar morphologies at beaches with contrasting environmental conditions over a period of 3 years. They identified two end members, the dissipative (D) and the reflective (R) state, which were found to be related to persistent high and low energetic conditions, respectively. On the timescale of storms, however, these states are rarely reached due to the relaxation time inherent to morphological response of sandbars (Wright et al., 1985). Instead, bars generally are found in intermediate states, identified by Wright and Short (1984) as longshore bar and trough (LBT), rhythmic bar and beach (RBB), transverse bar and rip (TBR) and low tide terrace (LTT), resulting in a total of six bar states. During an accretionary (downstate) sequence (Short, 1979), the bars mostly advance through each of the intermediate states toward the reflective state over a number of days to weeks (Van Enckevort et al., 2004). The larger amount of energy inherent to erosional (upstate) sequences (Short, 1979, 1999), however, often causes the bar to jump to a higher state within hours (e.g., Lippmann and Holman, 1990; Van Enckevort and Ruessink, 2003; Ranasinghe et al., 2004), with the bar briefly acquiring the erosional intermediate states described by Short (1979). An erosional sequence where all pre-existing alongshore variability is erased, resulting in the alongshore-uniform longshore bar and trough state, is often called a morphological reset.

Although the Wright and Short (1984) classification model is essentially applicable to single-barred beaches only, Short and Aagaard (1993) devised a double bar state model where each bar can go through the same states as in the single bar model. In general, the outer bar evolves more slowly through the bar states and is typically

more upstate than the inner bar. The outer bar has rarely been observed to reach the reflective state and often occurs as a quasi-inactive feature during low-energetic periods (Goldsmith et al., 1982; Castelle et al., 2007a; Ferrer et al., 2009). The inner bar, on the other hand, is far more dynamic and may progress through all the bar states, occasionally obtaining the reflective state. Observations of two accretionary sequences of both the inner and outer bar at the Gold Coast, Australia (Ruessink et al., 2007a) were found to be consistent with the Short and Aagaard (1993) model.

Besides the readily apparent response of bar state occurrence to offshore wave forcing, observations (Lippmann et al., 1993; Van Enckevort et al., 2004; Ruessink et al., 2007a; Almar et al., 2010) and numerical modelling results (Castelle et al., 2010a,b) of multi-barred beaches have indicated that morphologic feedback between the outer and inner bar(s) forms an important aspect of the state dynamics of a double-barred system. The distance between the inner and outer bars as well as the cross-shore geometry and the alongshore variability of the outer bar have been found to be critical parameters governing the morphological evolution of the composite bar system.

Although considerable research has been devoted to the state dynamics of a double-barred system, observations were mostly based on data which were either temporally limited to a single accretionary/erosional sequence (e.g., Van Enckevort et al., 2004; Ruessink et al., 2007a), spatially limited to (an alongshore transect of) the inner bar (e.g., Lippmann and Holman, 1990; Shand et al., 2003; Sénéchal et al., 2009) or based on data acquired at different locations or at irregular intervals (Short and Aagaard, 1993; Castelle et al., 2007a). Furthermore, the large relaxation times of outer bars, in relation to the offshore wave forcing, have often prevented an abundance of state transitions of the outer bar to occur during the studied periods (see e.g., Goldsmith et al., 1982; Ferrer et al., 2009). To date, the sequential behaviour of the bar states of a double-barred system at a single site has thus not been studied under a wide range of wave conditions. Analysis of multiple sequences, however, would provide a more comprehensive understanding of the state dynamics.

This paper aims at characterising the typical development of the alongshore variability of a double-barred system, using a 9.3-year long data set of daily high-resolution video observations from the northern Gold Coast, Queensland, Australia (Section 2.2). In Section 2.3, a method is established to enable the objective classification of the observed bar states. Subsequently, the frequency of the bar states and changes in bar state are quantified and regarded with respect to offshore wave forcing and morphological feedback (Section 2.4). Besides the antecedent morphology affecting the impact of the offshore wave forcing on each bar, it is shown that the outer bar governs the state of the inner bar to a large extent. Finally, in Sections 2.5 and 2.6, our main findings are discussed and summarised.

2.2 Study area and data collection

2.2.1 Study area

The bar state dynamics were studied for the double-barred beach at Surfers Paradise, located at the northern end of the Gold Coast in south-east Queensland, Australia (Figure 2.1). The double barred system at this site has previously been found to exhibit all intermediate beach states as described by Short and Aagaard (1993), see Ruessink et al. (2007a). On average, the inner and outer bar are located some 50 and 150 m from the mean-sea-level shoreline. In addition to the dominant cross-shore response of both bars to the seasonal signal in wave height, Ruessink et al. (2009) found the sandbars at the Gold Coast to exhibit episodic net offshore migration, whereby an individual wave event with wave heights three to four times the annual average triggers the decay of the outer bar. During such an event, the outer bar migrates further offshore into deeper water than usual, where it slowly decays by onshore sediment transport during the subsequent period of lower waves. During the next period of moderately high waves, the inner bar moves offshore and takes its place as the new outer bar and a new bar develops onshore.

The coastline at Surfers Paradise is aligned approximately north-south and faces the South Pacific Ocean. The specific study site is a wave-dominated, 2 km long straight stretch of beach, located toward the northern end of the 20 km of continuous coastline that extends from Burleigh Heads in the south to the trained Nerang River entrance 5 km further north. The nearshore is composed of predominantly quartz sand with a median grain size of about 250 µm. The nearshore bed slope is (approximately) 0.02. The Gold Coast is exposed to persistent southeasterly swells generated by mid-latitude lows crossing the southern Tasman Sea (Allen and Callaghan, 1999), resulting in a net annual littoral drift in the order of $500,000$ m^3 to the north (Patterson, 2007). The mean root-mean-square wave height H_{rms} at the Gold Coast wave rider buoy (in 18 m depth) is about 0.8 m with a peak period T_p of some 9 – 10 s. During East Coast lows (formed off the New South Wales coast) and tropical lows (which form north of the study area in the Coral Sea) the significant wave height H_s can increase to well over 1.5 m, with an estimated return interval of 2 years for $H_s = 3.5$ m (Allen and Callaghan, 1999). The tide is semi-diurnal with a spring tidal range of 1.5 – 2 m.

In 1999 – 2000 a 1.2 Mm^3 beach nourishment was undertaken to maintain and enhance the subaerial beach width (Turner et al., 2004). The implementation of the nourishment near our study site commenced early November 1999 about 4 months after the image collection started, and reached its southernmost extension in June 2000. The effect of the nourishment on the sandbars was most pronounced in March and April 2000. As our study site was restricted to the area to the south of the nourishment (Section 2.2.2), our sandbar data was not directly impacted by the nourishment. In 2005 and 2007 a series of minor beach nourishments were carried out, each less than $\approx 40,000$ m^3 and presumably of no importance to the sandbar evolution at Surfers Paradise (Ruessink et al., 2009). A hybrid coastal protection-surfing reef structure is located at Narrowneck, just north of the study site (Turner et al., 2004). A boulder wall revetment backs the entire length of the beach.

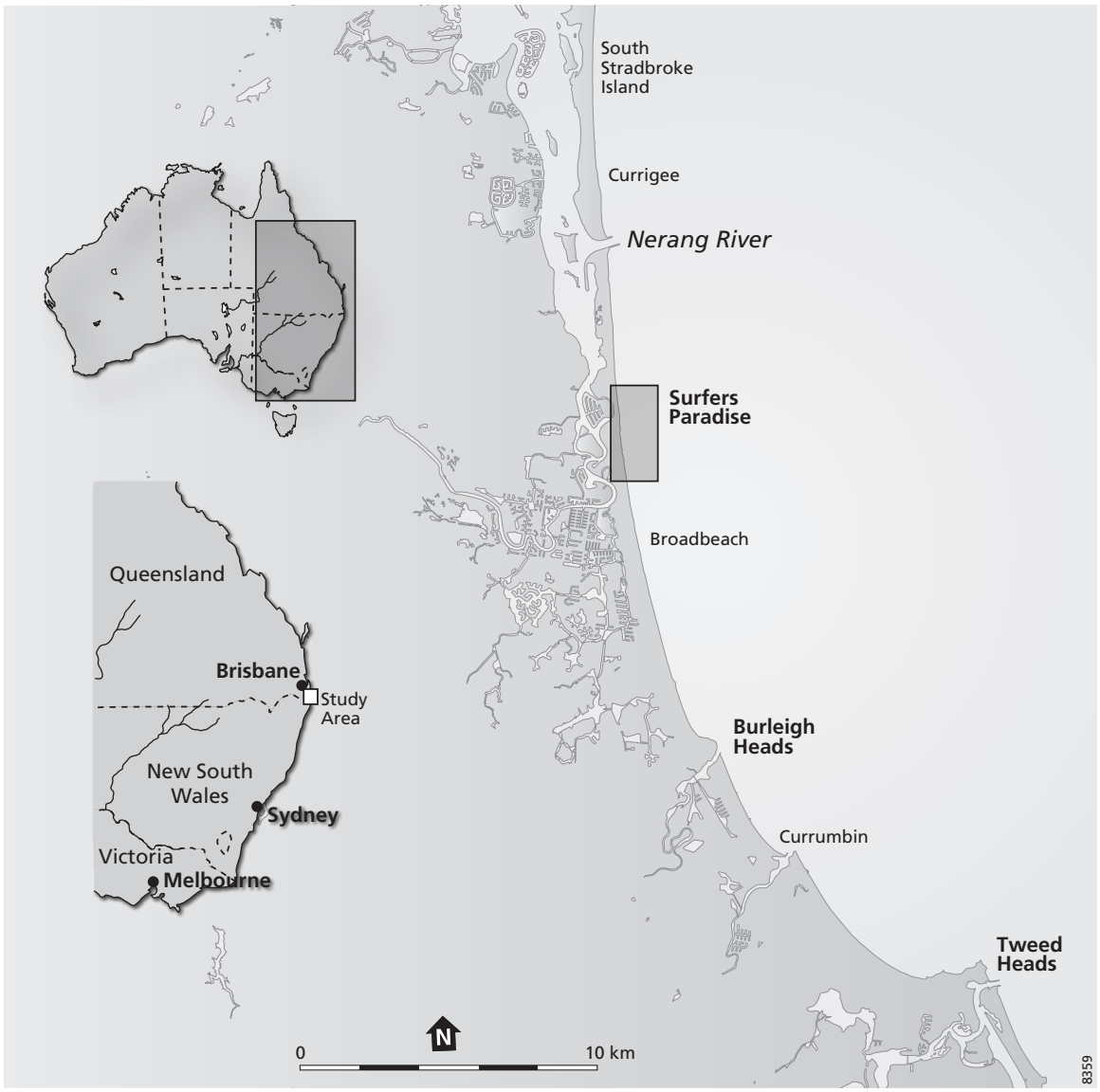

Figure 2.1 Location of the study site.

2.2.2 Video imaging

In July 1999, an Argus video-imaging system (Holman and Stanley, 2007) was installed atop a beachfront apartment building, approximately 100 m above mean sea level. The system consists of four cameras pointed obliquely along the beach, providing 180° uninterrupted coverage of the northern Gold Coast region (Turner et al., 2004, 2006). Each daylight hour the system routinely collects a 10-minute time-exposure image for every camera, created by the averaging of 600 individual snapshots sampled at 1 Hz. All four images are rectified (Holland et al., 1997) and merged to obtain planview images spanning 5000 m and 900 m in longshore and cross-shore direction, respectively. For this study, a single camera (camera 1) was used, covering the southernmost 2 km (from $y = -500$ to -2500 m) of the beach in range of the

cameras (Figure 2.2). The use of a single camera was motivated by the wish to avoid (i) the interference of the natural bar dynamics by the artificial surfing reef towards the north of the beach (at alongshore coordinate $y \approx 1000$ m, in Figure 2.2), and (ii) the intensity differences between the merged camera images. Image coordinates were converted to real-world coordinates by linking a set of clearly visible control points to their image coordinates, in combination with the measured camera positions and properties. The accuracy of this photogrammetric transformation typically corresponds to one pixel, resulting in a ground accuracy of less than 2 m and 0.5 m in the cross-shore and alongshore directions, respectively. The oblique orientation of the cameras causes these accuracies to worsen to about 30 m and 8 m towards the southernmost extent of the field site ($y = -2500$ m).

The basic premise behind the video-imaging system to infer sandbar characteristics, is the preferential wave breaking over shallow features (Lippmann and Holman, 1989). The foam on the water surface, resulting from the breaking waves, enables the detection of sandbars through the areas of high intensity in the time-exposure images. Accordingly, deeper areas appear as dark regions in the images due to the absence of wave breaking. In the next section, we will explain how we use these intensity variations to extract the bar states from the time-exposure images for this study. The cross-shore location (migration) of the optical breaker line (henceforth referred to as the barline) with respect to the actual bar crest location is a function of the (changes in) offshore wave height, the water level and the geometry of the sandbar itself (Van Enckevort and Ruessink, 2001; Pape et al., 2010; Ribas et al., 2010). At sites with a non-zero tidal range, such as the Gold Coast, the tidal water level variation is the main source of the temporally varying discrepancy between the video-observed and actual barline positions. To minimise the apparent (cross-shore and alongshore) barline variability related to changes in tidal water level, we used low-tide images only.

This study uses a 9.3-year data set of daily low-tide planview images, spanning from 15 July 1999 to 29 October 2008 (a total of 3395 days). During the entire period, images were sometimes unavailable because of temporary malfunctioning of the camera system (315 days) or unsuitable due to poor image quality (e.g. fog or rain drops on the camera lens; 164 days), reducing the total number of available images to 2916. Besides unavailable images, insufficient wave breaking over the bar(s) further restricted the number of images suitable for the extraction of bar states. As shown in the next section, these data gaps could be filled by interpolation of the parameters deduced from the available images.

We complement our sandbar data set with a mid-tide shoreline data set, $x_{\text{shore}}(t, y)$, gathered in the framework of the Northern Gold Coast Beach Protection Strategy (Boak et al., 2000). These shorelines were extracted approximately weekly from mid-tide Argus image using the detection algorithm of Aarninkhof et al. (2003). Prior to September 2000 shoreline positions were estimated less frequently. A continuous set of shorelines, corresponding to our study site and period, was obtained through interpolation of the available data and the replacement of missing data with the mean shoreline position of the corresponding day.

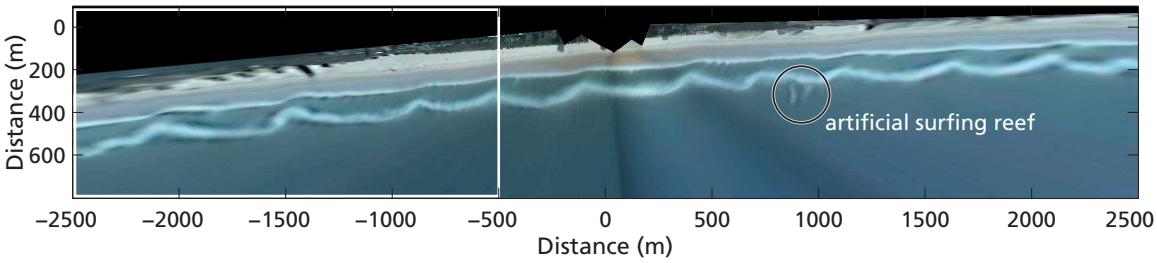

Figure 2.2 Planview time-exposure image (from February 1, 2006) showing the study site (white rectangle). The artificial surfing reef can be seen as two seaward protrusions of the breaker zone at an alongshore distance y of ≈ 1000 m (black circle).

2.2.3 Wave data

Hourly root-mean-square wave height (H_{rms}) and peak wave period (T_p) were obtained from the Gold Coast non-directional wave rider buoy, located approximately 2 km offshore of the study area, in 18 m water depth. Missing data (10.2 % in time) were replaced by H_{rms} and T_p recordings from the Brisbane wave rider buoy, located approximately 60 km to the north in 76 m water depth. While the T_p values for the Brisbane and Gold Coast are essentially identical, a standard feed-forward artificial neural network (ANN) was used for obtaining representative H_{rms} values for the Gold Coast (see Ruessink et al., 2009 for details). As the Gold Coast buoy is non-directional, the hourly angles of wave incidence θ at the Brisbane buoy were refracted to 18-m depth using Snell's law to yield estimates of θ directly offshore of the study site. Time series of the hourly H_{rms}, T_p and θ at the Gold Coast are given in Figures 2.3a, b and c, respectively.

2.3 Bar states

2.3.1 Bar state classification

During the downstate sequence of Wright and Short (1984), the alongshore variability of the sandbar changes as it progresses from the alongshore uniform LBT. At first, the alongshore variability of the barline increases as the bar becomes crescentic and attains the RBB state. The trough, however, remains alongshore uniform. The shore-attached horns of the crescentic bar (or inner bar-attached, in the case of the outer bar) during the TBR state, make the trough alongshore discontinuous while the bar remains crescentic. The successive infilling of the trough and the welding of the inner sandbar to the shoreline, as the bar progresses toward the LTT state, reduces the alongshore variability of the barline and further reduces the alongshore continuity of the trough. Finally, at the reflective extreme of the downstate sequence, both the barline and the trough have returned to being alongshore uniform. In this case, however, the trough is completely alongshore discontinuous, i.e. non-existent. During an erosional sequence the bar does not progress through the states of a downstate sequence. Instead, the barline rapidly straightens and the trough continuity

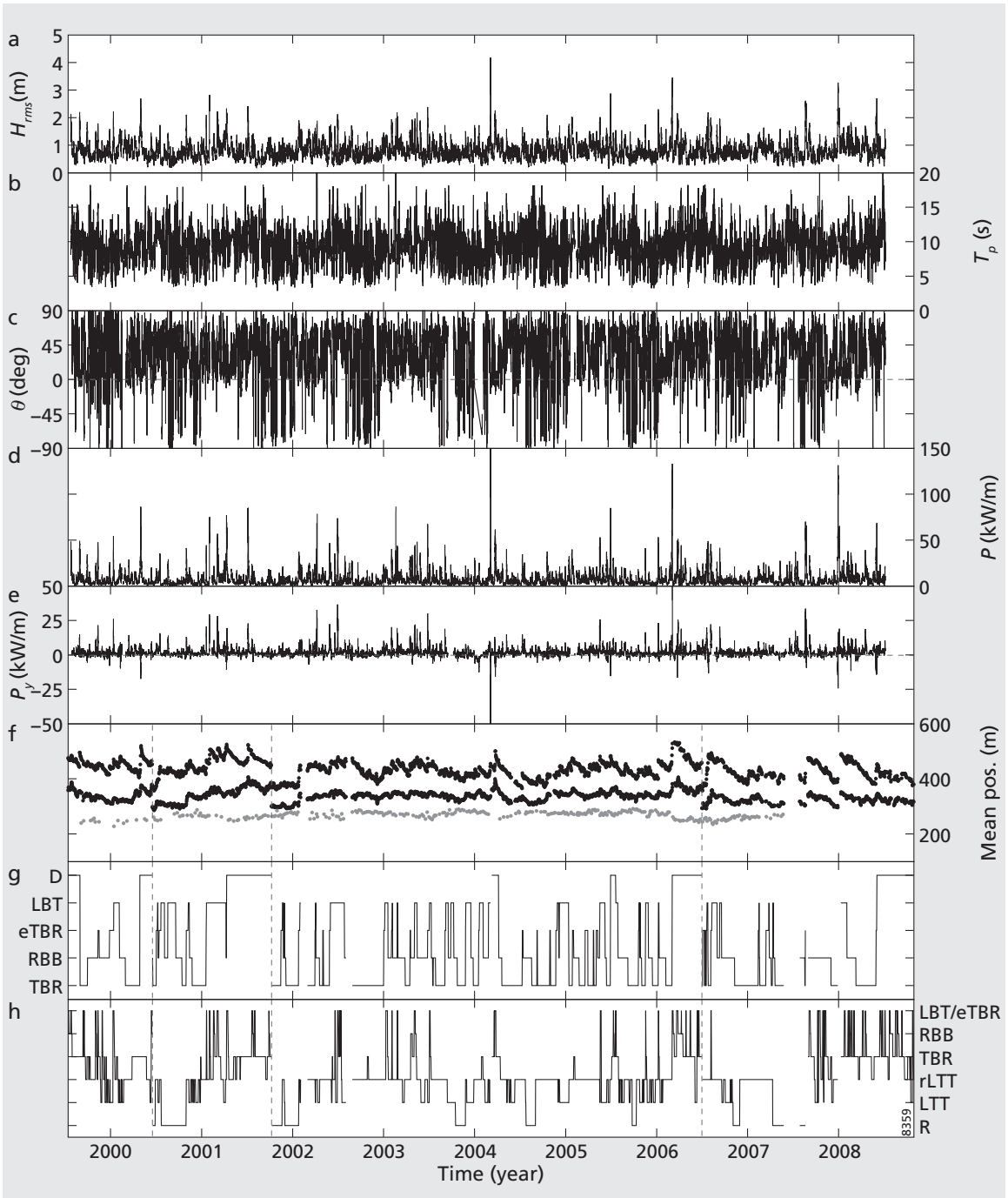

Figure 2.3 The (a) offshore root-mean-square wave height H_{rms}, (b) offshore peak period T_p, (c) offshore angle of wave incidence θ from shore normal, (d) offshore wave power P, (e) offshore alongshore wave power P_y, (f) alongshore-averaged (over $y = -500$ to -2500 m) inner and outer sandbar (black dots) and mid-tide shoreline (grey dots) cross-shore locations, $\bar{x}_{in}$, $\bar{x}_{out}$ and $\bar{x}_{shore}$, respectively, (g) outer bar state, (h) inner bar state versus time at Surfers Paradise, the Gold Coast. The dashed vertical lines in (f), (g) and (h) indicate the decay moments of the outer bar.

increases as erosional rip channels start to develop (see Short, 1979, 1999, 2006). Herein, we refer to this state as the erosional TBR, eTBR. From the above, it follows that the upstate and downstate extremes show the smallest alongshore variability, whereas the intermediate TBR state exhibits the greatest alongshore variability. The alongshore barline variability σ_{bp} and the alongshore trough continuity σ_{ti} provide the measures (i.e. morphological indicators) for the alongshore variability of the sandbar morphology in this study.

The crest lines of both the inner and outer bar were extracted from all the available video images by the automated alongshore tracking of the intensity maxima across each bar (Van Enckevort and Ruessink, 2001; Pape et al., 2010). The alongshore variability of the barline σ_{bp} was quantified by determining the standard deviation of the barline position, which was first linearly detrended and band-pass filtered between 25 and 1000 m. The alongshore variability of the trough was defined as the standard deviation of the linearly detrended intensity signal σ_{ti} along a defined line through the trough. For the outer bar, the trough line was determined by searching for the cross-shore minimum intensity between the outer and inner barline intensity maxima (see Figures 2.4a–c). In the case of an absent cross-shore minimum between the bar lines, indicative of a discontinuous trough, the cross-shore trough position was defined as being half way between the outer and inner bar. The resulting troughline was smoothed alongshore with a 150 m-wide Hanning window. The inner trough was determined in a similar way, but in between the inner barline intensity maximum and the shoreline. For cases where the inner bar was separated from the shoreline, which enabled the detection of another inner(most) bar, the troughline was defined between the inner barline and the new inner(most) barline. This mostly ephemeral inner(most) bar primarily occurred as an LTT and is not included in the analysis of the bar state dynamics. Thus, the outer bar/trough is defined as the most seaward bar/trough, whereas the inner bar/trough is defined as the next landward bar/trough.

To facilitate comparison of trough intensities between images with different contrasts (but identical morphology), image intensities along the defined trough line had to be re-scaled. For each image the offshore intensity, defined as the average intensity within an offshore region of 75 m cross-shore by 1500 m alongshore (Figure 2.4d) where wave breaking did never occur during the study period, and the mean barline

---

Figure 2.4 (following page) Extraction of the trough continuity for an alongshore (non-)uniform bar morphology. (a) Black and white (intensity) planview images of the study area, (b and c) cross-shore intensity profiles along the white lines indicated in (a), (d) intensity-adjusted planview image of the study area with the barlines, troughlines and shoreline, and (e) alongshore intensity profiles for the inner and (f) outer trough. The red (blue) stars in (a), (b) and (c) indicate the cross-shore location of the inner (outer) trough. The black lines in (e) and (f) correspond to the raw intensity values from (a) along the troughline, whereas the coloured lines in (d), (e) and (f) correspond to corrected intensity values from (d) for the inner (red) and outer (blue) trough. The white rectangles in (d) indicate the offshore area used for image intensity correction (see text for details).

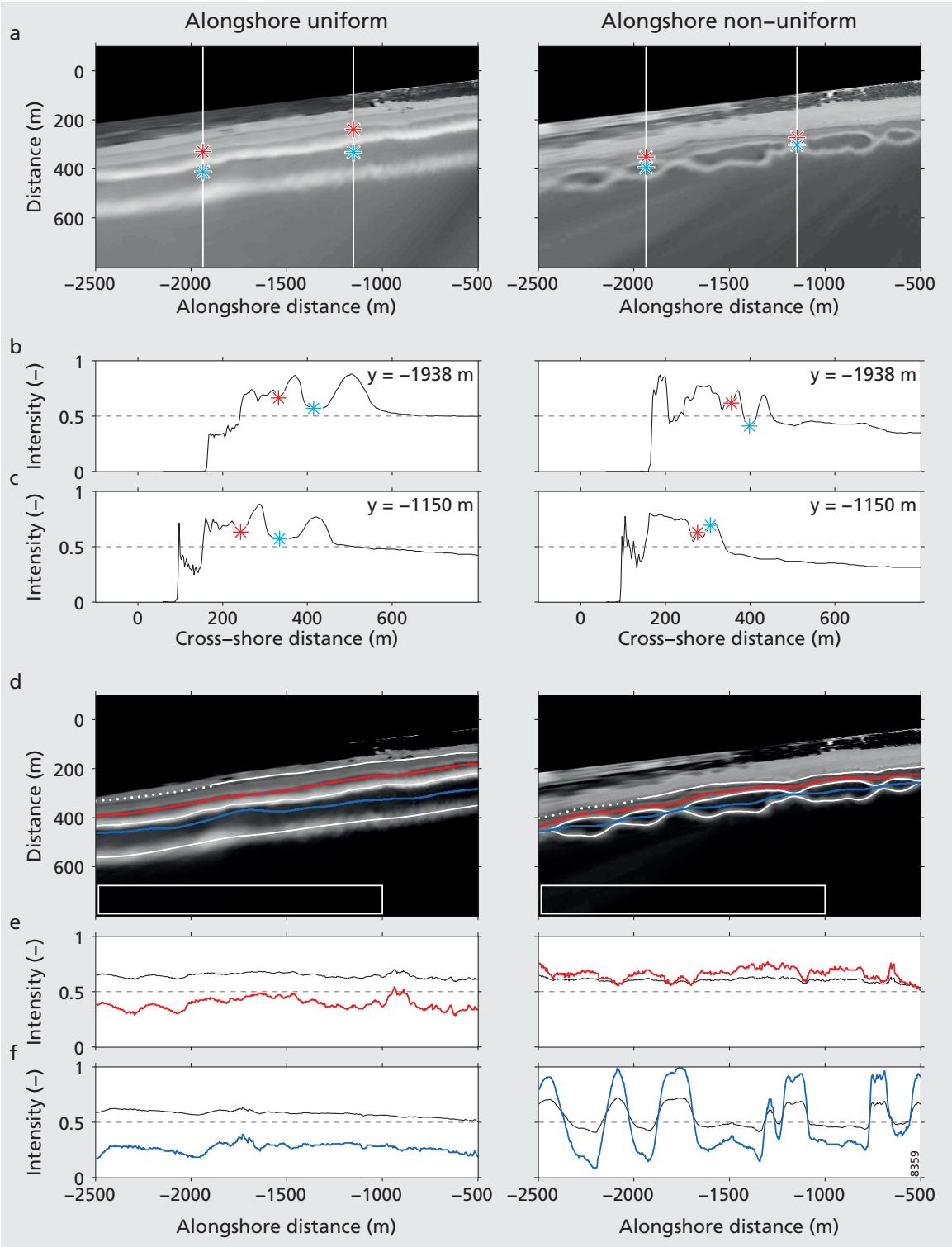
a
Alongshore uniform
Alongshore non–uniform
Distance (m)
0
200
400
600
–2500
–2000
–1500
–1000
–500
Alongshore distance (m)
b
Intensity (–)
1
0.5
0
y = –1938 m
c
y = –1150 m
0
200
400
600
Cross–shore distance (m)
d
e
f
8359

intensity served as the minimum (0) and maximum (1) intensity values, respectively. This way, the intensity of the trough is directly related to the intensity of the barline, providing an indication of the cross-shore amplitude of the bar and trough (Figure 2.4e–f), similar to Shand (2003). For all images, σ_{bp} and σ_{ti} of the inner and outer bar were extracted. Images with insufficient contrast (where the offshore intensity exceeded 0.75 times the barline intensity) were excluded, resulting in 1376 (1929) suitable images for the extraction of bar state features of the outer (inner) bar.

As described above, the alongshore variation of the trough is minimal in both the downstate and upstate extremes. To distinguish between the low variability of the trough intensity for these two cases, a distinction was made between continuous troughs and discontinuous troughs. After all, an almost continuous trough with several attached horns may yield the same intensity variation in the trough as a discontinuous trough with several rip channels. The bar states for these two cases, however, are not the same. Consequently, the more continuous (discontinuous) troughs are defined as possessing an average intensity along the troughline below (above) 0.5, half the maximum corrected image intensity. Subsequently, the alongshore trough continuity C_t is determined either by $C_t = 0 + \sigma_{ti}$ (for "dark" or more continuous troughs) or $C_t = 2\sigma_{ti(max)} - \sigma_{ti}$ (for "light" or more discontinuous troughs), where $\sigma_{ti(max)}$ is the maximum σ_{ti} for all available troughlines. For the outer (inner) trough, $\sigma_{ti(max)}$ did not exceed 0.4 (0.3). Consequently, completely continuous troughs correspond to $C_t = 0$ and completely discontinuous troughs correspond to $C_t = 0.8$ (0.6) for the outer (inner) trough. Hereafter, the value for trough continuity is simply referred to as σ_{ti}.

After quantifying σ_{bp} and σ_{ti}, bar states were defined for the classification of the data. A visual inspection of the available planview images indicated the presence of three states not available in the Wright and Short (1984) scheme. Firstly, both the inner and the outer bar were found to attain the aforementioned erosive eTBR state. This state was characterised by the presence of oblique rip channels and a straight barline (i.e. an alongshore uniform barline and a discontinuous trough; Figure 2.5a). Secondly, the inner bar was found to exhibit an LTT state with a quasi-rhythmic barline (i.e. an alongshore variable barline and a non-existent trough; Figure 2.5b), hereafter referred to as the rLTT state. Thirdly, the Wright and Short (1984) scheme does not include a decaying sandbar. As the decay is preceded by an extreme wave event (Section 2.2.1), we classify all decaying outer bars as dissipative (D). In total, 5 (6) bar states were defined for the classification of the outer (inner) bar. The inner reflective state R was defined as having a mean distance between the barline and the shoreline of less than 50 m. All other states were distinguished by classifying the data with a classification tree (Webb, 2002), which was trained with a sample set, consisting of 10% of the available data points equally distributed over parameter space (σ_{bp}, σ_{ti}) and subsequently pruned to prevent overfitting of the data (Figure 2.6). In total, the sample set of the outer (inner) bar contained 178 (196) images. The sampled images were visually (i.e. subjectively) classified. The separation between the outer bar RBB and TBR states was troubled by alongshore variability in the distance between the outer bar horns and the inner bar. In the end, it was decided to classify an outer

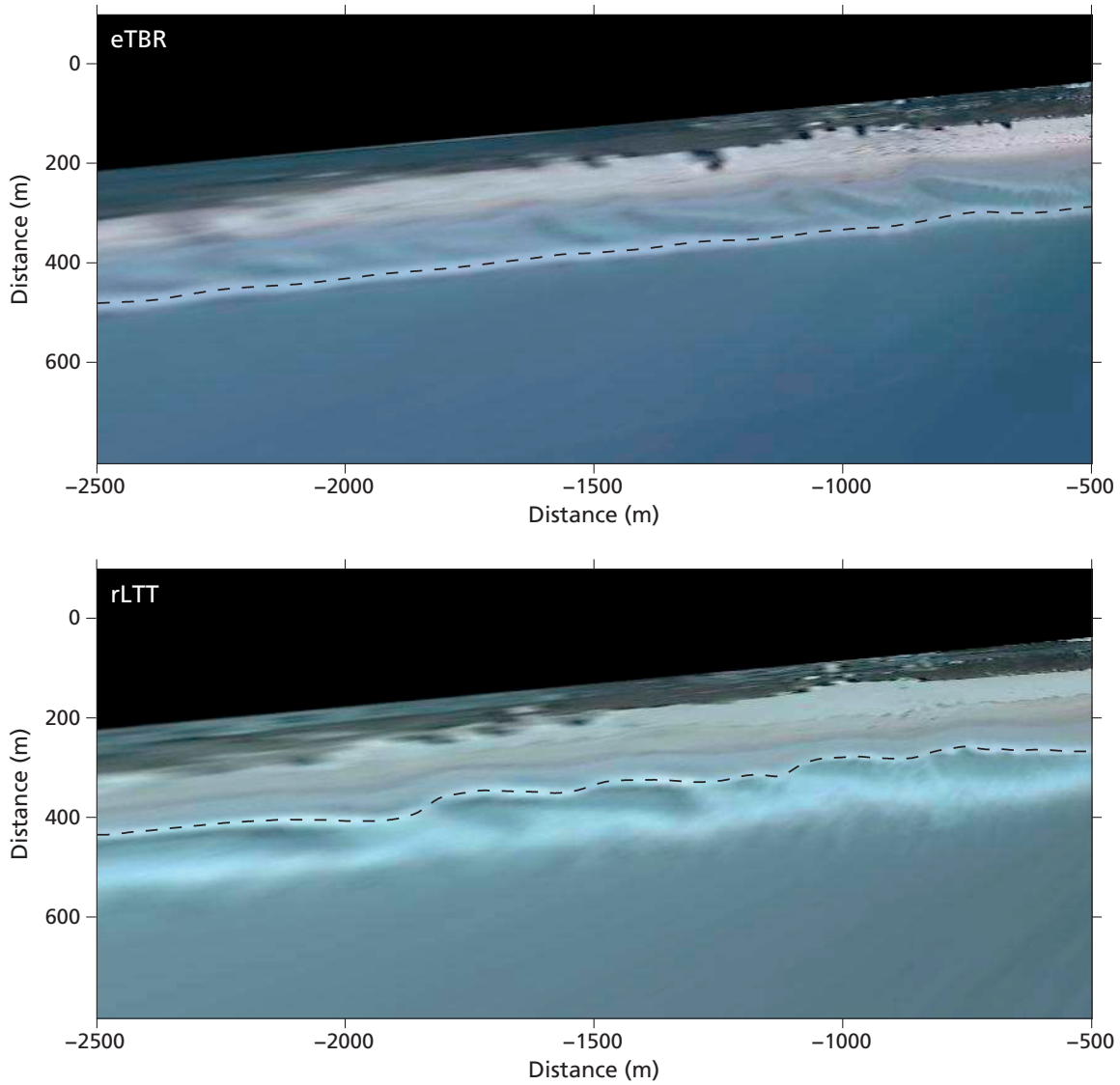

Figure 2.5 Planview images of the (here outer) eTBR state (a) and the (inner) rLTT state (b). The corresponding troughs lie landward of the indicated barline (dashed line).

bar as RBB when none of its horns were inner-bar attached. For the inner bar, the LBT and eTBR state could not be distinguished by the classification algorithm, and were therefore regarded as a single state. Table 2.1 (2.2) shows the performance of the classification algorithm for the sample set of the outer (inner) bar. Using 5% or 15% of the data for the sample did not alter the results of the classification scheme significantly. Previous studies involving the subjective classification of bar states have shown that there is generally a high level of agreement between the independent classifications (Lippmann and Holman, 1990; Ranasinghe et al., 2004; Armaroli and Ciavola, 2011). The classification of a subset of 280 outer bar states in our data by 3 experienced coastal scientists yielded a comparable level of agreement.

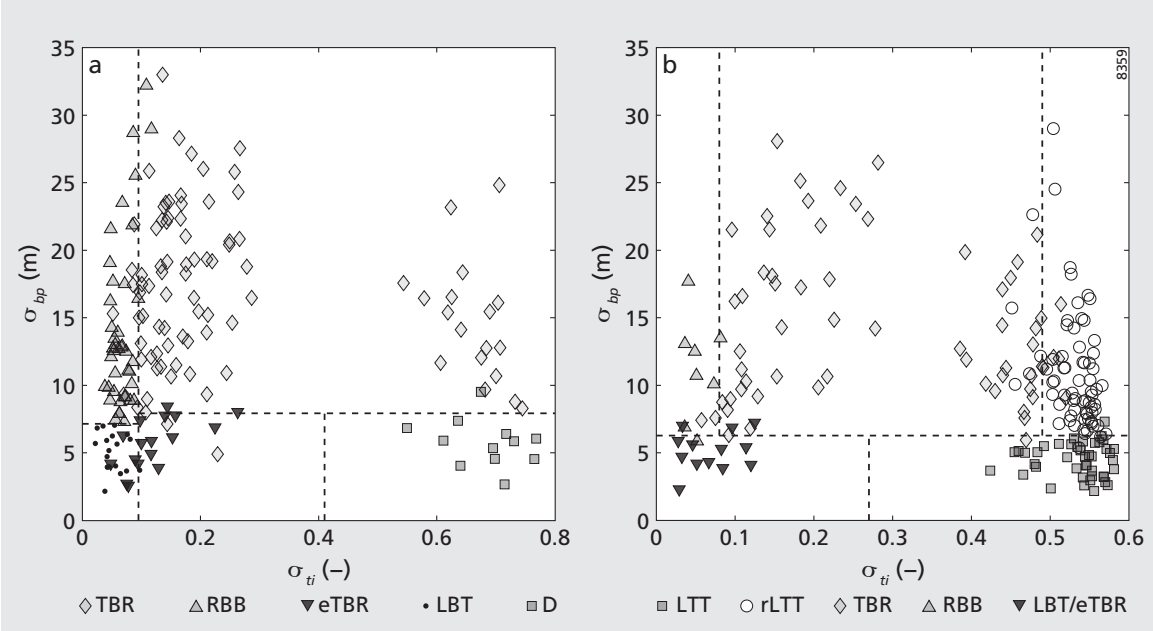

Figure 2.6 Decision trees applied for the classification of (a) the outer bar (178 images) and the (b) inner bar (196 images). The symbols represent the subjectively classified states. The performances of both classifications are provided in Tables 2.1 and 2.2, respectively.

Table 2.1 Performance of the classification algorithm for the sample set of the outer bar (178 images). The values correspond to the number of predicted states for each manually classified (i.e. observed) state.

	Predicted				
Observed	**D**	**LBT**	**eTBR**	**RBB**	**TBR**
D	11	0	0	0	1
LBT	0	18	1	0	0
eTBR	0	6	10	0	1
RBB	0	0	0	37	2
TBR	0	0	2	8	81

The classification algorithm resulted in 1376 (1929) classified outer (inner) bar states. Gaps in the data, due to the absence of (suitable) images, were filled through manual inspection of the images and the wave conditions. The states bordering gaps generally corresponded (70% of all gaps), and permitted the same state to be ascribed to the image(s) in the gap. In total, bar states were obtained for 96% (3258 days) of the study period. Remaining data gaps arose due to long periods (23 days on average) of unavailable images. Furthermore, the proximity of a bar state to a classification boundary may cause rapid bar state fluctuations between neighbouring classes. These apparent fluctuations were removed by manually adjusting ∼20% of the classified bar

Table 2.2 Performance of the classification algorithm for the sample set of the inner bar (196 images). The values correspond to the number of predicted states for each manually classified (i.e. observed) state. Note that the reflective state R is not included in the tree classification, as it is distinguished based on the mean distance between the barline and the shoreline.

	Predicted				
Observed	**LBT/eTBR**	**RBB**	**TBR**	**rLTT**	**LTT**
LBT/eTBR	10	1	2	0	0
RBB	1	7	0	0	0
TBR	0	2	56	4	1
rLTT	0	0	5	62	2
LTT	0	0	0	1	42

states. The resulting final time series of the inner and outer bar state classifications are shown in Figures 2.3g and h, respectively.

2.3.2 Bar state occurrence

Outer bar

Figures 2.7 a and b illustrate the frequency of occurrence and the associated residence times for the outer bar states, respectively. The outer bar was predominantly in the more downstate TBR (37% in time, 1231 days) and RBB (24% in time, 789 days) states, with a larger median residence time for the TBR state (24 days) than for the RBB state (13 days). Although the D state was observed less frequently (18%, 596 days) than the TBR state, the outer bar remained in this state for a long time (median value being 49 days). This state relates to the degenerative phase of the outer bar, where the subdued bar becomes inactive while slowly disappearing. The more upstate LBT was observed 14% in time (479 days), with a shorter median residence time (9 days) with respect to the more downstate intermediate states. Furthermore, the short residence time of the eTBR state (median value of 3 days), in combination with the infrequent occurrence (5% in time, 163 days), indicate the temporary nature of this particular state during (erosional) upstate transitions.

Inner bar

Figures 2.8 a and b illustrate the frequency of occurrence and the associated residence times for the inner bar states, respectively. The inner bar was generally more downstate than the outer bar. The rLTT state dominated in time (44%, 1448 days), although the corresponding median residence time (7 days) did not deviate significantly from the residence times of the other inner bar states, with median values of 3, 2, 6, and 5 days for the LBT/eTBR, RBB, TBR and LTT states, respectively. The R state was observed 12% in time, comparable to 6, 2, 20 and 14% in time

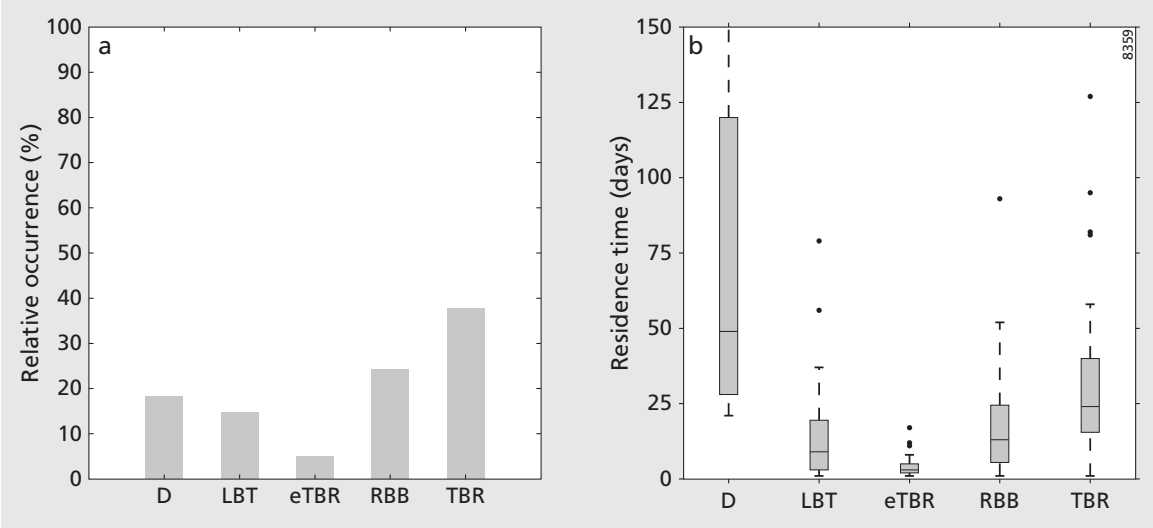

Figure 2.7 Outer bar states (a) and residence times (b) during the study period. The whiskers and dots of the box plots represent the range of extreme values within 1.5 times the interquartile range from the edges of the box and outliers beyond the whiskers, respectively.

for the LBT/eTBR, RBB, TBR and LTT states, whereas the corresponding median residence time of 39 days was clearly much larger than for the other states. The larger residence times of the TBR, rLTT, LTT and R states, indicate the persistent downstate nature of the inner bar. Moreover, the smaller residence times, compared to the outer bar state residence times, illustrate the mobility and variability of the inner bar morphology.

We found inner bar state dominance and residence time to depend on the state of the outer bar. Figures 2.8c and d show the inner bar states for intermediate outer bar states (states other than D). In this case, the inner bar state frequencies of occurrence and residence times were similar to those of the situation for all outer bar states, but with a shift toward more downstate configurations. This trend is most obvious from the decrease in TBR frequency (from 20% to 11%) and the increase in rLTT frequency (from 44% to 52%). Figures 2.8e and f show the inner bar states and residence times coinciding with the dissipative outer bar state D. In this case, the TBR state clearly became the most frequent inner bar state (60% in time). Furthermore, the inner bar was more frequently upstate than in the case for intermediate outer bar states, with the LBT/eTBR and RBB frequencies now adding up to 14% and 10%, respectively. Correspondingly, the inner bar was less frequently downstate (the R state was absent), compared to the situation for all outer bar states. The changes in frequency were also partly reflected by the median residence times, which were now 9 and 5 days for the TBR and rLTT states, respectively.

The above illustrates the influence the outer bar state had on the inner bar state. In general, the inner bar had a tendency to be more downstate with less continuous troughs (larger σ_{ti} values) for intermediate outer bar states. For the dissipative outer bar state D, however, the inner bar was more upstate with more continuous troughs

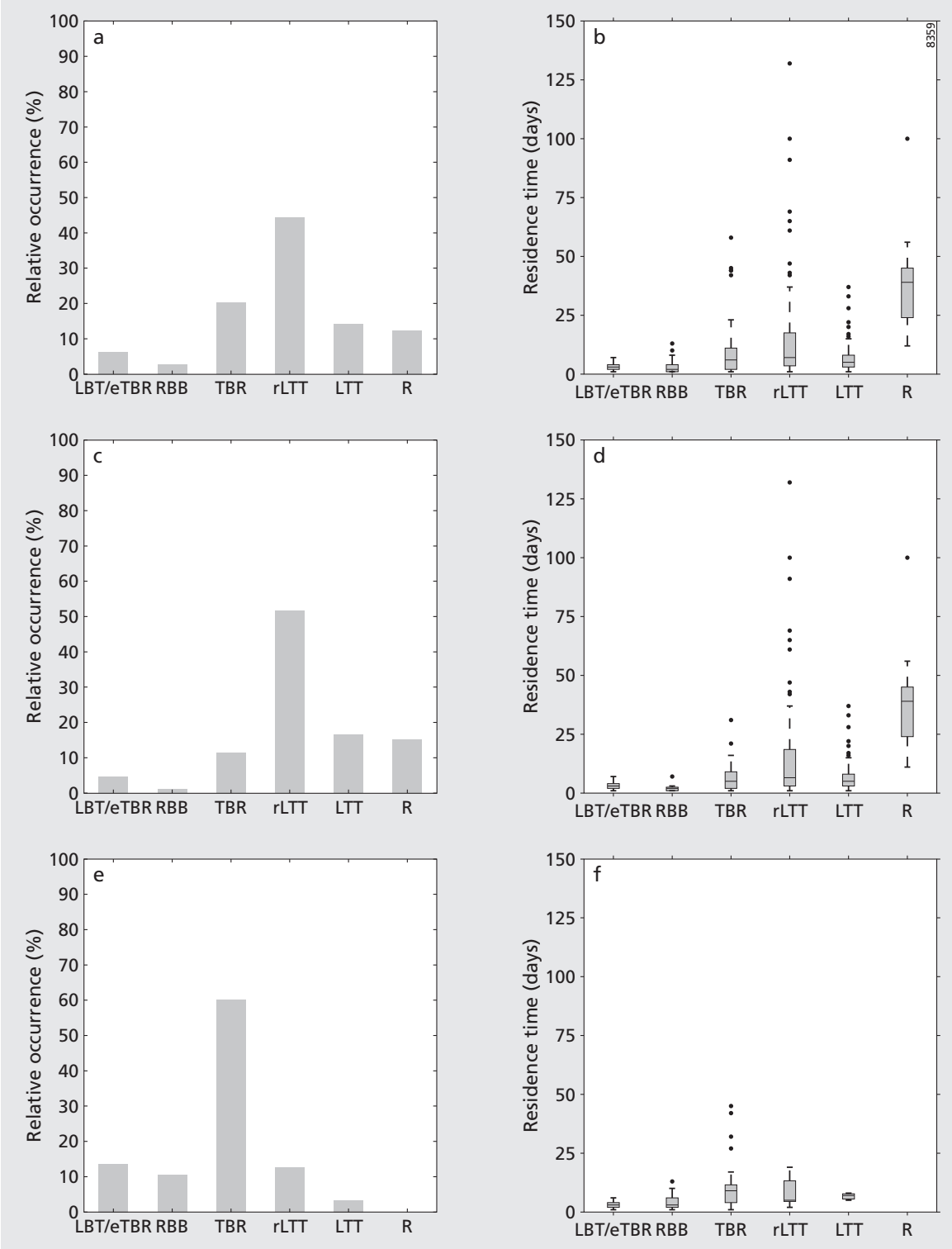

Figure 2.8 Inner bar states and residence times for all outer bar states (a and b; $N = 3258$), for intermediate outer bar states (c and d; $N = 2662$) and for the dissipative outer bar states (e and f; $N = 596$). The whiskers and dots of the box plots represent the range of extreme values within 1.5 times the interquartile range from the edges of the box and outliers beyond the whiskers, respectively.

Table 2.3 Transitions between outer bar states ($N = 145$).

	From				
To	**D**	**LBT**	**eTBR**	**RBB**	**TBR**
D		0	1	1	3
LBT	1		21	11	1
eTBR	0	0		5	27
RBB	1	33	5		3
TBR	1	0	5	26	

(smaller σ_{ti} values). The more upstate nature of the inner bar for this situation relates to the subdued geometry of the decaying outer D state allowing higher waves to reach the inner bar. Morphologically, this was mainly reflected by a shift from a terraced inner bar (with or without runnels) to an inner bar with well-developed rip channels.

Cross-occurrence
Figure 2.9 summarises the observed combinations of inner and outer bar states with examples of planview images. The corresponding frequency of the combined bar states are listed at the bottom of each panel. The most frequent combination of bar states was an outer TBR with an inner rLTT (observed during 787 days). The inner bar was clearly more downstate (TBR, rLTT, LTT and R) for intermediate outer bar states. The frequency of more upstate inner bar states, however, increases for more upstate outer bar states. Moreover, the subdued morphology of the outer D state (at the left top of the figure) coincided with more upstate inner bar states.

2.4 Bar state dynamics

2.4.1 Outer bar

State transitions
Table 2.3 summarises the transitions between the outer bar states during our study period. Upstate (downstate) transitions are provided above (below) the diagonal. Out of a total of 145 state transitions, 73 (72) were in upstate (downstate) direction. The most frequent downstate sequence was LBT–RBB–TBR, corresponding to the downstate sequence of Wright and Short (1984). In upstate direction, starting from the most downstate TBR, the most frequent sequence was TBR–eTBR–LBT; the TBR state changed to the alongshore uniform LBT through the eTBR state. Overall, the typical state sequence of the outer bar was LBT–RBB–TBR–eTBR–LBT. The dissipative state was occasionally reached (also shown in Section 2.3), after which the bar either disappeared or changed back to an intermediate state (also see Ruessink et al., 2009).

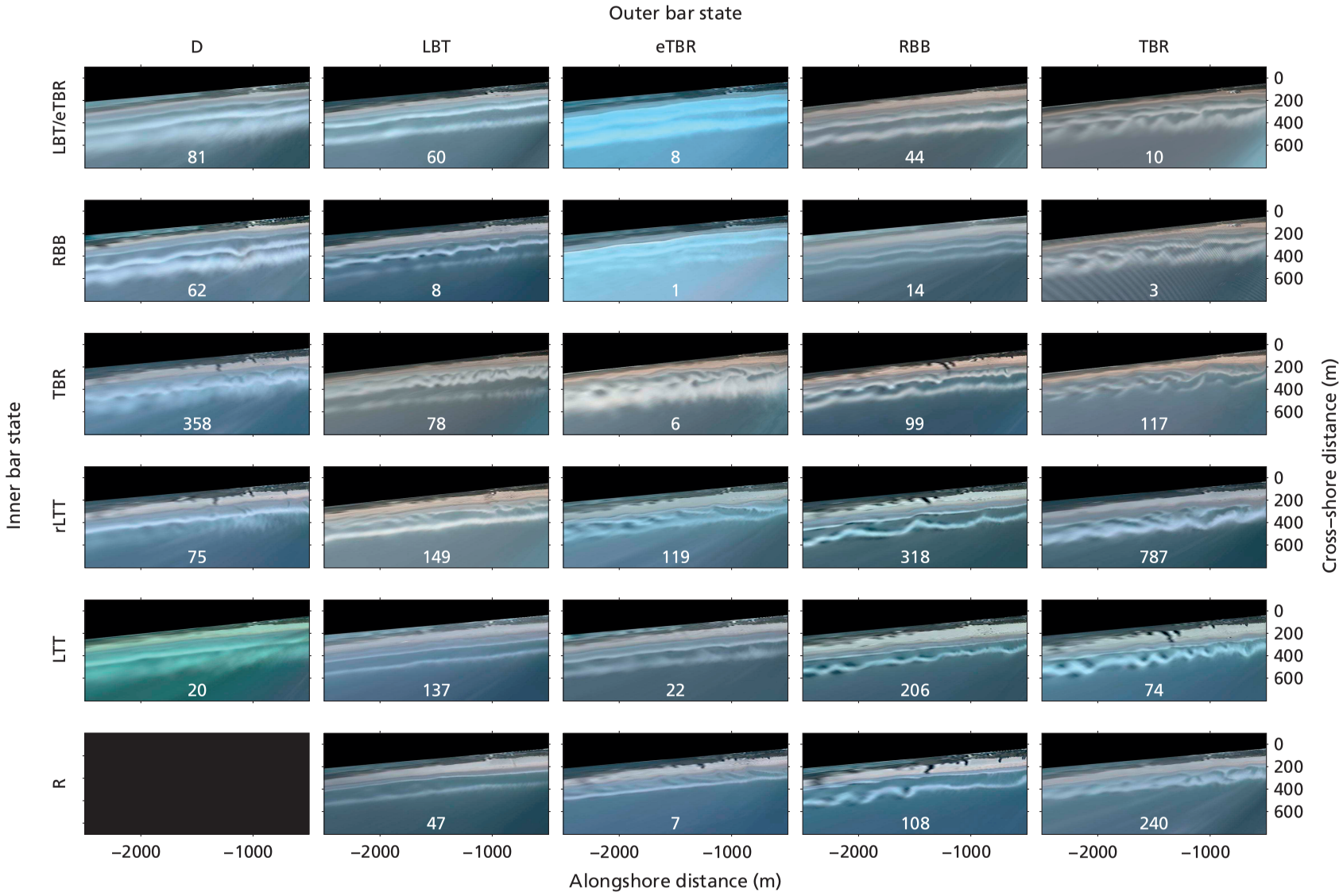

Figure 2.9 Observed combinations of the inner and outer bar states during the study period. The numbers at the bottom of each panel indicate the frequency (in days) of the observed combinations (3258 days in total).

Offshore forcing during state transitions

As described in Section 2.1, the existing literature indicates that upstate transitions are abrupt and are associated with high energetic events, whereas downstate transitions are gradual and happen during low energetic periods. Consequently, changes in bar state have mostly been ascribed to differences in e.g. wave height H, wave power P or the dimensionless fall velocity Ω (Wright et al., 1985; Lippmann and Holman, 1990; Van Enckevort and Ruessink, 2003; Ranasinghe et al., 2004, among others). To examine when the bars at the Gold Coast changed states, we explored whether these changes could be related to wave events. Herein, wave events are identified by means of the wave power P, which incorporates both H_{rms} and T_p, and suggested by Short (1979) as an important parameter governing morphological changes:

$$P = \frac{\rho g^2}{32\pi} H_{rms}^2 T_p \tag{2.1}$$

where ρ is the sea water density (1025 kg/m^3). Furthermore, recent observations have suggested the angle of wave incidence θ to play an important role in the straightening of the barline (e.g., Holman et al., 2006; Thornton et al., 2007; Strauss and Tomlinson, 2009; Almar et al., 2010). To analyse the effect of the dominantly oblique angle of wave incidence at our study site (see Section 2.2) during state transitions, we include the alongshore component of the wave power P_y, which represents the portion of the wave power available for alongshore sediment transport (Komar, 1998):

$$P_y = P \sin\theta \cos\theta \tag{2.2}$$

Time series of the hourly P and P_y are given in Figures 2.3d and e, respectively. We defined events as P exceeding 18 kW/m for a minimum duration of 12 hours. Inter-storm periods required a minimum time of 12 hours, to allow the identification of multiple peaks in P to be related to a single event. State transitions coinciding within an event were classified as abrupt transitions; all other state transitions are labelled as gradual transitions in the following. In total, 140 events were identified, with mean durations of 3–4 days.

Figure 2.10 illustrates a 2.5-month period in 2006, incorporating both abrupt and gradual transitions for the outer bar. Characteristic bar states during this period are shown in the planview images (Figures 2.10a–j), with time series of the bar states (Figure 2.10k), P and P_y (Figure 2.10l) below. At first, the outer bar is attached to the inner bar as a TBR (Figure 2.10a). During the first event ($\bar{P}$ = 14 kW/m, $\bar{H}_{rms}$ = 1.0 m) with obliquely incident waves ($\bar{P}_y$ = 5 kW/m, $\bar{\theta}$ = 42°) in the first half of July, the barline straightened and the bays became obliquely oriented, resulting in an outer eTBR state. The gradual re-attachment of the outer bar to the inner bar in the following period was interrupted by a slight increase in P and P_y, causing the outer barline to straighten (Figure b). The bar state returned to TBR as P_y decreased (Figure 2.10c). The large angle of wave incidence ($\bar{P}_y$ = 10 kW/m, $\bar{\theta}$ = 49°) during the second event ($\bar{P}$ = 22 kW/m, $\bar{H}_{rms}$ = 1.3 m), in the second half of July, coincided with the straightening of the outer barline and oblique orientation

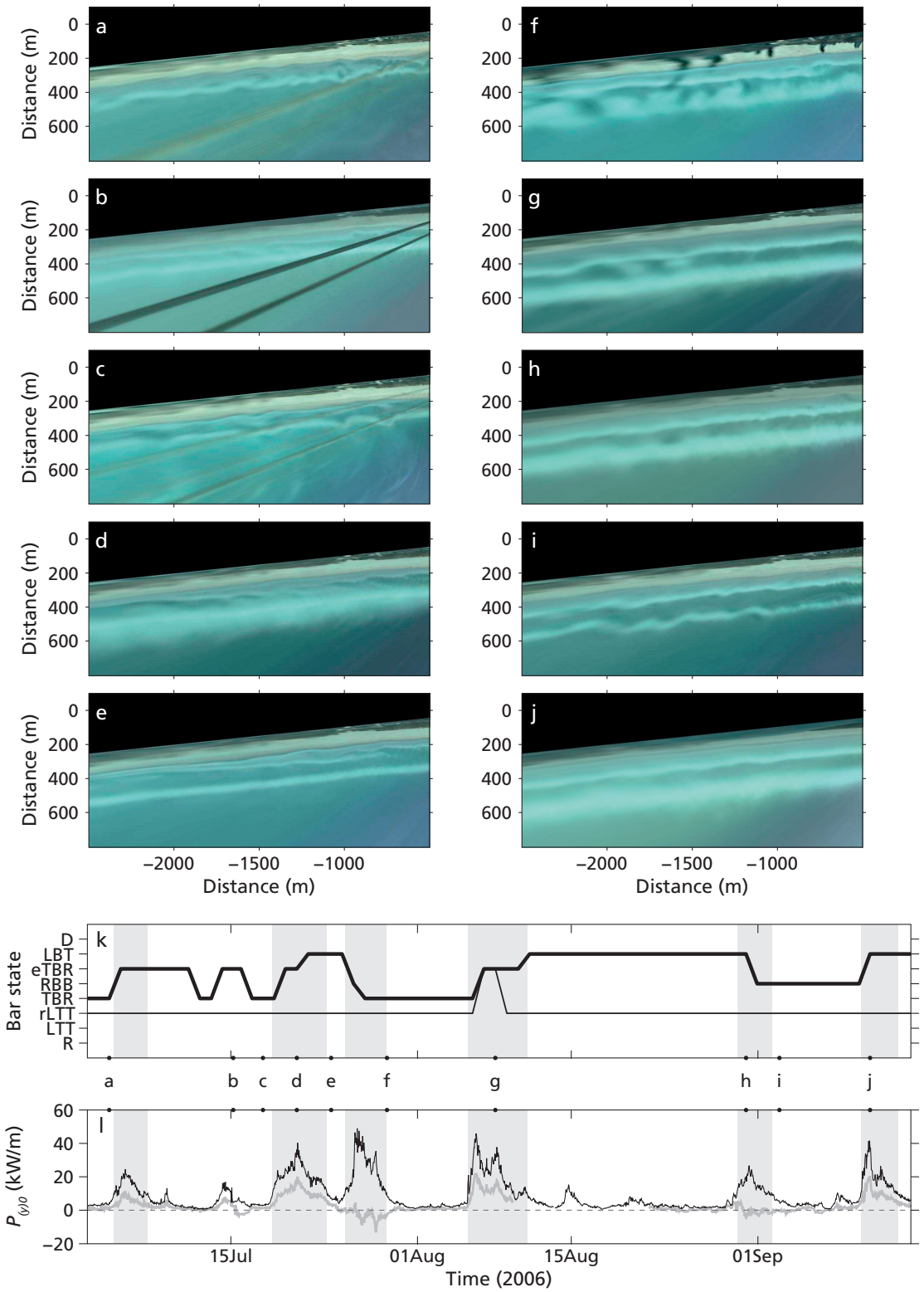

Figure 2.10 State transition examples showing (a–j) planviews, (k) outer (thick line) and inner (thin line) bar states, (l) wave power P (solid) and alongshore wave power P_y (grey). The identified events are indicated by the grey shaded areas.

of the bays associated with the previous outer TBR state (Figure 2.10d). At first, the horns remained attached to the alongshore variable inner bar. Eventually, the trough became completely continuous, resulting in an outer LBT state (Figure 2.10e). Shortly after, the most energetic event in this example ($\bar{P} = 25$ kW/m, $\bar{H}_{rms} = 1.6$ m) with more shore-normally incident waves ($\bar{P}_y = -3$ kW/m, $\bar{\theta} = -7°$) coincided with the development of crescentic patterns in the outer barline and the welding of the horns to the inner bar, the TBR state (Figure 2.10f). The outer bar remained in the TBR state until the following event ($\bar{P} = 21$ kW/m, $\bar{H}_{rms} = 1.3$ m) with obliquely incident waves ($\bar{P}_y = 12$ kW/m, $\bar{\theta} = 52°$) in the first half of August, which resulted in a transition from TBR to LBT through the eTBR state (Figure 2.10g). The outer bar remained in the LBT state during the subsequent low energetic period. During the following event ($\bar{P} = 15$ kW/m, $\bar{H}_{rms} = 1.3$ m) with almost shore-normally incident waves ($\bar{P}_y = 0.4$ kW/m, $\bar{\theta} = -1.6°$), at the end of August, the alongshore variability of the barline increased (Figure 2.10h) and the outer bar reached the crescentic RBB state (Figure 2.10i). Finally, obliquely incident waves ($\bar{P}_y = 10$ kW/m $\bar{\theta} = 44°$) during the last event ($\bar{P} = 20$ kW/m $\bar{H}_{rms} = 1.5$ m) resulted in an outer LBT state.

From the example above it follows that, besides the available wave power, the alongshore proportion of the wave power plays an important role in state transitions. Furthermore, both upstate and downstate transitions may happen either abruptly or gradually. Consequently, we examined each transition by averaging P and P_y over the period preceding the transition. For abrupt transitions the averaging period started at the beginning of the corresponding event or, if present, directly after the previous transition within the same event. Conversely, for gradual transitions, the averaging period started directly after the previous transition or, if present, directly after the previous event.

Figure 2.11 shows the resulting $\bar{P}$ and $|\bar{P}_y|$ for all abrupt and gradual state transitions. Upstate (downstate) transitions are provided above (below) the upper-left to lower-right diagonal. Upstate transitions are predominantly abrupt (52 out of 73 upstate transitions), whereas downstate transitions are mostly gradual (51 out of 72 downstate transitions), consistent with earlier observations (Short, 1979). *Gradual upstate* and *abrupt downstate* transitions, however, were also regularly observed. In downstate direction, the two most frequent abrupt transitions were from LBT to RBB (11 times) and from RBB to TBR (4 times), respectively. Gradual upstate transitions were mainly from TBR to eTBR (5 times), and from eTBR to LBT (11 times, more than the number of abrupt upstate transitions between these states). Transitions to the dissipative state coincided with the most energetic events, i.e. with the largest $\bar{P}$, but did not necessarily coincide with the largest $|\bar{P}_y|$. The difference between upstate and downstate transitions seems to lie less in the difference in $\bar{P}$, which may be of equal magnitude, but more in the difference in $\bar{P}_y$, which is generally smaller for downstate transitions.

Figure 2.12a shows $\bar{P}$ versus $|\bar{P}_y|$ for all abrupt transitions of the outer bar. Whereas $\bar{P}$ may be large for both upstate and downstate transitions, downstate transitions are mainly limited to $|\bar{P}_y| < 5$ kW/m. Correspondingly, $\bar{H}_{rms}$ ranges from 1–2 m for both upstate and downstate transitions, whereas downstate transitions are

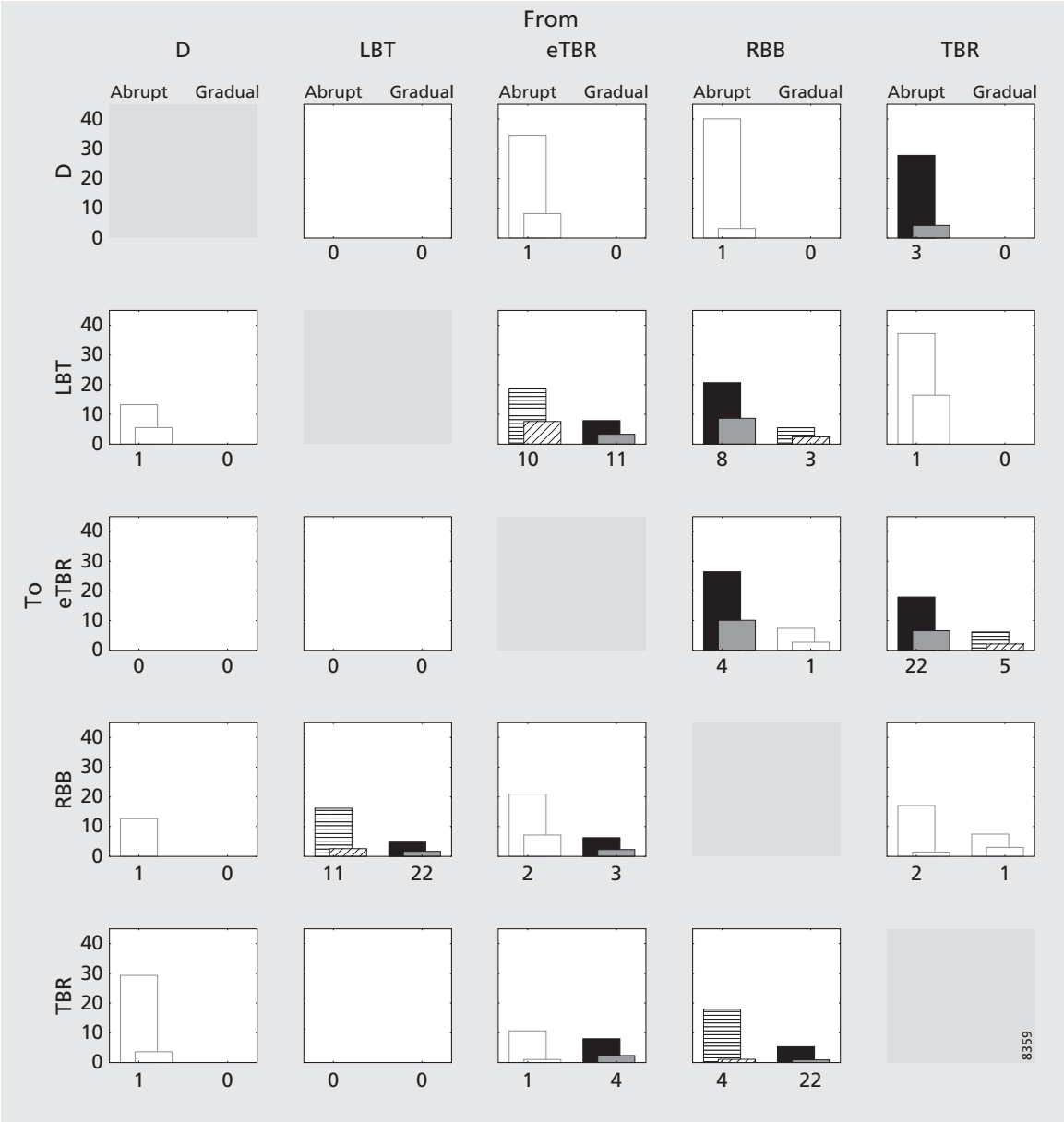

Figure 2.11 Mean wave power $\bar{P}$ (kW/m) and mean absolute alongshore wave power $|\bar{P}_y|$ (kW/m) for all abrupt and gradual state transitions of the outer bar. The transitions should be read from column to row. In each panel, the two left (right) rectangles correspond to abrupt (gradual) transitions. The black/grey (horizontally/diagonally striped) rectangles indicate the dominant (subordinate) transition mode; either abrupt or gradual. The frequency of abrupt and gradual transitions is indicated below each panel. Transitions with a frequency less than three times are indicated with white rectangles. In total, the outer bar changed state 145 times, out of which 73 abruptly and 72 gradually.

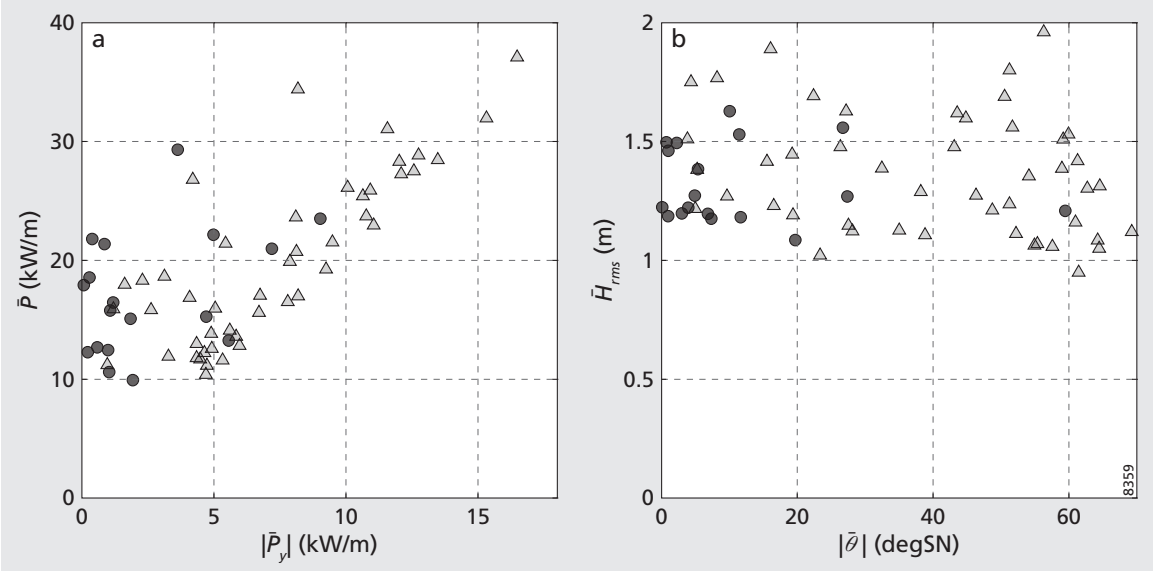

Figure 2.12 Mean wave conditions during abrupt downstate (circles) and upstate (triangles) transitions of the outer bar. (a) Mean wave power ($\bar{P}$) versus mean absolute alongshore wave power ($|\bar{P}_y|$) and (b) mean root-mean-square wave height ($\bar{H}_{rms}$) versus mean absolute angle of wave incidence ($|\bar{\theta}|$).

mostly limited to $|\bar{\theta}| < 30°$ (Figure 2.12b). Similarly, for gradual transitions (Figure 2.13), $\bar{P}$ ranges from 2–12 kW/m and $\bar{H}_{rms}$ ranges from 0.5–1 m for both upstate and downstate transitions. Figure 2.13b further shows that gradual upstate transitions are mainly limited to periods with $|\bar{\theta}| > 20°$.

Not every event resulted in a state transition. Despite that a bar state permits a certain amount of morphological variability without being classified differently (see Figure 2.6), the effect of the offshore wave forcing depends on the antecedent bar state. Based on Figures 2.12 and 2.13, the more upstate LBT would be expected to remain relatively unchanged during events with obliquely incident waves, whereas the more downstate (crescentic) bar states RBB and TBR would be expected to straighten during similar conditions to eTBR or LBT. For events with more shore-normally incident waves, however, the TBR state would be expected to remain unchanged and the RBB state may change to the TBR state. Figure 2.14 shows the mean offshore conditions for all events without transitions, for each state separately. Generally, the events without transitions were less energetic compared to the events with abrupt transitions in Figure 2.12. Whereas the upstate D, LBT and eTBR states permitted the more energetic events with obliquely incident waves (large $\bar{P}$ and large $|\bar{P}_y|$; large $|\bar{\theta}|$), the more downstate RBB and TBR permitted energetic events with more shore normally incident waves (large $\bar{P}$ and small $|\bar{P}_y|$; small $|\bar{\theta}|$). This supports the observation that up- or downstate transitions depend on the angle of wave incidence.

Summarising, upstate and downstate transitions of the outer bar may either happen abruptly, during moderately-energetic conditions ($\bar{P} \gtrsim 10$ kW/m, $\bar{H}_{rms} \gtrsim 1$ m), or gradually, during low-energetic conditions ($\bar{P} \lesssim 10$ kW/m, $\bar{H}_{rms} \lesssim 1$ m). The di-

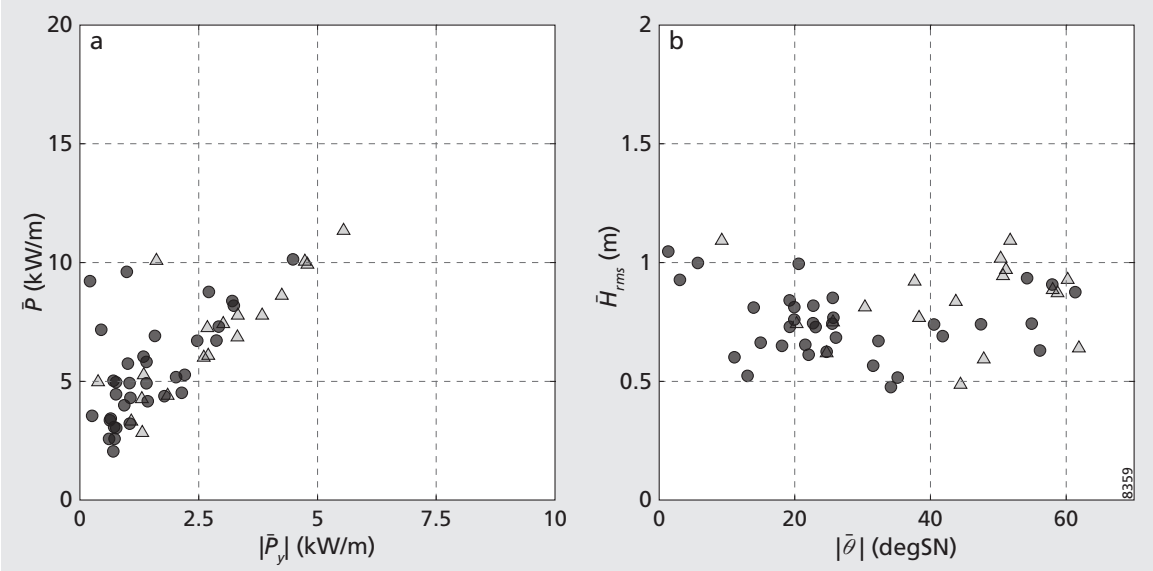

Figure 2.13 Mean wave conditions during gradual downstate (circles) and upstate (triangles) transitions of the outer bar. (a) Mean wave power ($\bar{P}$) versus mean absolute alongshore wave power ($|\bar{P}_y|$) and (b) mean root-mean-square wave height ($\bar{H}_{rms}$) versus mean absolute angle of wave incidence ($|\bar{\theta}|$). Note the different y-axis scale of (a) with respect to Figure 2.12a.

rection of bar state transitions (upstate or downstate) depends on the angle of wave incidence θ. *Abrupt downstate* transitions are mainly limited to $|\bar{\theta}| \lesssim 30°$, whereas *gradual upstate* transitions are mostly found for $|\bar{\theta}| \gtrsim 20°$.

2.4.2 Inner bar state dynamics

In total, the inner bar changed state 326 times (more than twice the amount of outer bar transitions; 145), of which 191 downstate and 135 upstate (Table 2.4). The main transitions were between LTT, rLTT and TBR, the most frequent inner bar states (see Figure 2.8). The inner bar regularly changed to the upstate LBT/eTBR state (63 times), after which it typically proceeded downstate through the sequence (RBB–)TBR–rLTT–LTT. Here, we do not distinguish between abrupt and gradual state transitions for the inner bar, as the continuously varying effect of the outer bar on the offshore wave forcing would have to be taken into account, which is beyond the scope of this paper. Instead, we aim to characterise the two types of inner bar state dynamics as distinguished in Section 2.3.2; for the well-pronounced intermediate outer bar states (states other than D) with a more downstate inner bar, and for the subdued dissipative outer bar state with a more upstate inner bar.

During periods with intermediate outer bar states, the inner bar became more downstate (upstate) 142 (101) out of 243 transitions. In accordance with the observations in Section 2.3.2 that the inner bar was more downstate for an intermediate outer bar, transitions were mainly between the more downstate R, LTT, rLTT and TBR (170 of 201 total transitions between these states). Upstate transitions from

Table 2.4 Transitions between inner bar states, for all outer bar states ($N = 326$).

To	*From* **LBT/eTBR**	**RBB**	**TBR**	**rLTT**	**LTT**	**R**
LBT/eTBR		2	34	16	11	0
RBB	25		0	1	0	0
TBR	29	24		18	3	0
rLTT	6	0	38		42	8
LTT	2	0	4	56		0
R	0	0	0	3	4	

Table 2.5 Transitions between inner bar states, for intermediate outer bar states ($N = 243$).

To	*From* **LBT/eTBR**	**RBB**	**TBR**	**rLTT**	**LTT**	**R**
LBT/eTBR		0	15	13	8	0
RBB	11		0	1	0	0
TBR	18	12		11	3	0
rLTT	6	0	29		42	8
LTT	2	0	2	55		0
R	0	0	0	3	4	

Table 2.6 Transitions between inner bar states, for the dissipative outer bar state ($N = 78$).

To	*From* **LBT/eTBR**	**RBB**	**TBR**	**rLTT**	**LTT**	**R**
LBT/eTBR		2	17	1	3	0
RBB	14		0	0	0	0
TBR	11	11		7	0	0
rLTT	0	0	9		0	0
LTT	0	0	2	1		0
R	0	0	0	0	0	

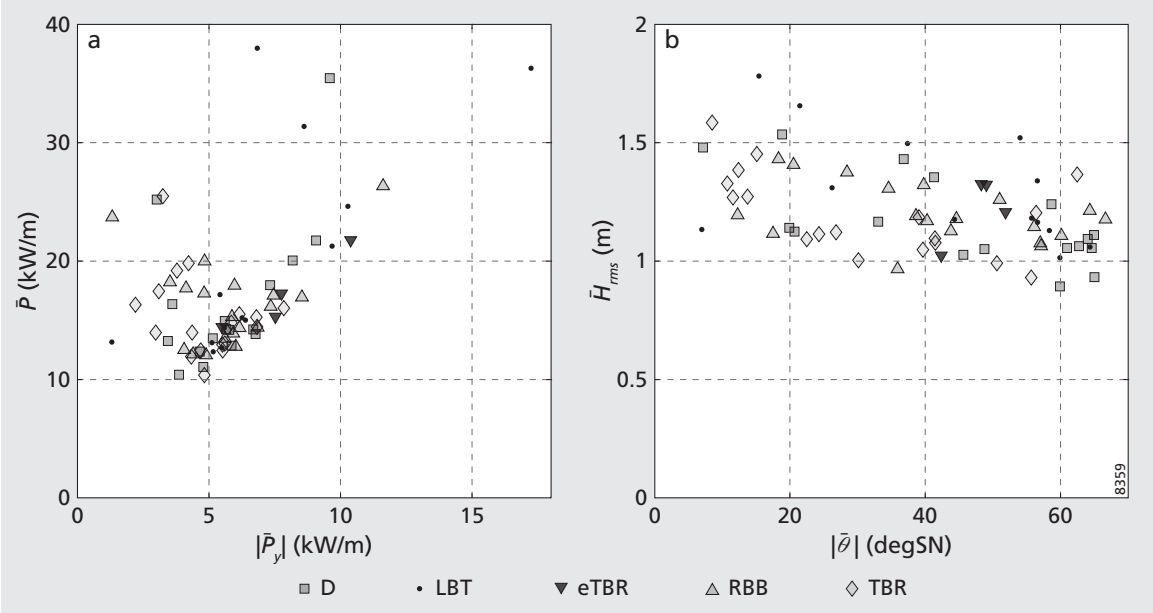

Figure 2.14 Wave conditions during events that did not lead to (abrupt) state transitions of the outer bar. (a) Mean wave power ($\bar{P}$) versus mean absolute alongshore wave power ($|\bar{P}_y|$) and (b) mean root-mean-square wave height ($\bar{H}_{rms}$) versus mean absolute angle of wave incidence ($|\bar{\theta}|$).

rLTT or TBR to LBT/eTBR were mainly succeeded by rapid downstate transitions, i.e. 'jumping' to the TBR, rLTT or LTT states. For the dissipative outer bar state (Table 2.6), however, transitions were mainly between the more upstate LBT/eTBR, RBB and TBR. Out of 78 transitions, 48 (30) were in downstate (upstate) direction. The dominant TBR state in this case (Section 2.3.2) generally changed to the more upstate LBT/eTBR (17 times) rather than downstate to rLTT (9 times). For intermediate outer bar states, on the other hand, the TBR state mostly proceeded downstate to rLTT (29 times) and, subsequently, from rLTT to LTT (55 times).

Figure 2.15 illustrates the two types of behaviour for the inner bar. For intermediate outer bar states (Figures 2.15a–g), the inner bar was generally in the rLTT state (Figure 2.15f), which mainly coincided with an outer TBR during the entire study period (see Figure 2.9). In this case, the inner barline is alongshore variable due to the attached horns of the outer TBR. Obliquely incident waves, causing the outer bar to proceed from TBR to LBT through the eTBR state, did not necessarily lead to the straightening of the inner barline. Instead, the horns of the former outer TBR state became part of the inner bar (Figure 2.15a), resulting in a rhythmicity in the inner barline related to the former alongshore variability of the outer bar. Similar behaviour was observed recently along the French Aquitanian coast by Almar et al. (2010). If the oblique wave incidence continued, the inner barline also straightened and changed from rLTT to either LBT/eTBR (Figure 2.15b; 7 out of 13 times) or LTT (13 out of 55 times). From the LBT/eTBR state, the inner bar either progressed to rLTT through TBR by infilling of the rip channels (Figure 2.15c), or 'jumped' back

to rLTT (6 times) or LTT (2 times) directly, as during the two succeeding events at the beginning of February and the beginning of March 2003 (Figures 2.15f and g). The LTT state was observed most frequently in combination with the detached outer LBT and RBB states (Figure 2.9). Accordingly, transitions to the inner LTT state mostly coincided with an outer LBT (17 of 59 times) and RBB (28 of 59 times), generally during more low-energetic periods such as in March 2003 (Figure 2.15d). When the crescentic outer RBB approached the inner bar, the inner barline started to develop rhythmicities similar to the outer barline (Figure 2.15e), as observed by Ruessink et al. (2007a). In total, transitions from an inner LTT to an inner rLTT coincided with an outer RBB (TBR) 19 (15) times out of 42.

For periods with a dissipative outer bar (Figures 2.15 h–n; after the extremely energetic event at the beginning of March 2006), the inner bar was generally in the TBR state (Figure 2.15n). The wide dissipation zone directly offshore of the inner bar in (Figure 2.15i) illustrates the subdued morphology of the outer bar. The bar regularly changed to the LBT/eTBR state (23 out of 78 total transitions; Figures i and l), after which it (Figure 2.15j) either remained detached from the shore as an RBB (14 out of 25 downstate transitions from LBT/eTBR) or (Figure 2.15k) returned to the TBR state (11 out of 25 downstate transitions from LBT/eTBR). The main consequence of a dissipative outer bar for the inner bar behaviour, with respect to an intermediate outer bar state, is the persistent development of rip channels (43 out 78 transitions, 55% as opposed to 52 out of 243 transitions, 21%) and frequent detachment from the shoreline (23 out 78 transitions, 30% as opposed to 36 out of 243 transitions, 15%).

2.5 Discussion

Using a 9.3-year data set of time-exposure images from the Gold Coast, Australia, we characterised the typical development of the alongshore variability of a double-barred sandbar system. Using the alongshore barline variability σ_{bp} and alongshore trough continuity σ_{ti}, we were able to objectively classify the inner and outer bar states from the images. Our classification algorithm provides an improvement to the classification of Browne et al. (2006) by directly including the alongshore variability of the bar morphology and provides an extension of the Ranasinghe et al. (2004) approach to a multiple bar setting. Besides the bar states from the Wright and Short (1984) classification scheme, we identified two additional bar states (see Figure 2.5). Both bars were found to attain the erosive transverse bar and rip (eTBR) state, characterised by the alongshore uniform barline and discontinuous trough with obliquely orientated rip channels, related to the dominant oblique angle of wave incidence at

Figure 2.15 (following page) Inner bar state transitions during intermediate (a–g) and dissipative (h–n) outer bar states, showing (a–e and h–l) planviews, (f and m) inner (thick line) and outer (thin line) bar states, (g and n) wave power P (solid) and alongshore wave power P_y (grey). Identified events are indicated by the grey shaded areas.

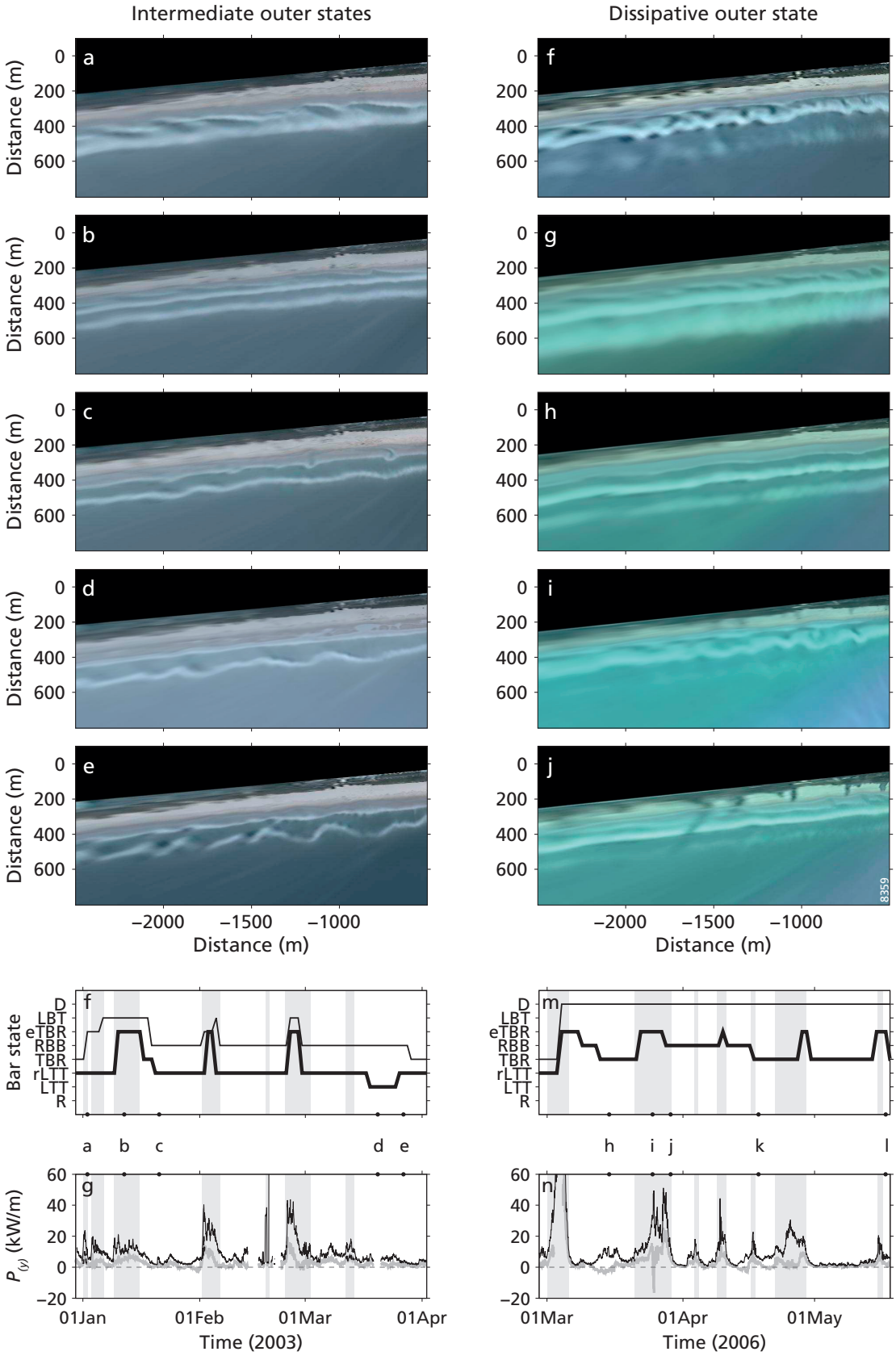
Intermediate outer states
Dissipative outer state
a
b
c
d
e
f
g
h
i
j
Distance (m)
0
200
400
600
−2000
−1500
−1000
Distance (m)
f
m
Bar state
D
LBT
eTBR
RBB
TBR
rLTT
LTT
R
a
b
c
d
e
h
i
j
k
l
g
n
$P_{(y)}$ (kW/m)
60
40
20
0
−20
01Jan
01Feb
01Mar
01Apr
01May
Time (2003)
Time (2006)

our study site (see Figure 2.3). Furthermore, the inner bar was dominantly observed as a rhythmic low tide terrace (rLTT), characterised by a quasi-rhythmic barline and a completely discontinuous trough (additionally with runnels). As discussed below, we think that this state is unique to multiple bar systems.

Whereas existing literature mainly relates state transitions to the amount of wave energy (either expressed through e.g. wave height H, wave power P or dimensionless fall velocity Ω), we find the angle of wave incidence θ to be of particular importance for state transitions. Bar straightening was not limited to high-energetic events and, similarly, the development of crescentic patterns was not limited to low-energetic periods. Instead, we found similar ranges in wave energy but different ranges in angle of wave incidence. The relation between upstate transitions and oblique wave incidence indicates the importance of the alongshore current for the straightening of the barline. This implies that morphological resets are not restricted to high-energetic events, but that a sufficiently powerful alongshore current may gradually create a continuous trough and straighten the barline. Our observation that energetic but shore-normally incident waves cause a downstate transition, rather than upstate, implies that (2DH) cell circulation remains important during highly energetic events with shore-normally incident waves.

We found the frequently occurring inner rLTT state to be a typical state of the inner bar in a double sandbar system. For dissipative outer bar states, during which the inner bar behaved more like a single-barred system, the rLTT state was only occasionally observed (Figure 2.8). The rhythmicity of the rLTT resulted from the interaction with the outer bar, either during downstate transitions of the crescentic outer bar (from RBB to TBR) or during upstate transitions (separation) of the attached outer bar (from TBR to eTBR), through inheritance of the outer bar horns. The latter emphasises the dependence of the inner bar morphology on the preceding morphology of the composite double bar system. Recent observations (Ruessink et al., 2007a) and model studies (Castelle et al., 2010a,b) showed that the inner bar patterns may (cor)relate to those of the outer bar. To adequately study the inner bar dynamics in relation to the composite bar system, the outer bar geometry (planview shape, alongshore depth variation and distance to the inner bar) together with the offshore wave forcing and the corresponding fraction of wave breaking (dissipation) over the outer bar should be taken into account. In the next chapter, therefore, we will (i) characterise the coupling between the inner and outer bar shapes, and (ii) explore the dependence of coupling on offshore wave conditions and the outer bar geometry.

2.6 Conclusions

Using the barline variability and trough continuity as morphological state indicators proved to be successful for determining the bar states within the double sandbar system at the Gold Coast, Australia. The outer bar was more upstate and generally advanced sequentially through the states LBT–RBB–TBR–eTBR–LBT, with occa-

sional transitions to the D state. Wave events led to abrupt state transitions of the outer bar, whereas obliquely (normally) incident waves resulted in upstate (downstate) transitions. The transition to LBT by means of the eTBR state highlights the role of high-angle waves and presumably the alongshore current in bar straightening. The outer bar was found to govern the state of the inner bar to a large extent. For intermediate outer bar states, the inner bar was mostly a shore-attached terrace with alongshore variability related to that of the outer bar. For dissipative outer bar states, however, the more upstate inner bar frequently separated from the shoreline and persistently developed rip channels. We suggest that increased insight into the inner bar dynamics would involve the quantification of (the alongshore variability of) wave breaking over the outer bar.

Acknowledgements

T.D. Price and B.G. Ruessink acknowledge financial support by the Netherlands Organisation for Scientific Research (NWO), under contract 818.01.009. We would like to thank Roshanka Ranasinghe and Giovanni Coco for providing independent beach state classifications of the image sample.

3 Observations and conceptual modelling of morphological coupling in a double sandbar system

Based on: Price, T. D. and Ruessink, B. G. (in press), Observations and conceptual modelling of morphological coupling in a double sandbar system. Earth Surface Processes and Landforms.

3.1 Introduction

Nearshore sandbars, located in < 10 m water depth, can contain remarkably periodic alongshore undulations in both cross-shore position and depth. These so-called crescentic sandbars can be seen as a sequence of shallow horns (shoals) and deep bays (cross-shore troughs) alternating landward and seaward, respectively, of an imaginary line parallel to the coast. The spacing between the horns varies from several tens of metres to several hundreds of metres (Van Enckevort et al., 2004). These horns and bays are thought to form spontaneously as a result of the positive feedback between horizontal cell circulation patterns, including rip currents, sediment transport, and the morphology itself (Falqués et al., 2000). In a double sandbar system, the alongshore spacing of seaward and landward perturbations in the inner bar may be identical to the horn spacing in the outer sandbar, contrasting with their supposed spontaneous development with different length scales (Smit et al., 2008; Castelle et al., 2010a). Instead, the inner-bar features appear to be morphologically coupled to those in the outer bar. This coupling is similar to the commonly observed correspondence between crescentic sandbars and shoreline perturbations (e.g., Sonu, 1973), resulting in an alongshore alternation in beach width and, consequently, in dune erosion (Komar and Rea, 1976; Thornton et al., 2007). Although this morphological coupling between sandbars has been observed previously (e.g., Bowman and Goldsmith, 1983; Castelle et al., 2007a), its ubiquity and dynamics remain largely unexplored.

On the one hand, in the observations of e.g. Hom-ma and Sonu (1962) and Bowman and Goldsmith (1983), no phase coupling was observed, even when outer-bar horns were welded to an inner bar. Recent observations (see Ruessink et al., 2007a and Section 2.4.2) and modelling efforts (Castelle et al., 2010a,b), however, have indicated that the morphodynamic feedback driven by the geometry of the outer sandbar might be a critical parameter governing the behaviour of the composite bar system. In the observations of Van Enckevort and Wijnberg (1999) the inner- and outer-bar horns were coupled out-of-phase (that is, an outer-bar horn facing an inner-bar sea-

ward bulge), a situation reminiscent of the commonly observed (180°) out-of-phase coupling between bar patterns and shoreline perturbations (e.g., Komar, 1971; Sonu, 1973; Orzech et al., 2011). In-phase coupling (with an outer-bar bay facing an inner-bar landward perturbation), on the other hand, has also been observed (Bowman and Goldsmith, 1983; Castelle et al., 2007a). Ruessink et al. (2007a) analysed 8 weeks of daily low-tide time-exposure images of a double sandbar system obtained at the Gold Coast, Australia. They found that the inner bar increasingly coupled to the outer-bar shape as the outer bar became more crescentic and migrated onshore, i.e. during a downstate transition of the outer bar from the alongshore uniform Longshore Bar and Trough (LBT), through the Rhythmic Bar and Beach (RBB) to the Transverse Bar and Rip (TBR) state (Wright and Short, 1984). The initially featureless terrace-shaped inner bar, i.e. Low-Tide Terrace (LTT), developed an alongshore variability coupled to the outer-bar shape. In Chapter 2 we termed this inner-bar state the rhythmic LTT, rLTT. Besides the morphological coupling during downstate transitions, coupled features have been found to persist during upstate transitions of the outer bar, during which the outer bar straightens. In this case, the outer bar may shed its horns, which subsequently migrate onshore and become part of the inner bar (Wijnberg and Holman, 2007; Almar et al., 2010). Previous observations of sandbar coupling were based on either sporadic observations (e.g., Short and Aagaard, 1993) or a single event of sandbar coupling (e.g., Ruessink et al., 2007a). Although this previous work has provided clear examples of the phenomenon of sandbar coupling, the frequency or predominance of either of the coupling patterns remains unclear.

Castelle et al. (2010a,b) used numerical simulations of a double sandbar system with a crescentic outer bar to study the flow patterns leading to coupled inner-bar features. They found that coupled inner-bar features arise from horizontal circulation patterns driven by alongshore variations in wave refraction and wave breaking across the crescentic outer bar. The alongshore variability in outer-bar depth was found to be crucial to the development of the coupled inner-bar morphology, causing the bars to couple either in-phase or out-of-phase. Whereas these simulations were done for shore-normally incident waves, field observations of the flow patterns over crescentic sandbars (Sonu, 1972; MacMahan et al., 2010) indicate a change from horizontal circulation patterns to meandering alongshore currents as the angle of wave incidence increases. Ruessink et al. (2007a) found coupled sandbar patterns with a 90° phase shift, thought to be related to the persistent nonzero angle of wave incidence at their study site. Quartel (2009) observed coupling of the intertidal morphology to the subtidal alongshore variability, with the phase between the two bar variabilities varying from in-phase (0°) to out-of-phase (180°), with gradual phase changes due to larger alongshore migration rates of the subtidal bar with respect to the intertidal bar.

Here, we use a multi-year data set of daily video images from the double-barred Gold Coast (Queensland, Australia) to (i) quantify the frequency of occurrence of coupled sandbars, (ii) distinguish the different types of coupling, and (iii) explore the dependence of coupling types on offshore wave conditions, in particular the angle of wave incidence. We start off with a description of the field site and methodology

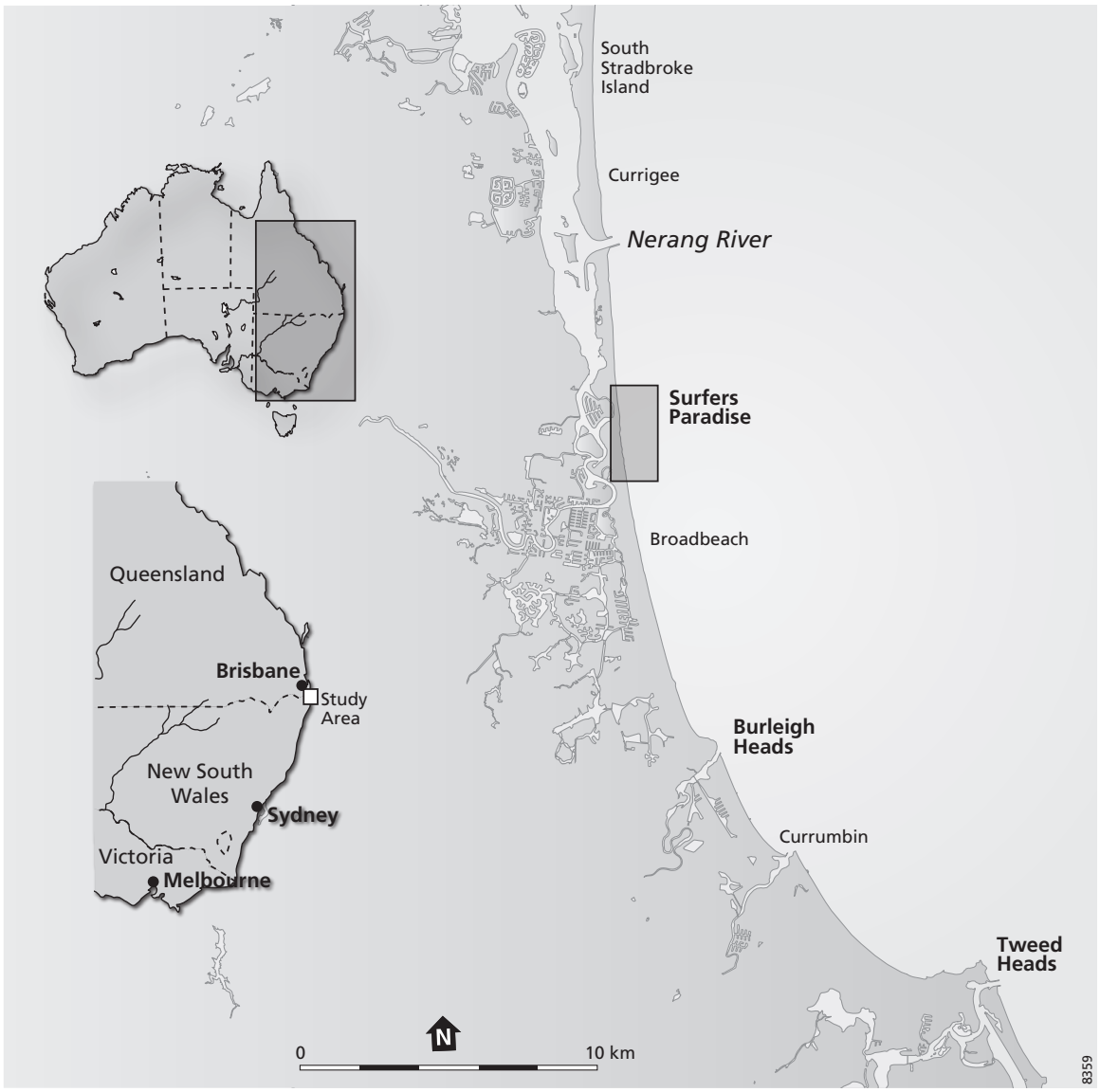

Figure 3.1 Location of the study site.

(Section 3.2). Results, a preliminary version of which was provided by Price et al. (2011), can be found in Section 3.3. We present a conceptual model on sandbar coupling in Section 3.4, and finalise the paper with the main conclusions in Section 3.5.

3.2 Methods

3.2.1 Field site

We studied the sandbars of the double-barred beach at Surfers Paradise, located at the northern end of the Gold Coast in south-east Australia (Figure 3.1; Turner et al., 2004). The frequent changes in sandbar morphology at this site, presented

in Chapter 2, in combination with the long period of daily observations, make this site specifically suitable for studying the composite behaviour of the coupled sandbar patterns. The study site is a wave-dominated, 2.5-km long straight stretch of beach, located toward the northern end of the 20 km of continuous coastline that extends from Burleigh Heads in the south to the trained Nerang river entrance 5 km further north. The Gold Coast is exposed to persistent south-easterly swells (30° shore-normal on average), resulting in a corresponding downdrift (northward) net annual sediment transport of about $500,000$ m^3 (Patterson, 2007). Hourly root mean square wave height H_{rms}, peak wave period T_p and angle of wave incidence θ were obtained from nearby wave buoys (see Ruessink et al., 2009). The mean H_{rms} at the Gold Coast wave rider buoy (at 18 m depth) is 0.8 m with an estimated return interval of 2 years for a H_{rms} of 2.5 m, and a mean T_p of some 9 – 10 s. The nearshore is composed of predominantly quartz sand with a median grain size of 250 μm, and has a bed slope of 0.02. A hybrid coastal protection-surfing reef structure is located just north of the study site (Turner et al., 2004), at an alongshore distance of about 1000 m.

In Chapter 2 we classified both the inner and outer bar in five possible morphodynamic states. These states include the aforementioned LBT, RBB, TBR (the modal outer-bar state at Surfers Paradise) and LTT. For the outer bar, they further distinguished the dissipative D state, during which the outer bar disintegrated following a major storm (Ruessink et al., 2009). The fifth state comprised highly oblique rip channels, often with a more-or-less uniform bar. This state, which we referred to as the erosional TBR (eTBR), forms the upstate transition from TBR to LBT during wave events with a large angle of incidence. Furthermore, the inner bar obtained a state exhibiting a terraced morphology with alongshore undulations of the terrace edge. We referred to this state as the rhythmic LTT (rLTT); it was the modal inner-bar state. The alongshore wavelength of the inner-bar rLTT was often similar to that of the outer bar, implying some sort of morphological coupling.

3.2.2 Video imaging

From 15 July 1999 to 29 October 2008 (9.3 years), an Argus coastal imaging station (Holman and Stanley, 2007) was installed at an elevation of 100 m above mean sea level. The system consists of four cameras pointed obliquely along the beach, providing 180° uninterrupted coverage of the northern Gold Coast region (Turner et al., 2004). Each daylight hour the system routinely collected a 10-min time-exposure image for every camera, created by the averaging of 600 individual snapshots sampled at 1 Hz. The pixel footprint amounts to 2×0.5 m (cross-shore $\times$ alongshore) in front of the cameras and worsens to about 8×30 m at the southern end of the field site, at 2500 m from the cameras. All four images were rectified (Holland et al., 1997) and merged to obtain planview images with a grid resolution of 2.5×2.5 m spanning 5000 and 900 m in longshore and cross-shore direction, respectively. For this study, we used the southernmost 2.5 km of the beach in range of the cameras (from $y = -2500$ to $y = 0$ m, where y is the local alongshore coordinate), motivated by the presence of the artificial surfing reef to the north (at $y \approx 1000$ m).

The basic premise behind the video-imaging system to infer the planview sandbar shape is the preferential wave breaking over shallow features, creating foam on the water surface (Lippmann and Holman, 1989). This enables the detection of sandbars through the areas of high intensity in the time-exposure images. Accordingly, we extracted the optical breaker line (hereafter referred to as the barline) of both the inner and outer bar from all the available images by the automated alongshore tracking of the intensity maxima across each bar (Van Enckevort and Ruessink, 2001; Pape et al., 2010). To minimise the apparent (cross-shore and alongshore) barline variability related to changes in tidal water level (see e.g., Van Enckevort and Ruessink, 2001; Pape et al., 2010), we used low-tide images only. The acquired barlines were linearly detrended and band-pass filtered between 25 and 1000 m before further analysis. Henceforth, these detrended and filtered barlines are referred to as the barline perturbations $X_p(y,t)$. In total, this study spans 3395 days (9.3 years). During this period, images were sometimes unavailable due to malfunctioning of one or more of the cameras (400 days), reducing the total number of images available for barline extraction to 2995.

3.2.3 Cross-correlation

As shown by Van Enckevort and Wijnberg (1999) and Ruessink et al. (2007a), cross-correlation provides a suitable technique for detecting coupled inner and outer barlines. The cross-correlation function of two barlines x_n and y_n, $n = 0 \cdots N-1$, at lag m is

$$r_{xy}(m) = \frac{R_{xy}(m)}{\sqrt{R_{xx}(0)R_{yy}(0)}}, \tag{3.1}$$

where N is the total number of alongshore points, and R_{xy} is the autocovariance function

$$R_{xy}(m) = E[(x_{n+m} - E(x))(y_n - E(y))], \tag{3.2}$$

in which E is the expected value operator, and R_{xx} and R_{yy} are the autocovariance functions of x_n and y_n, respectively. The lag m at the (absolute) largest significant correlation indicates the alongshore displacement of the inner-bar features with respect to those of the outer bar, where positive (negative) lags coincide with a displacement of the inner-bar features to the south (north). A positive correlation ($r_{xy} > 0$) coincides with in-phase coupling, whereas negative correlations ($r_{xy} < 0$) correspond to out-of-phase coupling. The test for statistically significant nonzero correlation was performed using a reduced number of effective points N_{eff}, following Garrett and Toulany (1981):

$$\frac{1}{N_{eff}} = \frac{1}{N} + \frac{2}{N^2}\sum_{j=1}^{N_0}(N-j)R_{xyxy}(j), \tag{3.3}$$

where $R_{xyxy}(j)$ is the autocovariance of the detrended product of the two barlines to be correlated, and N_0 is the number of lags until R_{xyxy} experiences a zero-crossing.

3.2.4 Depth variations

As mentioned in the Section 3.1, the depth variation of the outer bar has previously been hypothesised to be an important parameter leading to coupled inner and outer sandbar morphology. Bathymetric data was collected too infrequently (Ruessink et al., 2009) to be of use to our study and we, therefore, estimated bathymetric evolution from time series of time-exposure images. Image intensity can be seen as a proxy for the roller dissipation D_r (Aarninkhof et al., 2005; Van Dongeren et al., 2008), allowing the underlying bathymetry to be estimated through model-data assimilation. We applied the assimilation model XBeachWizard (Van Dongeren et al., 2008), which uses a least-squares estimator approach to estimate the bathymetric evolution from a series of time-exposure images in combination with the process-based numerical model XBeach (Roelvink et al., 2009). Following the method as outlined in Van Dongeren et al. (2008), we applied XBeachWizard to explore the depth variations along the outer bar for three coupling events, further described in Section 3.3.3. The details of the image preprocessing and assimilation setup required to apply XBeachWizard are discussed in Appendix A. We note that XBeachWizard also produces an uncertainty estimate σ for each depth, see Van Dongeren et al. (2008) for details.

Depth estimates of the outer bar $z(y,t)$ were taken along the acquired barlines (see Section 3.2.2), averaged over a cross-shore distance around the barline position. We found the bar (shallowest location) in the estimated bathymetry to be positioned landward of the (video-derived) barline, motivating our choice for to average the depth from 2.5 m (1 pixel) seaward to 12.5 m (5 pixels) landward of the barline position. Depth perturbations along the barlines $z_p(y,t)$ were obtained by subtracting the alongshore-averaged depths $\bar{z}(t)$ from the depth estimates along the outer barlines $z(y,t)$. As a measure of variability in $z_p(y,t)$, the difference in the 5^{th} and 95^{th} percentile at each t was taken and denoted as $\Delta z_{\{5,95\}}(t)$.

3.3 Results

3.3.1 Cross-correlation results

Figure 3.2 shows the cross-correlogram resulting from the cross-correlation of the 9.3-year data set of inner and outer barlines. A positive (negative) correlation, indicated by the red (blue) colours, corresponds to in-phase (out-of-phase) coupling. The black contours indicate the 98% confidence level for statistically significant coupling. To aid in the interpretation of Figure 3.2, we will first describe coupling in relation to the morphologic outer-bar state. Figure 3.3 shows the frequency of the bar states for both coupled and non-coupled barlines. During coupling, the outer bar was mostly in either the RBB (28% of all coupled events) or TBR (40%) states (Figure 3.3a). Note that a crescentic outer bar did not necessarily lead to a coupled inner barline (Figure 3.3b). Similarly, in-phase coupling mainly coincided with outer RBB (32%) or TBR (35%) states (Figure 3.3c), whereas during out-of-phase coupling the outer sandbar was dominantly (80%) attached to the inner sandbar (i.e. the TBR state; Figure 3.3d). The eTBR state is the least observed during coupling, which

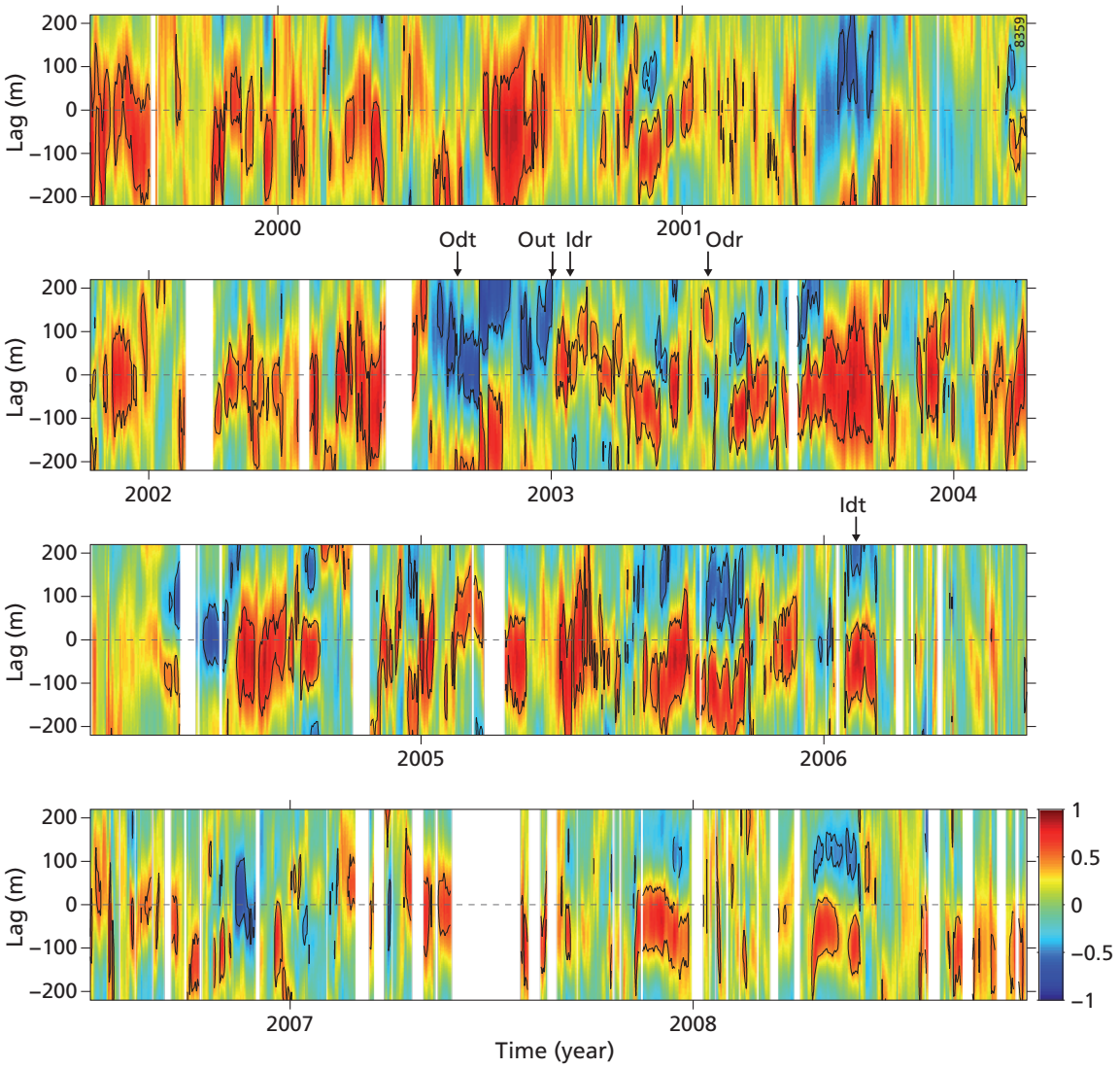

Figure 3.2 Cross-correlogram of the inner and outer barlines for the entire study period. A positive (negative) correlation r_{xy}, indicated by the red (blue) colours, corresponds to in-phase (out-of-phase) coupling. The black contours indicate the 98% confidence level for statistically significant coupling. The arrows indicate the examples from Figure 3.5.

relates to the highly transient character of this state as the bar progresses toward the alongshore uniform LBT state. As the amplitude of the barline is normalised during cross-correlation, even small undulations in (seemingly) straight barlines may be significantly correlated. Consequently, cross-correlation also yielded some significantly coupled barlines for the inactive dissipative D and alongshore uniform LBT outer-bar states (Figure 3.3a). Accordingly, for the further analysis of morphological coupling in this paper, we disregard these states and consider outer sandbars with a notable alongshore variability only (i.e. RBB, TBR and eTBR).

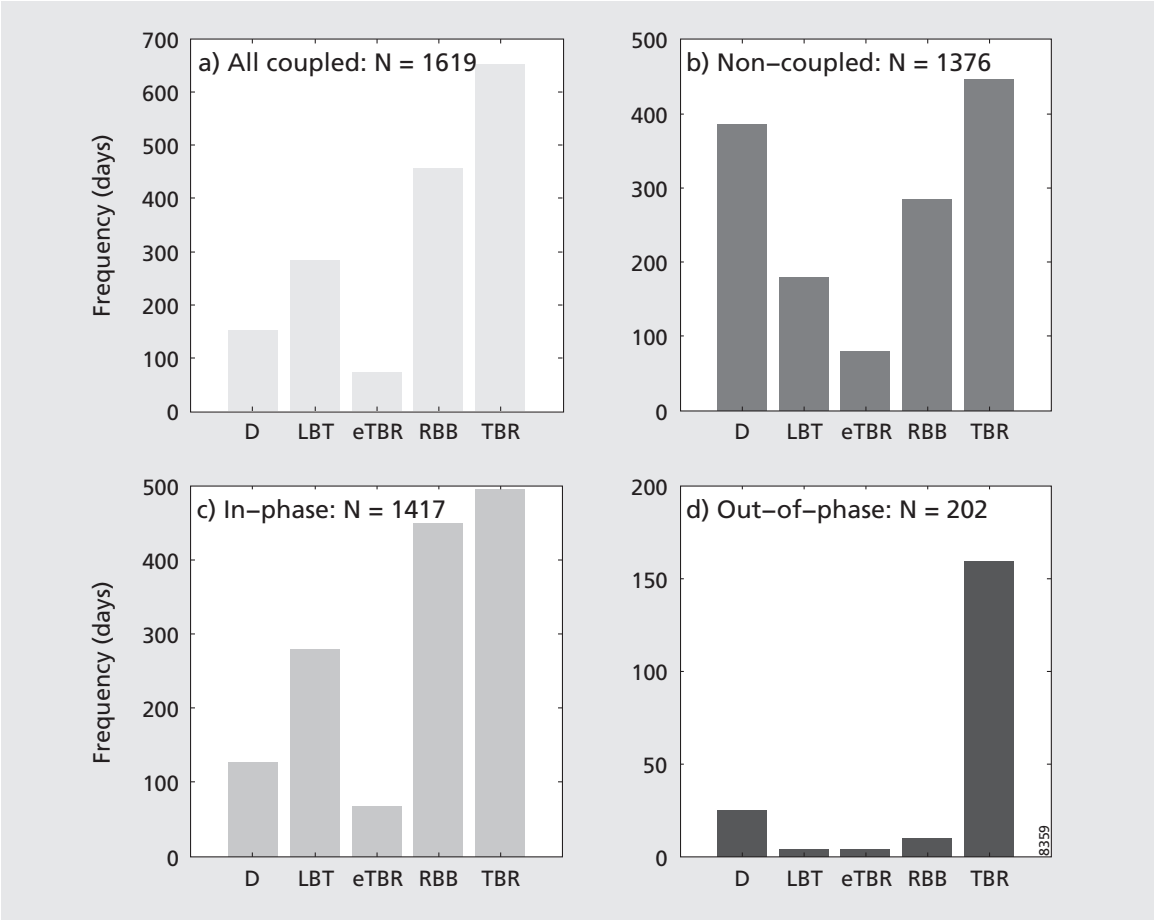

Figure 3.3 Occurrence of the outer sandbar state for (a) all coupled barlines, (b) non-coupled barlines, (c) in-phase coupled barlines and (d) out-of-phase coupled barlines. Here, N refers to the number of observations for each panel.

After assuming the outer D and LBT states to be uncoupled, the cross-correlation results exhibited coupling between the inner- and outer barline features for 40% of all observations (1184 out of the available 2995 days) at the 98% confidence level. In contrast to previous observations of common out-of-phase sandbar-shoreline coupling at single-barred beaches (e.g., Sonu, 1973), the bars here are mostly (85% of the coupled barlines) coupled in-phase. Less frequently (15% of the coupled barlines), the barlines coupled out-of-phase. In total, we observed 224 coupling events, consisting of 174 (78%) in-phase coupling events and 50 (22%) out-of-phase coupling events. The duration of coupling events ranged from 1 to 30 days, with in-phase (out-of-phase) coupling lasting 6-8 (3-6) days on average. Changing the confidence level to 95% or 99% did not alter the results notably.

A result of the cross-correlation technique is the lag at which the largest correlation between two signals is found. Figures 3.4a and b shows the histograms (with 30–m bins) of the lags corresponding to the in-phase and out-of-phase coupled barlines, respectively. We found a skewed lag distribution toward negative values for in-phase

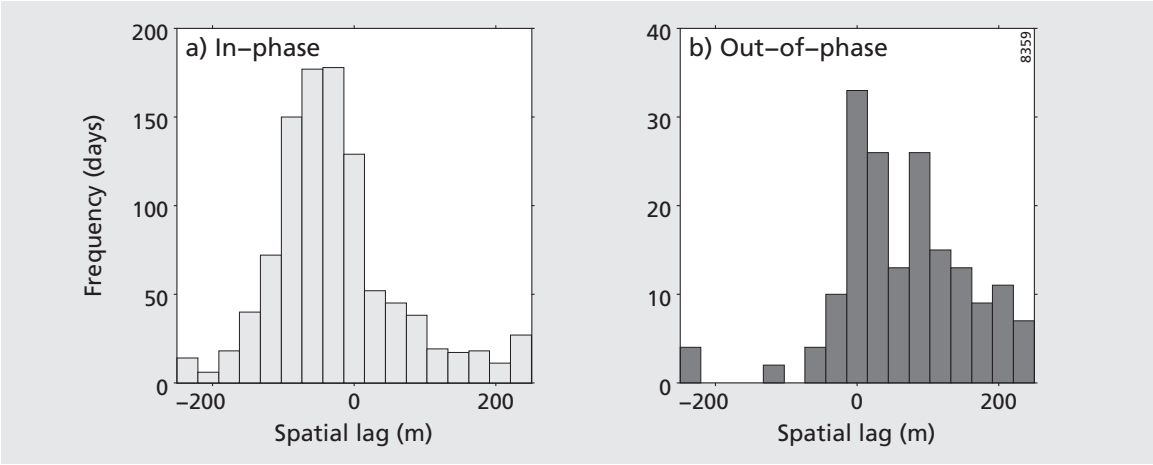

Figure 3.4 Distribution of the alongshore offset (lag) between the significantly correlated outer and inner barlines for (a) in-phase coupling and (b) out-of-phase coupling.

coupling with a modal lag of −30 m. This coincides with the inner barline being positioned to the north of the corresponding outer-bar shape (as depicted in Figure 3.5a). The lag distribution for out-of-phase coupling, on the other hand, was bimodal and was skewed toward positive values. The mode values of 0 m and 100 m correspond to no alongshore offset at all (see Figure 3.5c) and with the inner barline shape being positioned to the south of the corresponding outer barline shape (see Figure 3.5e), respectively.

Whereas the above results show that in-phase coupling with an alongshore offset of the coupled features predominated, the inclusion of the inner-bar state provides further details on the type of coupling. Table 3.1 provides the bar states for both the inner and outer bar during in-phase coupling. The inner bar predominantly appeared as a terraced (rip-less) feature (rLTT; 55%), both for the detached (RBB) and attached (TBR) outer-bar state, corresponding to the dominant outer bar states for the inner and outer bars at this site, shown in Chapter 2. An example of this coupling type for an outer RBB is given in Figure 3.5a, whereas the case for an outer TBR is provided in Ruessink et al. (2007a, their Figure 3f). Although less abundantly, the inner bar also contained rip channels (i.e. the inner TBR state; 8% of in-phase coupled barlines) that coupled to the crescentic outer bar (see Figure 3.5b). For out-of-phase coupling, the inner bar also predominantly appeared as an rLTT, in combination with an outer TBR (Table 3.2; 73%). For this combination of states, the coupled features of the alongshore variable outer bar and the inner terrace were either at the same alongshore position (Figure 3.5c), or displaced alongshore (Figure 3.5e). Note that out-of-phase coupling with inner rips (TBR) corresponding to the locations of the outer horns (RBB or TBR), barely occurred (4%).

Table 3.1 Combined frequency of occurrence of the inner and outer bar states for in-phase coupling ($N = 1011$, not all states shown).

Inner	*Outer* **eTBR**	**RBB**	**TBR**
TBR	1	33	50
rLTT	55	203	300
LTT	9	119	25
R	1	68	115

Table 3.2 Combined frequency of occurrence of the inner and outer bar states for out-of-phase coupling ($N = 173$, not all states shown).

Inner	*Outer* **eTBR**	**RBB**	**TBR**
TBR	1	0	6
rLTT	3	5	126
LTT	0	2	3
R	0	0	24

3.3.2 Observed coupling patterns

Based on the results above and a visual inspection of the 9.3 years of low-tide time-exposure images, we distinguish 5 main types of coupled sandbar morphology at our study site, depicted in Figure 3.5. The bars either coupled in-phase, with an outer-bar horn facing a shoreward perturbation of the inner barline, or out-of-phase, where the outer-bar horn coincided with a seaward bulge in the inner barline. Four of the five observed coupling types coincided with a downstate sequence of the outer bar, further explained in Sections 3.3.3 and 3.4. The morphology of the inner bar was found to be either terraced (with no trough or channels intersecting the bar) or characterised by the presence of rip channels. These properties are hereafter used to refer to the observed coupling types, as depicted in Figure 3.5: I or O (in-phase or out-of-phase), d or u (downstate or upstate) and t or r (terraced or with rips).

As shown in Section 3.3.1, sandbar coupling at our study site was mainly in-phase, with a terraced inner bar (rLTT; Table 3.1) showing landward perturbations displaced to the north of the outer-bar horns (Figure 3.4a). This corresponds to the Idt coupling type (Figure 3.5a), also observed by Ruessink et al. (2007a) at the same site. Although less common, rip channels in the inner bar mainly coupled in-phase with the outer bar bays (Tables 3.1 and 3.2), resulting in the Idr coupling type (Figure 3.5b). Similarly, for out-of-phase coupling during downstate transitions of the outer

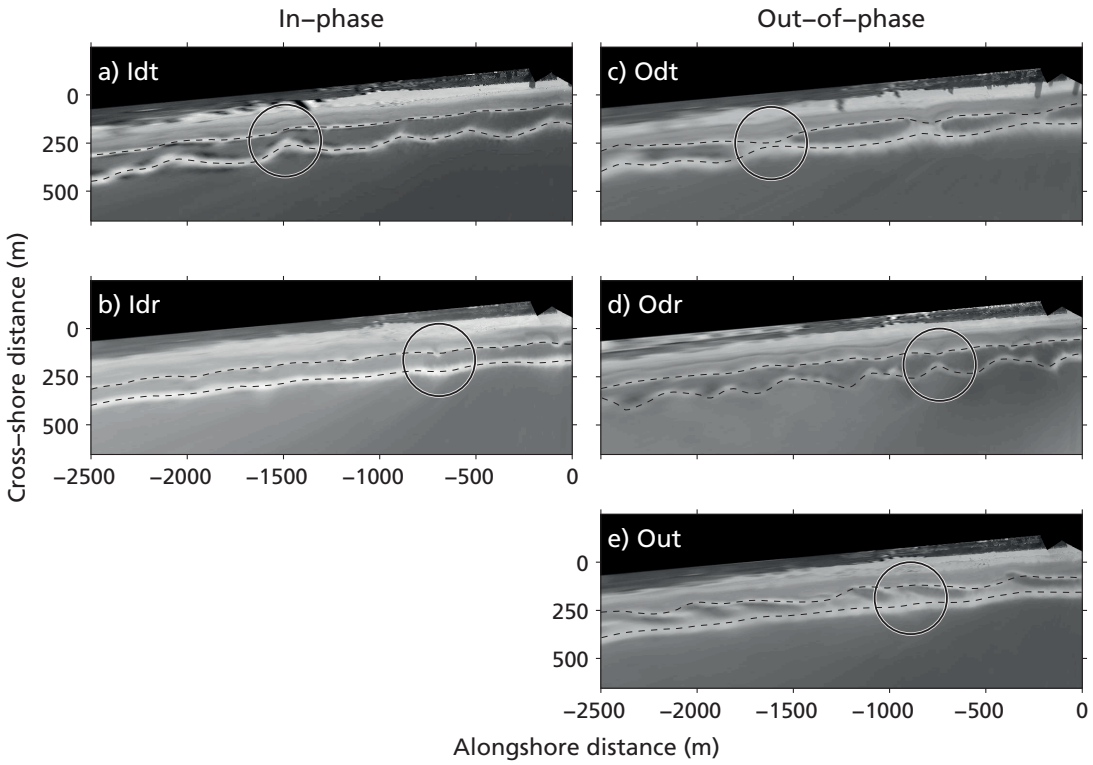

Figure 3.5 Examples of observed types of morphological coupling between the inner and outer barlines; low-tide time-exposure planview images of in-phase coupling with (a) an inner terrace and (b) inner rips, out-of-phase coupling with (c) an inner terrace and (d) inner rips in downstate direction, and (e) out-of-phase coupling with a clear alongshore offset between the inner and outer barline features in upstate direction. The dotted lines indicate the detected barlines, and the circles indicate a characteristic coupling feature for each coupling type. The images correspond to (a) 30 January 2006 0500GMT, (b) 18 January 2003 0400GMT, (c) 8 October 2002 0500GMT, (d) 22 May 2003 2300GMT and (e) 2 January 2003 0400GMT (day 2392, 1284, 1182, 1409 and 1268, respectively), also indicated in Figure 3.2.

bar, the inner-bar features either coupled to the locations of the outer-bar horns as seaward perturbations of the terraced inner bar (Odt; Figure 3.5c) or as rip channels (Odr; Figure 3.5d), although the latter was rarely observed (Table 3.2). Furthermore, a coupled pattern of the inner and outer barlines with a clear northward displacement of the outer-bar horns with respect to the seaward perturbations in the inner barline was observed (Figure 3.4b), following an upstate sequence of the outer bar. Here, the horns of the outer bar are obliquely oriented and attached to seaward perturbations of the terraced inner bar, indicating an out-of-phase coupling with a large alongshore offset (Out; Figure 3.5e).

3.3.3 Coupling patterns and wave conditions

Although each coupling event has its own unique set of boundary conditions, we observed a general trend in how a coupling type developed in response to certain wave conditions. Below, we first introduce a specific event for the Idt, Idr and Odt coupling types. We then aggregate these results into a conceptual model in Section 3.4.

Idt coupling type

As shown above, the main type of in-phase coupling Idt was associated with an alongshore offset of the inner barline features to the north. An alongshore offset between coupled barline features has previously been suggested to relate to the angle of wave incidence (Ruessink et al., 2007a; Quartel, 2009), consistent with the large (offshore) mean angle of wave incidence of 30° (from the southeast) at our study site. Figure 3.6 shows the evolution of the bar system during the development of an Idt type coupling in January 2006. Starting from straight inner and outer bars on 9 January (Figures 3.6a-d and k), the outer bar became crescentic within the following 10 days (Figure 3.6l), during a period with decreasing wave heights H_{rms} (below 1 m; Figure 3.6h) and shore-normally incident waves (Figure 3.6i). Concurrently, the inner bar progressed toward the LTT state (Figure 3.6l), corresponding to the decreased inner-bar variability (Figures 3.6c-d). During a more energetic event around 20 January with obliquely incident waves from the southeast (from the bottom left in the planviews), the outer-bar variability decreased, and the crescentic features migrated northward, in down-current direction (Figures 3.6a and m). The inner-bar variability subsequently increased and, as before this event, decreased as the angle of wave incidence became more shore-normal, corresponding to a decrease in both the wave power P and alongshore wave power P_y (Figure 3.6j). The initial increase coincided with the development of small rips as the inner bar progressed downstate, unrelated to the alongshore variability of the outer bar, corresponding to the observations of Ruessink et al. (2007a). Subsequently, from 24 January onward, both H_{rms} and the wave angle θ obtained more or less constant values of 0.8 m and 15 degrees (from the southeast), respectively. The terraced inner bar developed an undulating pattern (i.e. changing from LTT to rLTT) with landward perturbations located to the north of the outer-bar horns (Figure 3.6n). Thus, in this case the coupled inner-bar features developed in down-current direction, depicted by the negative lag (≈ -50 m) of maximum r_{xy} in Figure 3.6g.

Figures 3.6e and f show the corresponding time series of the estimated depth perturbations along the outer bar $z_p(y,t)$ and the variations therein $\Delta z_{\{5,95\}}(t)$, respectively. The horns (bays) would be expected to correspond to shallower (deeper) areas. Although some similarity between the variations in outer barline position and barline depth can be seen (e.g. the red shades (shallower areas) at $y_c = 500$ m and $y_c = 1000$ m in Figure 3.6e resemble the locations of the blue shades (landward perturbations) at $y = -1000$ m and $y = -1500$ m in Figure 3.6a, respectively), it is not so apparent for this case. During the last week of the shown period, from 24 January

to 1 February, the depth variation $\Delta z_{\{5,95\}}$ remained constant at about 0.5 m. The estimated bathymetry toward the end of this period (Figure 3.6o) shows the crescentic outer bar with small depth variations along its crest. Estimated uncertainties σ along the bar crest were less than 0.3 m.

Odt coupling type

In contrast to Idt, the main type of out-of-phase coupling Odt coincided with a zero-lag of the coupled barline features. Figure 3.7 shows the evolution of the bar system preceding the development of an Odt type coupling in March-April 2003. Starting from straight bars on 27 February, the inner-bar variability subsequently increased and decreased as rip channels developed (Figures 3.7c, d and k) and filled in, respectively, coinciding with the downstate progression of the inner bar during the first five days. Concurrently, the outer bar steadily started to develop alongshore variability (Figures 3.7a and b). Slight increases in both H_{rms} (Figure 3.7h) and θ around 6 and 12 March (Figure 3.7i), yielding an increase in $P_{(y)}$ (Figure 3.7i), coincided with temporary decreases in alongshore variability of the outer bar, and alongshore migration of both the inner- and outer-bar features. After 14 March, H_{rms} decreased to an average value of 0.7 m and, despite the large angles of wave incidence, the alongshore wave power decreased to about 2 kW/m. Apparently, the relatively weak alongshore current permitted the outer-bar features to remain at their alongshore positions and to become more pronounced, both in position (Figure 3.7a, b and l) as in depth (Figure 3.7e, f and o): after 18 March, $\Delta z_{\{5,95\}}$ increased up to 1 m and remained constant. Moreover, as shown by Ruessink et al. (2007a) (who also studied this specific period), the outer bar propagated onshore under these wave conditions, coinciding with the development of alongshore variability of the inner bar (Figures 3.7d and m) round about 25 March, with a slight alongshore offset of the coupled features (see Ruessink et al., 2007a). It was not until April 13, coinciding with a reduction of P_y to 1 kW/m, that the outer bar eventually welded to the terraced inner bar, resulting in Odt-type coupling (Figures 3.7g and n). The outer barline position, in this case, clearly corresponded to the depth variation along the barline (the landward perturbations in Figure 3.7a at $y = -1000$ m and $y = -1300$ m coincide with the shallow areas at $y_c = 900$ m and $y_c = 550$ m in Figure 3.7e,

---

Figure 3.6 (following page) Example of the development of the Idt coupling type, with time series of the outer barline (a) perturbations $X_{p,ob}(y,t)$, (b) standard deviation $\sigma_{x,ob}$, inner barline (c) perturbations $X_{p,ib}(y,t)$, (d) standard deviation $\sigma_{x,ib}$, outer-bar depth (e) perturbations along the barline $z_p(y,t)$, (f) variation $\Delta z_{\{5,95\}}$, (g) cross-correlogram of the inner and outer barlines, offshore (h) root-mean square wave height H_{rms}, (i) angle with respect to shore-normal θ and (j) the (alongshore component of the) wave power $P_{(y)}$, depicted by the dotted (solid) line. Panels k-n show low-tide time-exposure planviews, where the white box indicates the computational area used to estimate the bathymetry in (o), and the dotted lines indicate the detected barlines. Note that x and y (x_c and y_c) denote image (computational area) coordinates.

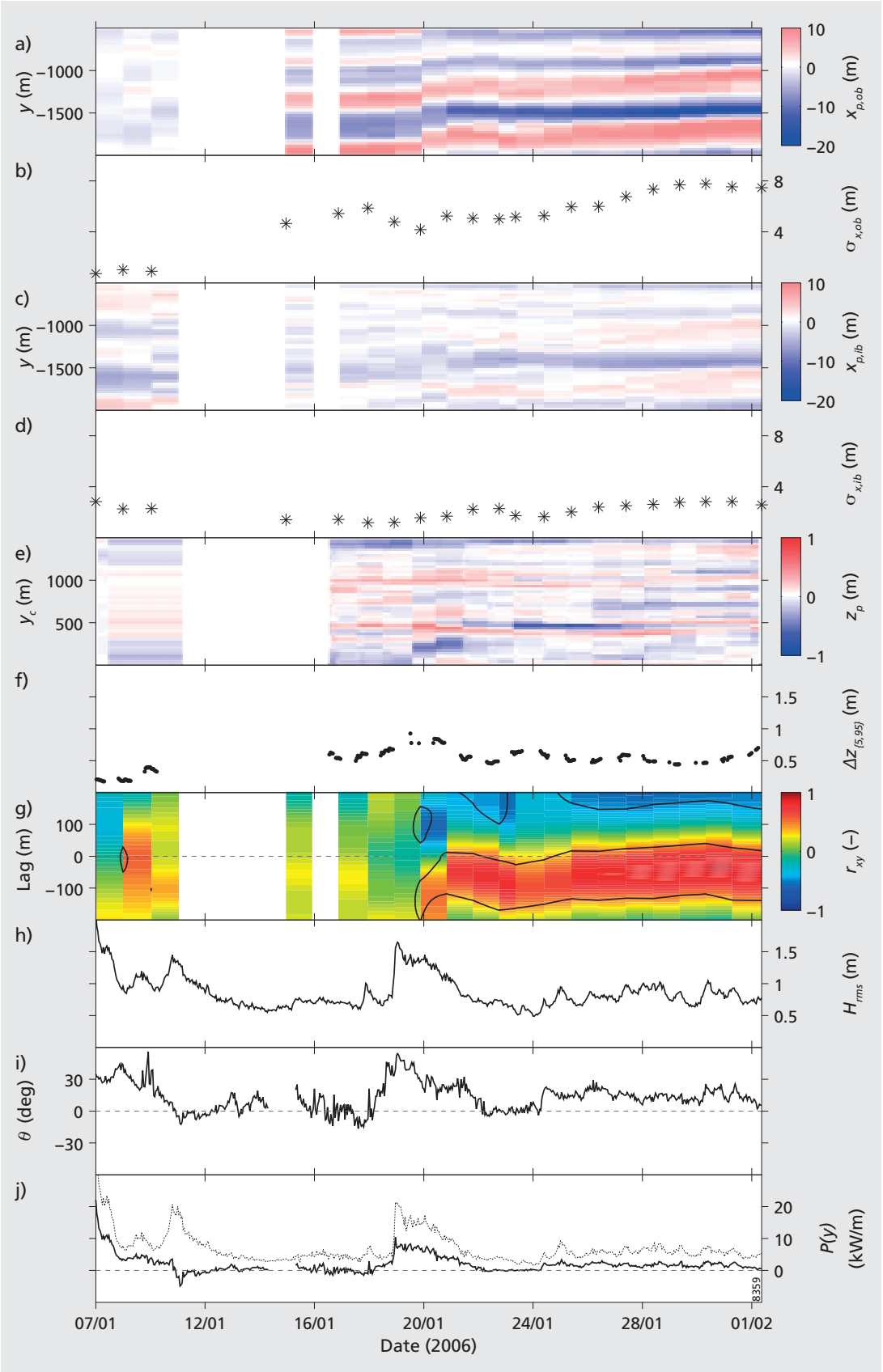
a)
b)
c)
d)
e)
f)
g)
h)
i)
j)
y (m)
−1000
−1500
10
0
−10
−20
$x_{p,ob}$ (m)
8
4
$\sigma_{x,ob}$ (m)
$x_{p,ib}$ (m)
$\sigma_{x,ib}$ (m)
y_c (m)
1000
500
1
0
−1
z_p (m)
1.5
1
0.5
$\Delta z_{[5,95]}$ (m)
Lag (m)
100
0
−100
r_{xy} (−)
H_{rms} (m)
θ (deg)
30
0
−30
20
10
0
P(y) (kW/m)
8359
07/01
12/01
16/01
20/01
24/01
28/01
01/02
Date (2006)

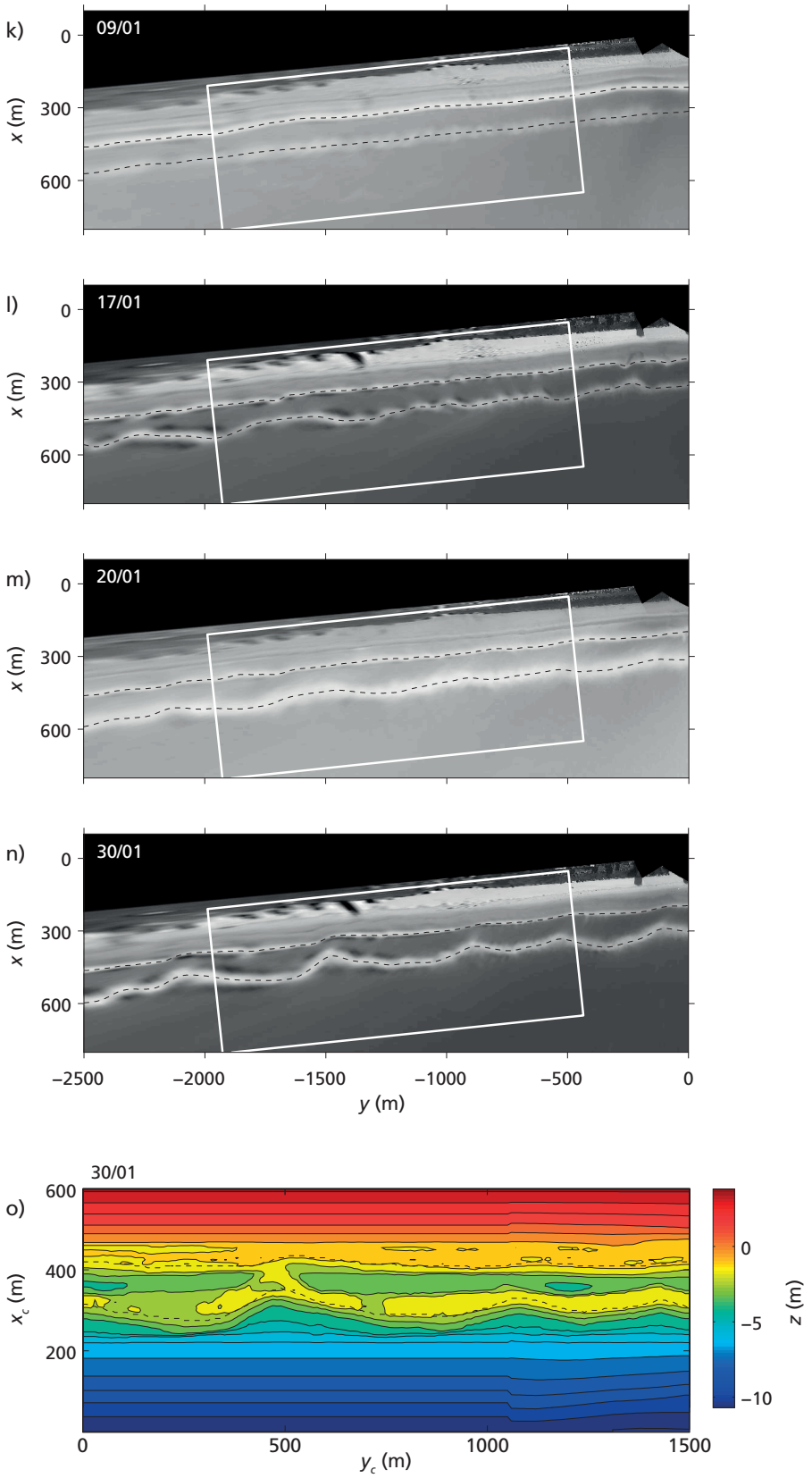

Figure 3.6 Development of Idt coupling type, see page 67 for caption.

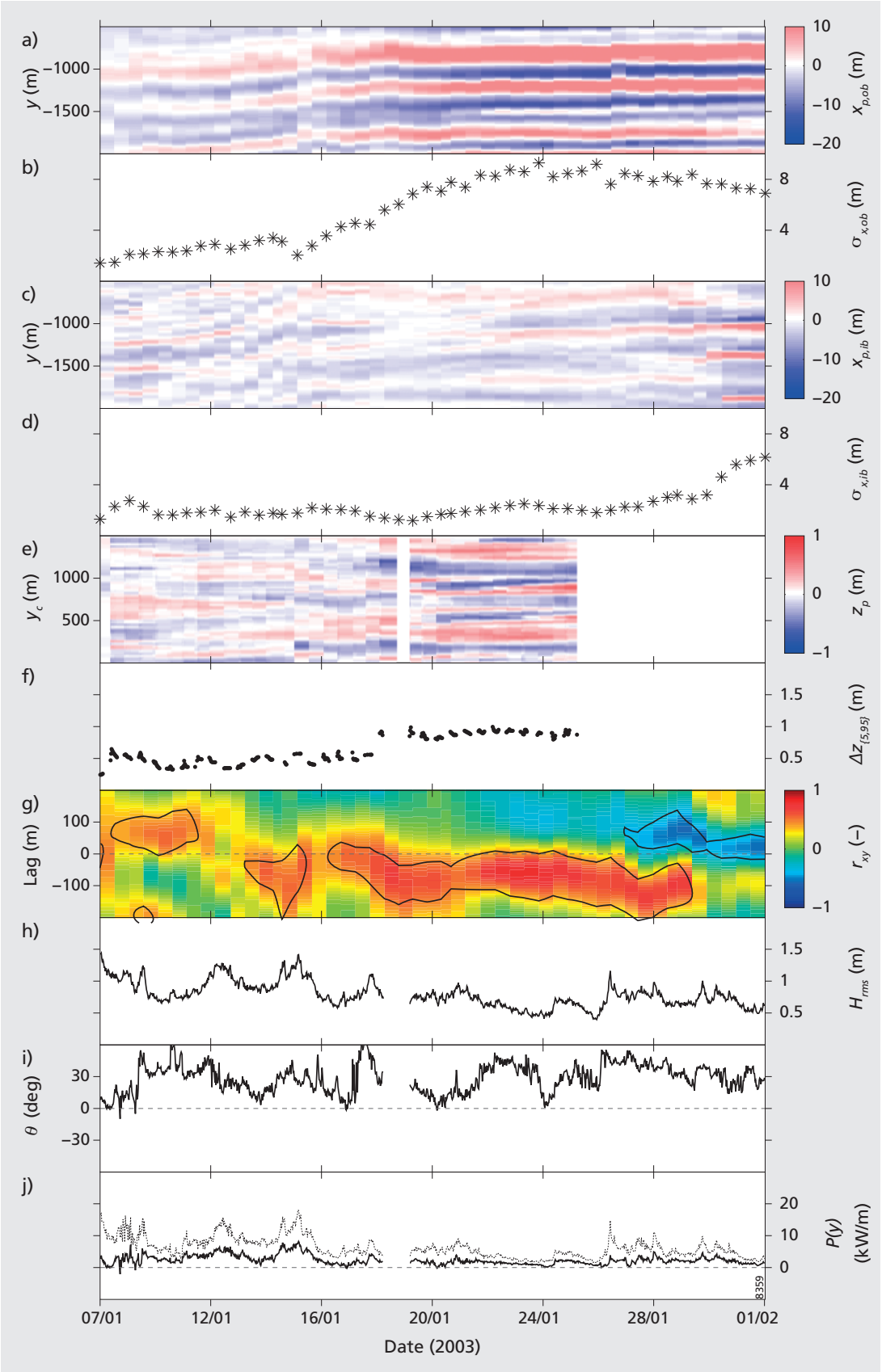
a)
y (m)
−1000
−1500
10
0
−10
−20
$x_{p,ob}$ (m)
b)
8
4
$\sigma_{x,ob}$ (m)
c)
y (m)
−1000
−1500
10
0
−10
−20
$x_{p,ib}$ (m)
d)
8
4
$\sigma_{x,ib}$ (m)
e)
y_c (m)
1000
500
1
0
−1
z_p (m)
f)
1.5
1
0.5
$\Delta z_{[5,95]}$ (m)
g)
Lag (m)
100
0
−100
1
0
−1
r_{xy} (−)
h)
1.5
1
0.5
H_{rms} (m)
i)
θ (deg)
30
0
−30
j)
20
10
0
P(y) (kW/m)
8359
07/01
12/01
16/01
20/01
24/01
28/01
01/02
Date (2003)

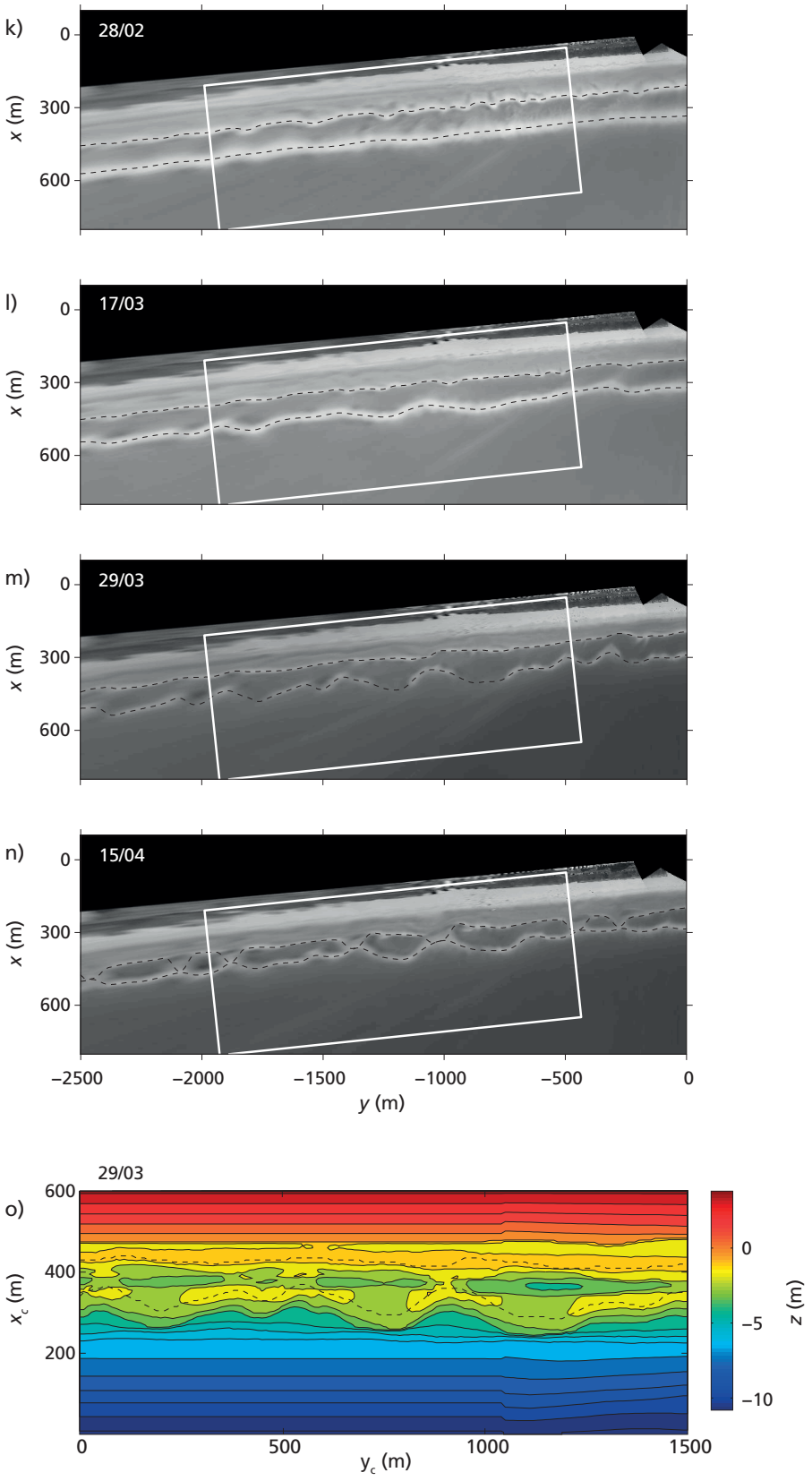

Figure 3.7 Development of Odt coupling type, see caption on page 67 for details.

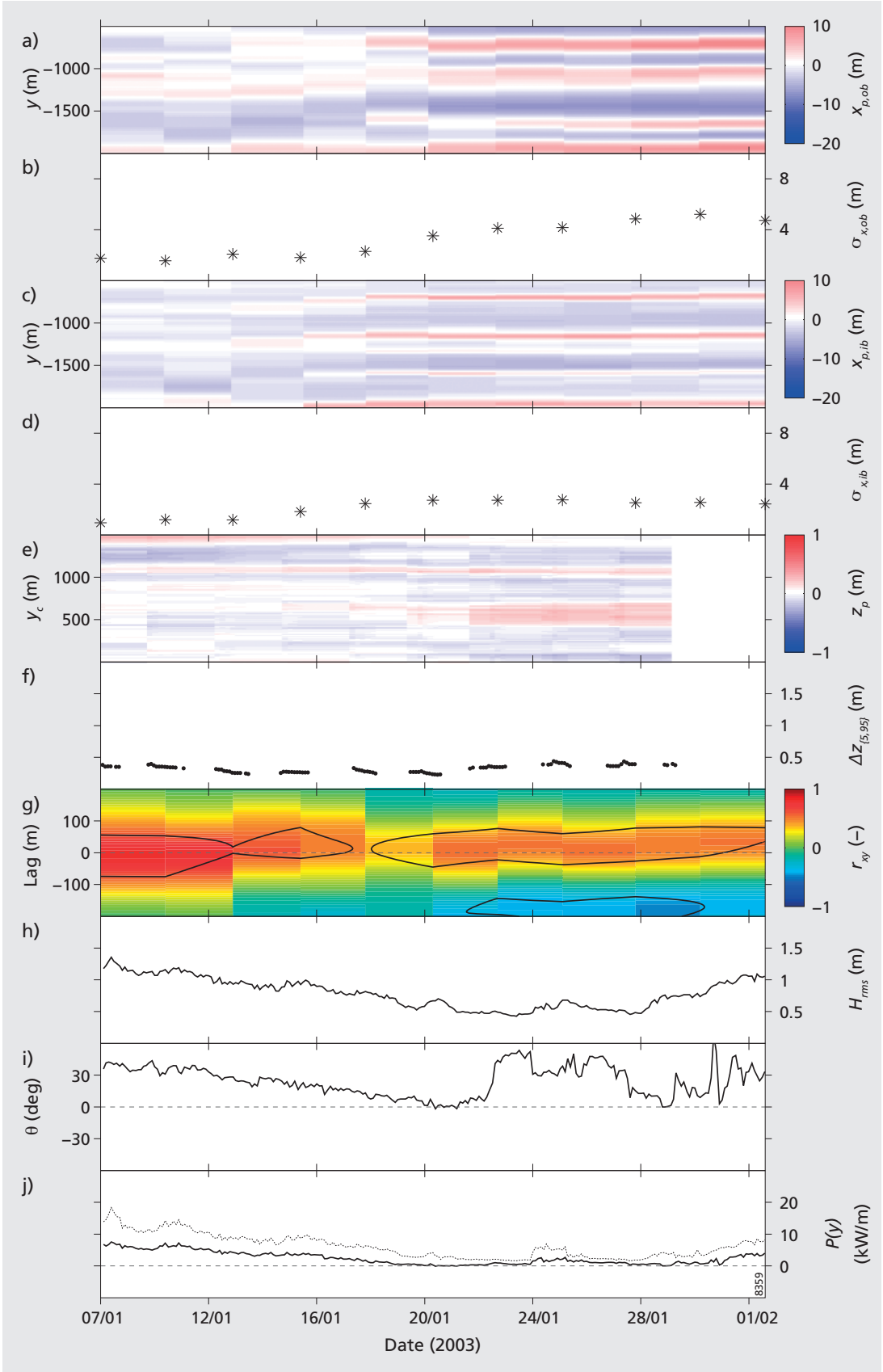
a)
y (m)
−1000
−1500
10
0
−10
−20
$x_{p,ob}$ (m)
b)
8
4
$\sigma_{x,ob}$ (m)
c)
y (m)
−1000
−1500
10
0
−10
−20
$x_{p,ib}$ (m)
d)
8
4
$\sigma_{x,ib}$ (m)
e)
y_c (m)
1000
500
1
0
−1
z_p (m)
f)
1.5
1
0.5
$\Delta z_{[5,95]}$ (m)
g)
Lag (m)
100
0
−100
1
0
−1
r_{xy} (–)
h)
1.5
1
0.5
H_{rms} (m)
i)
θ (deg)
30
0
−30
j)
20
10
0
P(y) (kW/m)
8359
07/01
12/01
16/01
20/01
24/01
28/01
01/02
Date (2003)

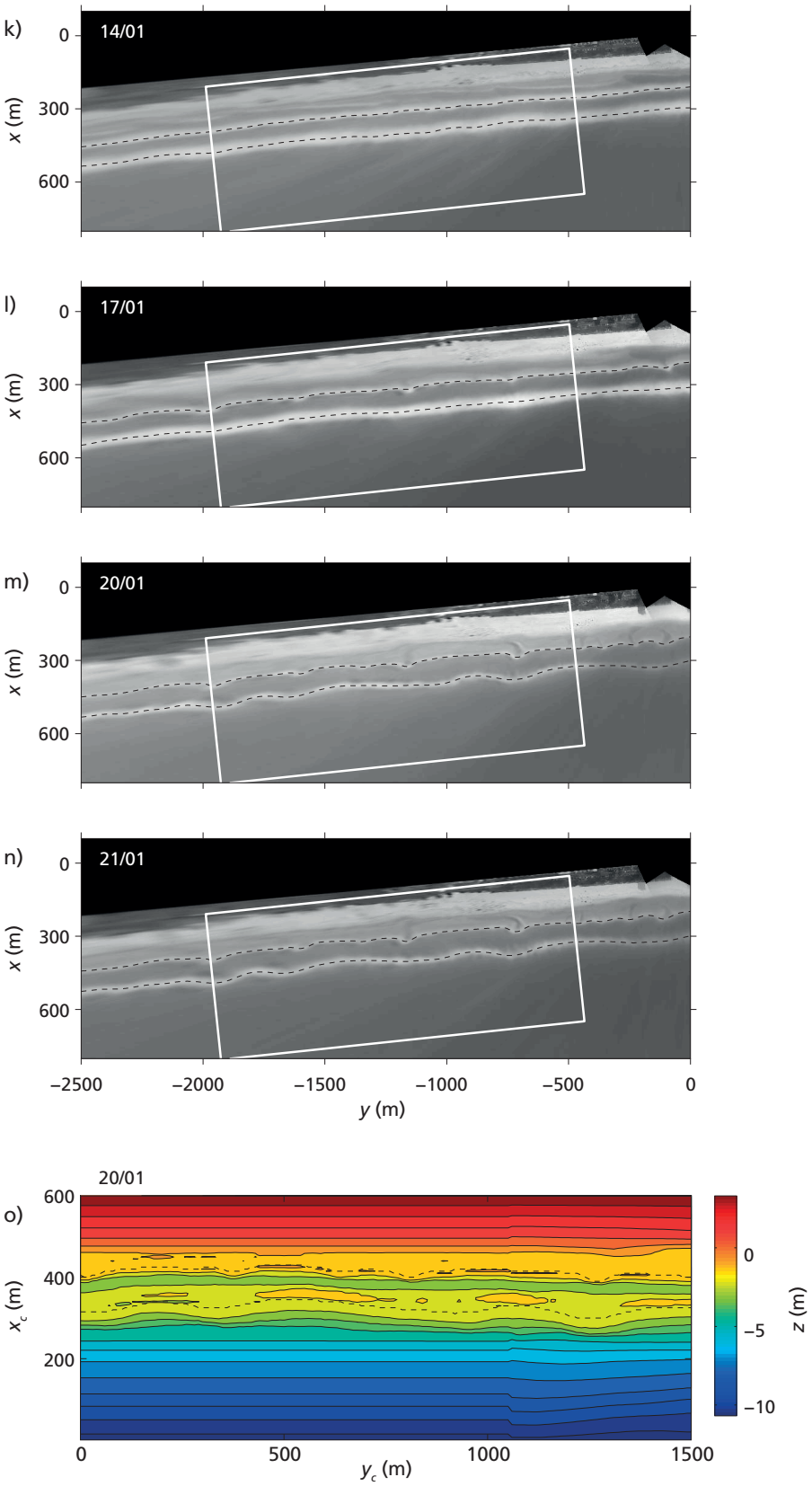

Figure 3.8 Development of Idr coupling type, see caption on page 67 for details.

respectively). Estimated uncertainties σ along the bar crest in Figure 3.7o were less than 0.4 m.

Idr coupling type
Figure 3.8 shows the evolution of the bar system during the development of an Idr type coupling in January 2003. Initially, on 14 January, both the inner and outer bars were alongshore uniform, with an alongshore continuous trough (Figures 3.8a-d and k). In the course of the subsequent 5 days, both H_{rms} and θ steadily decreased to approximately 0.5 m and 0 degrees, respectively (Figures 3.8h-i), during which both bars developed alongshore variability. The inner-bar trough started to fill in and rip channels started to develop (Figure 3.8l). Although the perturbations in the barlines only became clearly visible from 17 January onwards (Figure 3.8a-d and l), perturbations in the outer-bar crest depth were detected on 15 January at approximately y_c = 600 m, y_c = 1100 m and y_c = 1500 m, and remained until the end of the shown period (Figure 3.8e). Initially, the rip channels in the inner bar were obliquely oriented, but their orientation became shore-normal and they became positioned at the alongshore location of the outer-bar bays (Figures 3.8g and l-n) as the angle of wave incidence approached shore-normal and P_y decreased (Figure 3.8j). The depth variation along the outer-bar crest remained just below 0.5 m during the development of the Idr coupling type (Figure 3.8f and o), where estimated uncertainties along the bar crest σ were less than 0.3 m.

3.4 Conceptual model

As described in Section 3.1, it has been shown that for shore-normal wave incidence the depth variations of the outer bar determine alongshore variations in wave breaking and/or focussing (by refraction), which in turn, may lead to coupling of the inner bar. Castelle et al. (2010a) found that a larger fraction of wave breaking across a crescentic outer bar leads to out-of-phase coupled barlines, with the inner-bar rips facing the shallower outer-bar horns, coinciding with the Odr coupling type. They found in-phase coupling, on the other hand, to develop for outer bars with smaller alongshore depth variations and for smaller wave heights (see Castelle et al., 2010a, their Figure 5c). In this case, wave focussing by refraction over the outer-bar horns overwhelmed the effect of wave breaking and the inner-bar rip channels emerged at the alongshore locations of the outer-bar bays, the Idr coupling type. This corresponds with our findings that the Idr coupling type coincided with a relatively small depth variation along the outer barline of about 0.5 m (Figure 3.8), in combination with small wave heights and shore-normal wave incidence. Both the Odr and Idr coupling types result from the cell-circulation patterns invoked by a crescentic outer bar, causing the initially alongshore-uniform inner bar (and trough) to develop rip channels that are coupled to the outer-bar geometry, as it progresses downstate. The fact that both the Odr and the Idr coupling type were not frequently observed at our study site (see Section 3.3.1) may therefore relate to the dominant oblique wave incidence. More-

over, the inner bar predominantly appeared as a rhythmic low tide terrace, without rip channels. As shown in Chapter 2, inner-bar rip channels mainly formed when the outer bar was more upstate (LBT or D), during which less wave breaking over the deeper (Ruessink et al., 2009) outer bar allowed more wave energy to reach the inner bar (also see Figures 3.6-3.8). For obliquely incident waves circulation patterns may be inferior to the magnitude of the alongshore current (Sonu, 1972; MacMahan et al., 2010). Instead, the outer bar may drive a meandering alongshore current that follows the crescentic shape (depth isobars) of the outer bar, with a more landward (seaward) positioned alongshore current at the outer-bar horns (bays). Sonu (1972)'s Figure 1 suggests that such a meandering current, with increased velocities at the more landward oriented part of the alongshore current (MacMahan et al., 2010), may lead to an Idt coupling with an associated downdrift offset. The dominant northward shift of the inner-bar features for the Idt coupling type (Sections 3.3.1 and 3.3.3) illustrates the down-current offset corresponding to the dominant south-east (30°) angle of wave incidence. If sufficiently powerful, the alongshore current may drive the alongshore migration of the outer-bar features (Van Enckevort and Ruessink, 2003), or even lead to a more alongshore-uniform sandbar (in cross-shore position and depth; Section 2.4.1). A similar influence of the alongshore current is found for the Out coupling type, where the outer bar is displaced down-current (to the right in the planviews; Figure 3.5e). In this case, however, the correlated inner-bar features have an offset in up-current direction. As shown in Section 2.4.1, this state (with an outer eTBR) coincides with sufficiently energetic obliquely incident waves, causing the outer bar to migrate alongshore (in down-current direction) and to straighten. The inner-bar features migrate less, causing an up-current offset with respect to the outer-bar features. If both bars maintain their coupled features as they migrate alongshore differently, the outer eTBR may appear coupled in-phase with the inner rLTT (see the corresponding frequency of occurrence of 5% in Table 3.1). Moreover, the barline forms were mainly found to decouple as a result of these different migration rates (90% of all decoupling events), as opposed to morphological resets during heavy storms (10%). The mode lag of zero for out-of-phase coupled barlines, on the other hand, implies reduced longshore currents and/or the prevalence of more shore-normal wave incidence leading to this type of coupling. The corresponding evolution described above in Section 3.3.3, however, showed that wave heights must also remain low (Figure 3.7), and that an outer bar with large alongshore depth variations may persist through larger angles of wave incidence if the wave height is sufficiently small. Consequently, the foregoing suggests that longshore currents (driven by obliquely incident waves) prevent the outer-bar horns from completely connecting to the inner bar. This is supported by the dominance of the attached TBR state for out-of-phase coupling (Figure 3.3d).

Figure 3.9 summarises our observations of the different coupling types in a conceptual model. Coupling during downstate progression of the outer bar is either in-phase or out-of-phase, where the coupled inner-bar features either consist of rip channels or perturbations of the low-tide terrace. Obliquely incident, moderately energetic waves drive an alongshore current, which prevents the outer horns from welding to the inner bar. Instead, the alongshore current follows the crescentic shape of the outer bar and

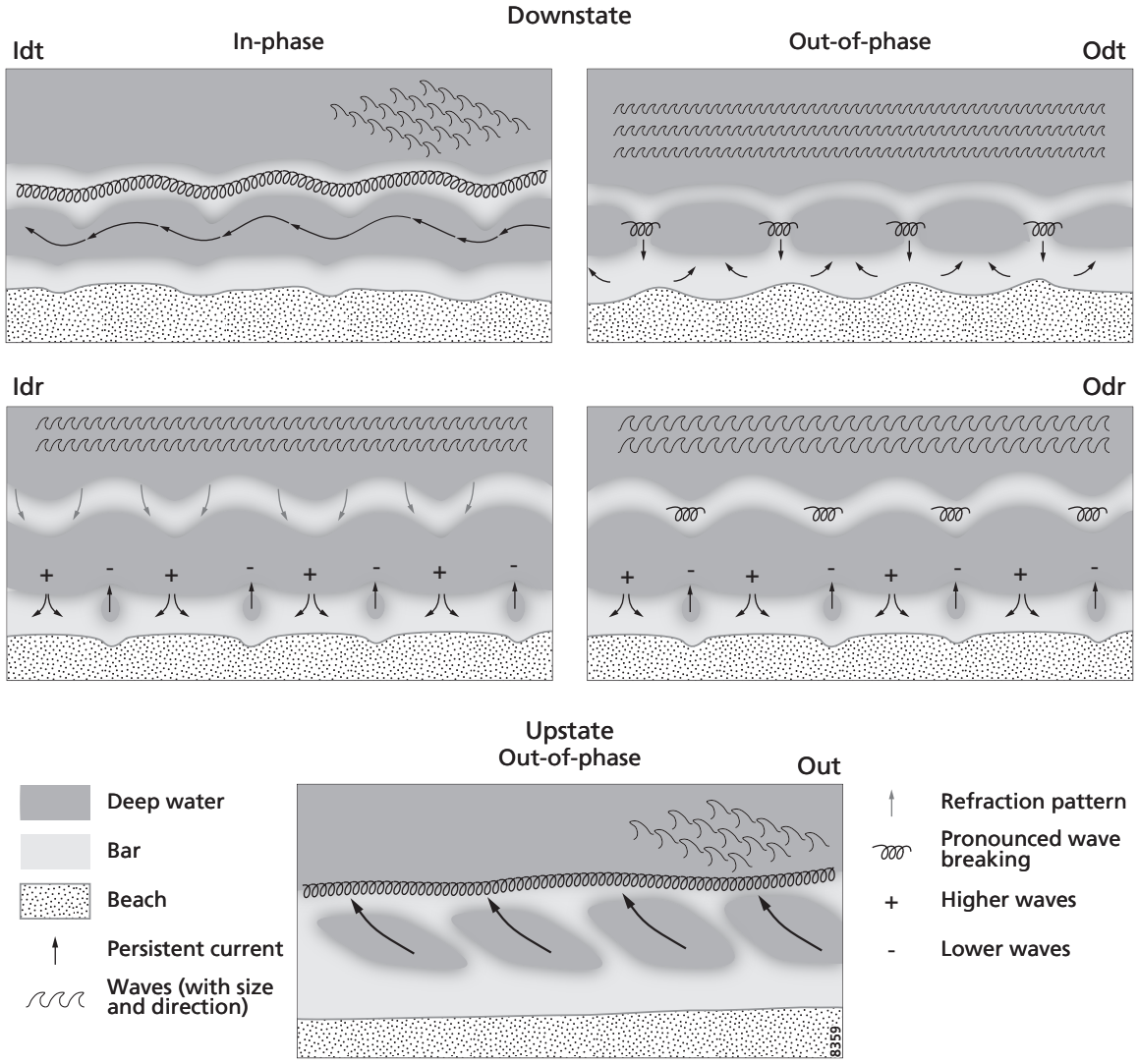

Figure 3.9 Conceptual model of the development of different coupling types.

veers landward at the horns, leading to downdrift-positioned landward perturbations in the inner terrace, the Idt coupling type. For this coupling type it is not the alongshore depth variation, but the alongshore planview shape of the outer bar which is important for altering the wave- and current field at the inner bar. Smaller wave heights (and smaller angles of wave incidence), however, drive a weaker alongshore current and allow the outer bar to propagate onshore and its horns to weld to the inner bar, leading to the Odt coupling type. Larger, shore-normally incident waves over such an outer bar with large depth variations drive a stronger circulation pattern over the inner bar, leading to the Odr coupling type. Larger, but obliquely incident waves over an attached outer crescentic bar, however, cause the outer bar to become

more alongshore uniform both in shape and depth. The outer-bar horns separate from the outer bar to become part of the inner bar (similar to Almar et al., 2010), resulting in an alongshore variable inner terrace, the upstate coupling type Out. If the straightening persists, both bars become alongshore uniform with an alongshore continuous trough. A sudden change to low-energetic, shore normal wave conditions toward the end of this straightening, however, leads to the Idr coupling type. Here, the small remaining depth variations along the outer bar cause wave focussing through refraction, driving a weak cell-circulation pattern over the inner bar that allows the bars to evolve alongshore variability at similar time scales.

Further work is necessary to test the generality of our findings. Similar to our observations and those of Ruessink et al. (2007a), for example, observations from Duck beach show the formation of an Idt coupling type (see Van Enckevort and Ruessink (2003), their Figure 1b), following a period of obliquely incident, moderately energetic waves (Van Enckevort et al., 2004). In general, we expect differences to arise due to e.g. tidal range, wave climate (i.e. swell or sea) and mean bottom slope. Besides intersite comparison, we believe numerical modelling is now essential to test our hypotheses on the role of the angle of wave incidence and alongshore currents on the coupling type. The XBeachWizard-derived bathymetries, combined with measured wave- and waterlevel forcing, provide a suitable step to do so for a natural sandbar system as opposed to the many previous modelling exercises with synthetic bathymetries and forcing (e.g., Smit et al., 2008; Castelle et al., 2010a,b; Castelle and Ruessink, 2011). Accordingly, in the next chapter, we force a non-linear model with realistic hydrodynamics and bathymetric data to test our hypotheses on the role of the angle of wave incidence on the coupling type.

3.5 Conclusions

From a 9.3-year data set of time-exposure images from a double sandbar system we distinguished 5 types of morphological coupling between the inner and outer sandbars. Using cross-correlation we found the coupling of the barlines to be a common phenomenon, at 40% of the observations, with the predominance of in-phase coupling (85%) over out-of-phase coupling (15%). The coupled inner-bar features mainly consist of perturbations in the low-tide terrace and form during the downstate progression of the outer bar; coupled rip channels are less common. The large mean angle of wave incidence at our study site seems to determine the predominance of in-phase coupling. We hypothesise that moderately energetic obliquely incident waves over a crescentic outer bar drive a meandering alongshore current along the inner bar, preventing the outer-bar horns from welding to the inner bar. Instead, landward perturbations are formed down-current of the outer-bar horns in the inner terrace, as indicated originally by Sonu (1972). More energetic, obliquely incident waves make both bars more alongshore uniform in position and depth, and eventually cause the bars to decouple. Motivated by existing modelling results (Castelle et al., 2010a,b), we further hypothesise that shore-normally incident waves over a crescentic outer bar

drive a cell-circulation pattern over the inner bar while increasing the depth-variation along the outer bar, ultimately resulting in out-of-phase coupling.

Acknowledgements

We thank Ap van Dongeren and Robert McCall, from Deltares, for providing the XBeachWizard code, and for their subsequent help in getting it running for our Gold Coast application. Financially supported by the Netherlands Organisation for Scientific Research (NWO), under contract 818.01.009. This paper is a contribution to the BarBec project (ANR N2010 JCJC 602 01), coordinated by Bruno Castelle at EPOC, University of Bordeaux 1.

4 Coupled sandbar patterns and obliquely incident waves

Based on: Price, T. D. and Castelle, B. and Ranasinghe, R. and Ruessink, B. G. (submitted), Coupled sandbar patterns and obliquely incident waves. Journal of Geophysical Research, Earth Surface.

4.1 Introduction

The nearshore bathymetry of many sandy beaches is characterised by the presence of one or more sandbars within a distance of several hundreds of metres from the shoreline. Each sandbar may develop a series of three-dimensional patterns (Wright and Short, 1984; Short and Aagaard, 1993), ranging from an alongshore-uniform ridge of sand to remarkably periodic alongshore undulations in both cross-shore position and depth, known as crescentic sandbars and rips. Crescentic sandbars can be seen as a sequence of shallow horns and deep bays, alternating seaward and landward of a line parallel to the coast, with typical length scales ranging from 100 to 1000 m (Van Enckevort et al., 2004). These horns and bays are formed spontaneously because of the positive feedback between horizontal cell circulation patterns (including rip currents), sediment transport, and the morphology itself (i.e. self-organisation mechanisms; Hom-ma and Sonu, 1962; Hino, 1975; Sonu, 1972; Falqués et al., 2000). In a double sandbar system, the inner bar morphology generally also develops through these self-organisation mechanisms. However, under certain conditions, the alongshore spacing of seaward and landward perturbations in the inner sandbar may be coupled to the horn spacing in the outer sandbar (as shown in Chapter 3 and by, e.g., Van Enckevort and Wijnberg, 1999; Ruessink et al., 2007a; Castelle et al., 2007a; Quartel, 2009). In this case, the crescentic outer-bar morphology acts as a forcing template for the inshore flow patterns through wave breaking and wave focussing across the outer bar (Garnier et al., 2008a; Castelle et al., 2010a,b). The morphological evolution of the inner bar, therefore, is driven by a mixture of self-organisation and outer-inner bar coupling mechanisms (Castelle et al., 2010a,b). Although morphological coupling between two sandbars suggests a reciprocal influence, observations (Ruessink et al., 2007a) and modelling results (Castelle et al., 2010a,b; Thiébot et al., 2012) indicated that the inner-bar morphology does not affect the outer-bar morphodynamics.

Coupled sandbar patterns can contain a variety of appearances, or, morphological states (e.g., Bowman and Goldsmith, 1983; Castelle et al., 2007a; Ruessink et al., 2007a). In Chapter 3, we distinguished 5 coupling types, based on observed breaker lines over a double-sandbar system (i.e. barlines) from over 9 years of time-exposure images from the Gold Coast, Australia. Four of the five observed coupling types coincided with a downstate sequence of the outer bar, a sequence during which the outer

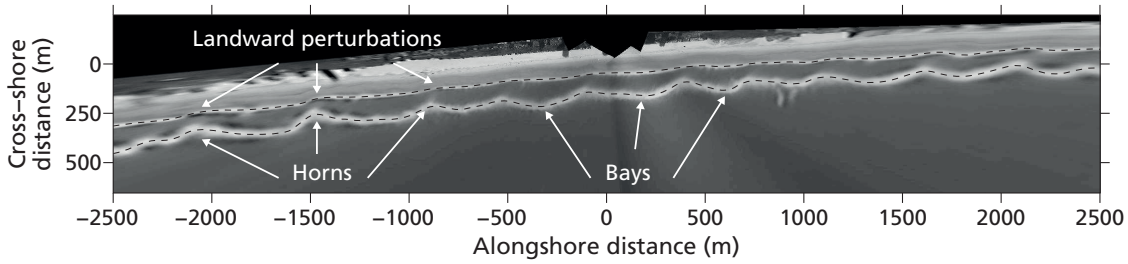

Figure 4.1 Example of a time-exposure image from the Gold Coast, Australia, showing the Idt coupling type, with a crescentic outer bar and an inner bar with landward perturbations coupled to the alongshore positions of the outer-bar horns. The dotted lines indicate the video-derived inner and outer barlines.

bar becomes increasingly alongshore non-uniform and propagates onshore (Wright and Short, 1984). The bars either coupled in-phase, with an outer-bar horn facing a shoreward perturbation of the inner barline, or out-of-phase, where the outer-bar horn coincided with a seaward bulge in the inner barline. The morphology of the coupled inner bar was either terraced, with no trough or channels intersecting the bar, or characterised by the presence of rip channels, where landward or seaward perturbations of the terraced inner bar and rip channels constituted the coupled inner-bar features. The inner-bar morphology may also remain coupled to the outer-bar morphology during upstate transitions (straightening) of the outer bar; the alongshore non-uniformity of the inner bar may actually increase during these upstate transitions as outer-bar horns detach, migrate onshore, and merge with the inner bar (Wijnberg and Holman, 2007; Almar et al., 2010). In Chapter 3, we used abbreviations for the aforementioned properties to name the 5 different coupling types according to whether the bars were coupled in- or out-of-phase (I or O), the outer bar proceeded downstate or upstate (d or u), and whether the inner-bar morphology was terraced or with rips (t or r). Using cross-correlation on the inner and outer barlines, we found the most frequent coupling type at our study site to be the Idt type, an outer crescentic bar with landward perturbations of the inner terrace coupled to the alongshore positions of the outer-bar horns (Figure 4.1).

Although video observations provide a high-frequency long-term data set of (coupled) sandbar morphology, they do not provide direct information on the morphodynamic processes leading to changes in sandbar morphology. Instead, numerical models are often used to shed light on the observed sandbar morphodynamics. So far, numerical studies of sandbar morphology have largely focussed on single-barred beaches (e.g., Ranasinghe et al., 2004; Reniers et al., 2004; Garnier et al., 2006; Tiessen et al., 2011). The few existing numerical studies of double sandbar systems have mainly focussed on the initial development and subsequent evolution of crescentic patterns, either using linear stability analysis (e.g., Klein and Schuttelaars, 2006; Garnier et al., 2008a; Coco and Calvete, 2009; Brivois et al., 2012), nonlinear depth-averaged models (Klein and Schuttelaars, 2006; Smit et al., 2008, 2012; Thiébot et al., 2012), or quasi-three-dimensional models (Drønen and Deigaard, 2007). Al-

though some of these studies analysed the effect of a varying cross-shore profile, the initial bathymetries were always alongshore-uniform, albeit with initial depth perturbations of $O(10^{-2})$ m to evoke bed pattern development. Castelle et al. (2010a,b), on the other hand, forced a nonlinear depth-averaged morphodynamic model with an initially crescentic outer bar with varying geometric parameters. They found that coupled inner bar features arise from horizontal circulation patterns driven by alongshore variations in wave refraction and wave breaking across the crescentic outer bar. Depending on both the outer bar geometry and the wave conditions, the barlines coupled either in-phase or out-of-phase. Whereas the simulations of Castelle et al. (2010a,b) were performed for shore-normal wave incidence only, Thiébot et al. (2012) performed numerical simulations for a large range of wave angles over initially alongshore-uniform sandbars. For slightly obliquely incident waves (10° and 15° with respect to shore normal at 8 m waterdepth), they found that initially the inner bar did not develop any alongshore variability due to the large alongshore current. However, when the outer bar started to develop alongshore variability, the alongshore current and the incoming wave field at the inner bar became perturbed, leading to the development of inner-bar features with an alongshore spacing similar to that of the outer-bar horns. This corresponds to the observations of Ruessink et al. (2007a), where inner-bar patterns developed in response to the increasingly three-dimensional, onshore migrating outer bar. None of these simulations, however, resulted in the Idt coupling type.

In Chapter 3, we hypothesised that the Idt coupling type related to the dominant oblique wave incidence. For a given crescentic outer bar, we suggested that the type of bar coupling is not solely a function of the amount and alongshore variation of wave breaking over the outer bar (as concluded by Castelle et al. (2010a)), but that the angle of wave incidence plays an important role. In the case of shore-normally incident waves, the outer bar drives a cell-circulation system over the inner bar, resulting in the development of coupled rip channels in the inner bar, either in-phase or out-of-phase. Obliquely incident waves over a crescentic outer bar, on the other hand, drive a meandering alongshore current at the inner bar, similar to the field observations of, e.g., Sonu (1972) and MacMahan et al. (2010). We hypothesised that the landward perturbations of the terraced inner bar for the Idt coupling type (Figure 4.1) resulted from this meandering alongshore current, with increased velocities at the more landward oriented parts of the alongshore current at the locations of the outer-bar horns. Although these observations indicated an important role of the angle of wave incidence for the flow pattern and the corresponding coupling type, we were unable to quantify our hypothesis from the video images alone.

In this chapter, we aim to analyse how the angle of wave incidence affects the coupling processes at the inner bar. As the processes and concepts underlying the coupling types that form under shore normal wave incidence were studied by Castelle et al. (2010a), we here focus on oblique wave incidence and, hence, the Idt coupling type. We use a nonlinear morphodynamic model to analyse the development of the Idt coupling type, and base our modelling exercise on a representative 4-day period of observations during which the Idt coupling type developed. Subsequently,

we demonstrate that the angle of wave incidence is crucial to the flow pattern and emerging coupling type at the inner bar. In contrast to existing modelling efforts of double-barred systems, which use synthetic or highly-idealised bathymetries, we force our model with realistic bathymetrical data derived from the video observations. In this way, we use the sandbar geometries (e.g., cross-shore distance, wavelength of the crescentic pattern, alongshore depth variation) and wave conditions for which our model should reproduce an Idt coupling type. Using this approach, we aim to bridge the gap between a purely synthetic modelling approach, and a direct comparison of modelling results with field measurements from a natural double sandbar system.

4.2 Methods

4.2.1 Non-linear morphodynamic model

We used a non-linear depth-averaged model (detailed in Castelle et al., 2012; Castelle and Coco, 2012) that couples a spectral wave model, a time- and depth-averaged flow model, an energetics-type sediment transport model, and the bed level continuity equation to compute bed level changes. The model has been successfully applied to simulate the formation, the nonlinear evolution and the finite amplitude dynamics of rip channels and crescentic sandbars (e.g., Castelle et al., 2010a, 2012). Furthermore, the model allows for shoreline evolution (and, thus, the development of erosive megacusps at the base of rip channels), and tidal water level fluctuations, which represents a major difference with other nonlinear morphodynamic models applied to 3D surfzone sandbar behaviour. The wave field and resulting radiation stress components are computed from the spectral wave model SWAN (Booij et al., 1999), which solves the spectral wave action balance, here with the parameter settings detailed in Castelle et al. (2012).

The flow model is based on the phase-averaged nonlinear shallow water equations (Phillips, 1977), comprising the time-averaged and depth-integrated momentum conservation and water mass conservation equations. Using the Einstein summation convention, where subscript i refers to the two horizontal coordinates (with x and y the alongshore and cross-shore axis, respectively), these read:

$$\frac{\partial Q_i}{\partial t} + \frac{\partial}{\partial x_j}\left(\frac{Q_i Q_j}{h}\right) + gh\frac{\partial \eta}{\partial x_i} + \frac{1}{\rho}\frac{\partial S_{ij}}{\partial x_j} - \frac{1}{\rho}\frac{\partial T_{ij}}{\partial x_j} + \frac{\tau_i^b}{\rho} = 0, \tag{4.1}$$

$$\frac{\partial \eta}{\partial t} + \frac{\partial Q_j}{\partial x_j} = 0. \tag{4.2}$$

where $Q_i = U_i h$ is the water volume flux per unit width in the i-direction, with U_i the component of the flow velocity $\vec{U}$; t is time; h is the mean water depth; g is the gravitational acceleration; η is the mean free surface elevation; ρ the water density; S_{ij} are the components of the radiation stress tensor; T_{ij} are the components of the lateral shear stresses, which are the horizontal momentum exchanges due to the combined action of turbulence and the mean current using the formulation proposed by Battjes (1975); τ_i^b are the components of the wave-averaged bed shear stresses.

The combined bed load and suspended load sediment transport $\vec{Q}_s$ are computed using the formulations of Bailard (1981). Both the bed load and suspended load parts contain an efficiency factor, ε_b and ε_s, respectively. We used the default values for the efficiency of either transport mechanisms: $\varepsilon_b = 0.1$ and $\varepsilon_s = 0.02$, respectively. Herein, we use the same approach for the sediment transport as in Castelle et al. (2010a,b), which differs from the approach in e.g. Castelle and Ruessink (2011), where the sediment transport was computed with respect to a pre-determined equilibrium bed level (i.e. basic state).

The new seabed level Z_f was computed using the sediment mass conservation equation:

$$\frac{\partial Z_f}{\partial t} + \frac{1}{1-p}\frac{\partial Q_{s,j}}{\partial x_j} = 0, \tag{4.3}$$

where $p = 0.4$ is the sediment porosity and $Q_{s,j}$ are the components of the sediment transport flux $\vec{Q}_s$. In the present work, the morphological timestep for the bed update scheme, which is different from the hydrodynamic time step (1 s), was 30 minutes for all the simulations presented herein.

4.2.2 Model setup

A bathymetry containing a double sandbar system can be described using a number of geometrical parameters, described below and illustrated in Figure 4.2. Firstly, the mean cross-shore profile, excluding sandbars, exhibits a concavity commonly described by the profile shape function d of Dean (1991):

$$d = Ay^{2/3}, \tag{4.4}$$

in which d is the water depth (for a given water level h) at a cross-shore distance y and A is a sediment-dependent scale parameter. Sandbars constitute perturbations on top of this alongshore-uniform profile, with their crests at a certain cross-shore position y and depth D. In Figure 4.2, the subscripts $_i$ and $_o$ denote properties of the inner and outer bar, respectively. The outer sandbar in Figure 4.2a consists of a bar that is separated from the inner bar by a trough. The inner bar, on the other hand, exhibits a terrace, with width w_i, where the depth is more or less constant. The alongshore variations of crescentic sandbars can be seen as a regular variation of depth and cross-shore position, in this case for the outer bar (Figure 4.2b). Accordingly, their shape can be described by a horizontal amplitude A_y of the cross-shore position around the mean cross-shore bar position y_o, an alongshore wavelength L_x, and a vertical amplitude A_z of the depth around the mean bar depth D_o. This amplitude corresponds to the depth differences between the more onshore-positioned horns and more offshore-positioned bays, with depths D_h and D_b, respectively (Figure 4.2a).

We directly derived the sandbar geometries from field data to create an idealised initial bathymetry using the geometrical parameters described above. In our study, both the bathymetry and the hydrodynamic forcing were derived from observations from the double-barred sandy ($D_{50} = 250$ μm) beach at Surfers Paradise (Queensland, Australia; Turner et al. (2004)), where morphological coupling is frequently

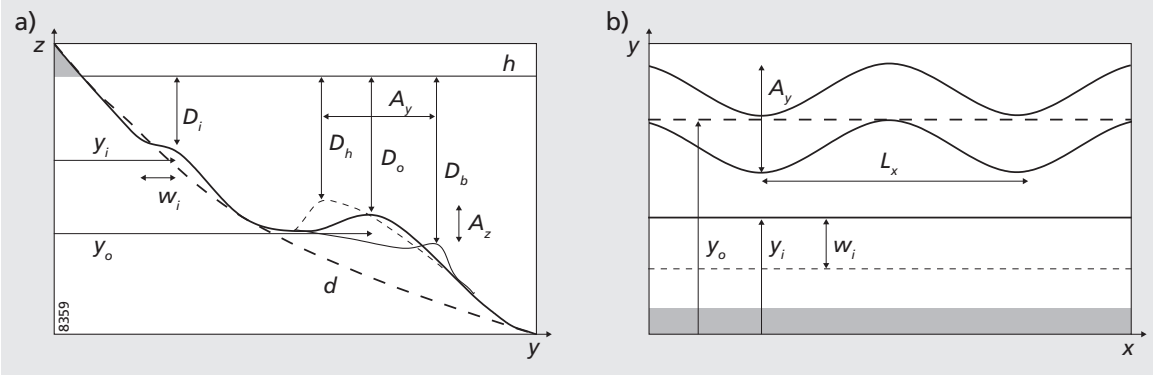

Figure 4.2 Schematic of (a) a cross-shore profile and (b) a plan view, illustrating the bathymetrical parameters of a crescentic double sandbar system. See text for further explanation.

Table 4.1 Bathymetrical parameters used for all simulations (see also Figure 4.2).

Parameter	*Description*	*Value*
d	Mean cross-shore profile with respect to mean sea level h (MSL)	$d = 5 - 0.245y^{2/3}$
y_i	Cross-shore position inner bar	140 m
y_o	Cross-shore position outer bar	240 m
D_i	Mean inner bar depth (MSL)	-0.5 m
D_o	Mean outer bar depth (MSL)	-2.1 m
w_i	Terrace width inner bar	40 m
L_x	Wavelength alongshore variation outer bar	500 m
A_y	Horizontal amplitude of cross-shore position outer bar	40 m
A_z	Vertical amplitude between horns and bays	0.5 m

encountered (Chapter 3). We extracted the boundary conditions for the simulations used herein from a representative 4-day period during which the development of an Idt coupling type was observed in time-exposure video images (Section 3.3.3): from 25 to 28 January 2006 (see Figure 4.3a-d). During this period, the initially alongshore-uniform inner bar coupled to the crescentic outer bar, while the wave conditions remained fairly constant (Figure 4.3e-h).

Firstly, we obtained the mean beach profile d by fitting Eq. 4.4 to the alongshore-averaged cross-shore profile from a bathymetrical survey from June 2002, giving $d = 5 - 0.245y^{2/3}$ (Table 4.1; Figure 4.4a). From the time-exposure images we directly derived the mean cross-shore positions of the inner bar y_i and the outer bar y_o, which were 100 m apart, the terrace width of the inner bar $w_i = 40$ m (Figure 4.4a), and the wavelength $L_x = 500$ m and cross-shore amplitude $A_y = 40$ m of the outer crescentic bar (Figure 4.4b). Because of a lack of suitable bathymetric

Table 4.2 Wave conditions used for all simulations (see also Figure 4.3).

Parameter	*Description*	*Value*
H_s	Significant wave height	1.1 m
θ	Angle of wave incidence (reference case)	0° to 20° (14°)
T_p	Peak wave period	9 s
ζ	Tidal water level	0 m

surveys, we applied the assimilation model XBeachWizard (Van Dongeren et al., 2008) to transform the breaking-induced intensity in the video image into estimates of the depth (see Appendix A for details). This yielded an alongshore depth variation $A_z = 0.5$ m between the depth of the horns D_h and the depth of the bays D_b. Based on the assimilation results and available measured bathymetries, the mean depth of the outer bar D_o and inner bar D_i were set at -2.1 and -0.5 m with respect to mean sea level (MSL), respectively. The effect of different outer and inner bar depths D_o and D_i on the model results are discussed in Section 4.4. All simulations were performed with the same initial double sandbar bathymetry (Figure 4.4c) with a (3D) crescentic outer bar and an alongshore uniform terraced inner bar, on a computational grid of 3020 × 780 m (alongshore × cross-shore), 20 × 20 m grid cells, and periodic lateral boundary conditions. The water depth at the seaward extent of the model, at $y = 780$ m, was 15 m.

For the reference simulation we used constant wave conditions, corresponding with the mean values of the 4-day observation period (Table 4.2; Figure 4.3e-h): a mean significant wave height H_s of 1.1 m, a mean angle of wave incidence θ of 14° (herein, θ is always with respect to shore-normal and in 15-m depth, obtained by refracting the measured data using Snell's law), a mean peak wave period T_p of 9 s, and a constant tidal water level ζ of 0 m. Subsequently, we varied θ from 0° to 20° with steps of 1°, while keeping all other boundary conditions constant. The wave conditions during the 4-day period (Figures 4.3e-h) were sufficiently constant (standard deviations: $\theta = 6.9°$, $H_s = 0.2$ m, $T_p = 1.2$ s), to support the simplified approach of using the averaged, time-invariant wave forcing for the simulations. As θ varied only slightly, and did not change sign (Figure 4.3f), we do not expect that usage of the mean value in this case will lead to significantly different dynamics as suggested by Castelle and Ruessink (2011) for larger θ variations. We neglected the observed tidal water level variation ζ and applied a constant water level throughout all simulations. Including tide, however, did not significantly affect the model results, further discussed in Section 4.4. We applied a simulation time of 4 days for all computations, corresponding to 192 morphological model timesteps.

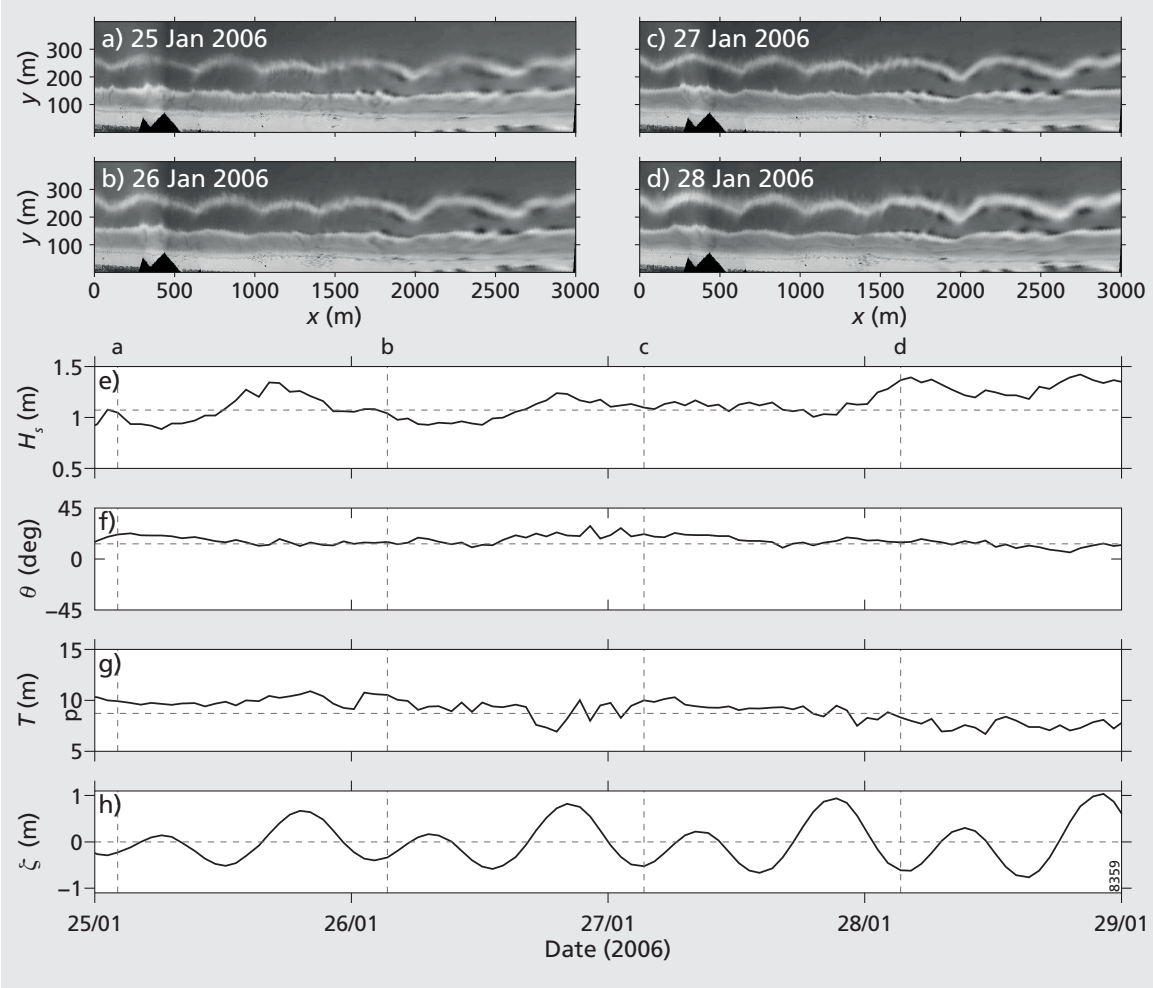

Figure 4.3 Field data, showing (a-d) time-exposure video images of the observed coupling, time series of the offshore (e) significant wave height H_s (m), (f) angle of wave incidence θ (degrees with respect to shore-normal), (g) peak wave period T_p (s) and (h) tidal water level ζ (m). The horizontal dashed lines in (e-h) indicate the mean values used for the reference case, whereas the vertical dashed lines in (e-h) indicate the moments at which the video images in (a-d) were taken.

4.2.3 Analysis of model results

To examine the evolution and the processes involved in the morphological coupling, we computed a number of parameters representative of the morphological evolution, the flow patterns and sediment transport, respectively. As this study focusses on the response of the terraced inner bar to a crescentic outer bar for given wave conditions, we analysed these parameters at an alongshore profile over the inner terrace at cross-shore distance $y = 120$ m, where we found the processes and morphology to be representative of the inner-bar morphodynamics.

In our model there is no bed diffusion or bed slope transport (Garnier et al., 2008b) likely to dampen the development of instabilities. Depending on the boundary con-

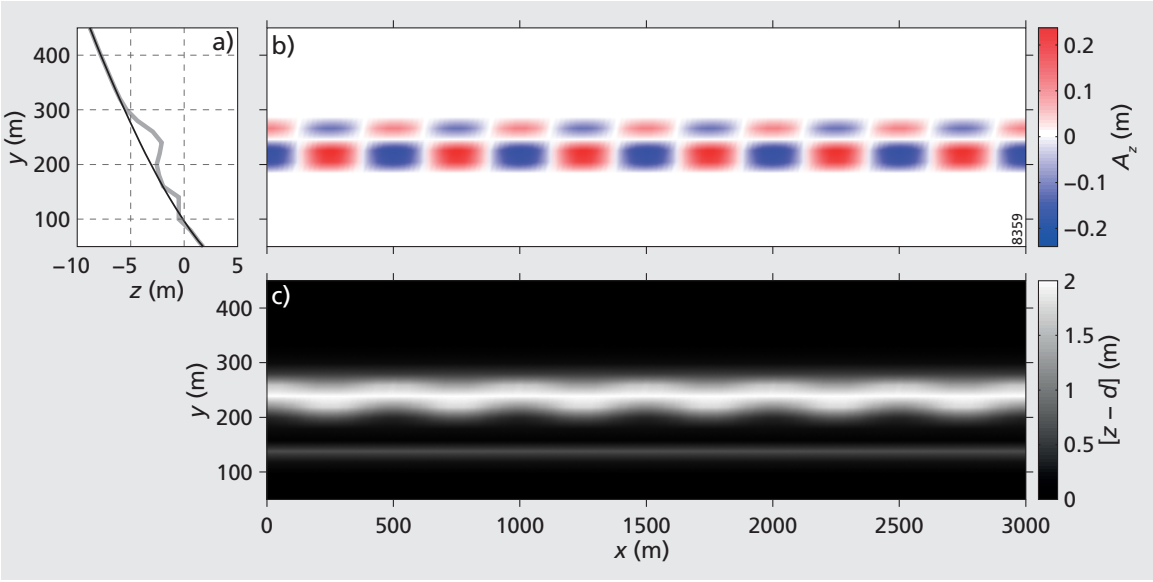

Figure 4.4 The initial double sandbar bathymetry z used for the simulations, with (a) the alongshore-uniform double-barred profile (grey) and the fitted Dean profile d (black), (b) the horn and bay sequence (A_z) superimposed on the alongshore-uniform bathymetry in (a), and (c) the resulting bathymetry with a crescentic outer bar and an alongshore-uniform inner bar, shown here as perturbations $[z - d]$ with respect to the Dean profile in (a).

ditions (both the hydrodynamic forcing as the outer bar morphology) this eventually led to an unrealistic morphology of the inner or outer bar for some simulations. None of the simulations, however, led to a blow up of the model. The analyses of the double sandbar morphology presented below do not represent steady states of the system. Instead, we analyse each model simulation after a simulation time of 2 days (100 morphological timesteps), before the appearance of an unrealistic morphology in any of the simulations.

To quantify the change from horizontal cell-circulation patterns to a more meandering alongshore current, as the angle of wave incidence increases, we compute the swirling strength (Adrian et al., 2000) as a measure for the rotational nature (vortices) of the flow pattern. The swirling strength is extracted from the velocity fields, using critical-point analysis of the local velocity gradient tensor and its corresponding eigenvalues (Zhou et al., 1999). Firstly, the velocity gradient tensor of the xy-plane is computed as

$$V = \begin{pmatrix} \frac{\partial U_y}{\partial y} & \frac{\partial U_y}{\partial x} \\ \frac{\partial U_x}{\partial y} & \frac{\partial U_x}{\partial x} \end{pmatrix}, \tag{4.5}$$

where U_y and U_x are the cross-shore and alongshore velocities (which constitute $\vec{U}$), respectively. Subsequently, complex eigenvalue pairs of V, each consisting of a real part (λ_{cr}) and an imaginary part (λ_{ci}), indicate the presence of a vortex in the velocity field. In this case, λ_{ci} provides the measure for the swirling strength, where vortices can be identified as regions where $\lambda_{ci} > 0$, and λ_{ci}^{-1} represents the period (seconds)

required to spiral around the origin of the vortex. Essential to our analysis of the rotational nature of the flow over the inner bar, the swirling strength λ_{ci} conveniently isolates the rotational parts of the flow and excludes regions with large shearing motion (and no swirling motion), as may be expected for cross-shore differences of the velocity in a purely alongshore (unidirectional) current.

4.3 Results

4.3.1 Reference simulation

Before analysing any change in processes at the inner bar, we first present the reference simulation, with $H_s = 1.1$ m, $\theta = 14°$, $T_p = 9$ s and $\zeta = 0$ m. This reference simulation serves two purposes: firstly, the evaluation of the agreement between the computed and the observed inner-bar Idt morphology, and, secondly, it permits the comparison of model results obtained for varying angles of wave incidence.

Figure 4.5a shows the bathymetry after 2 days of simulation. The obliquely incident waves approach from the right top. The inner bar has developed landward perturbations (along $y = 120$ m, e.g. at $x \approx 400$, 900, 1400 m), which are slightly offset with respect to the alongshore position of the outer-bar horns (along $y = 220$ m, e.g. at $x \approx 300$, 800, 1300 m). This morphology resembles the Idt coupling type, with landward perturbations of a similar magnitude and position with respect to the outer bar as in the observations in Figure 4.3. In the depth profile along the inner bar (at $y = 120$ m), the flat, terraced morphology is interrupted by perturbations with a depth of approximately 0.4 m (Figure 4.5b). In our simulations, depth-induced wave breaking across the entire outer bar resulted in lower wave energy shoreward of the outer-bar horns. The dominant direction of the wave-driven flow over the inner bar, and the entire nearshore area (Figure 4.5c), is from right to left in the figure. At the inner bar, this alongshore flow meanders in onshore- and offshore-direction. The meandering nature of the alongshore flow becomes clear from the cross-shore component of the flow (the colours in Figure 4.5c), which shows a change in flow direction from more onshore-directed over the flat terraced area to more offshore-directed at the landward perturbations of the inner barline. A weaker meandering current also prevails over the outer bar horns, with more onshore-directed flow downdrift of the outer-bar horns, and more offshore-directed flow updrift of the outer-bar horns. These fluctuations at both the inner and outer bars, however, do not lead to a rotational flow over the inner bar, and the swirling strength remains zero over the entire domain (Figure 4.5d). Similar to the flow pattern, the main direction of the resulting sediment transport fluxes $\vec{Q}_s$ is alongshore-directed with fluctuations in onshore and offshore direction (Figure 4.5e). The accretion/erosion patterns show that the landward perturbation at the inner bar is situated directly between an area of accretion and erosion, indicating that the perturbation migrates alongshore, reminiscent of the relation between sediment transport and alongshore rip channel migration identified by Orzech et al. (2010). This alongshore migration, further discussed in Section 4.4, is a result of the alongshore-migrating outer bar, causing the morphological template,

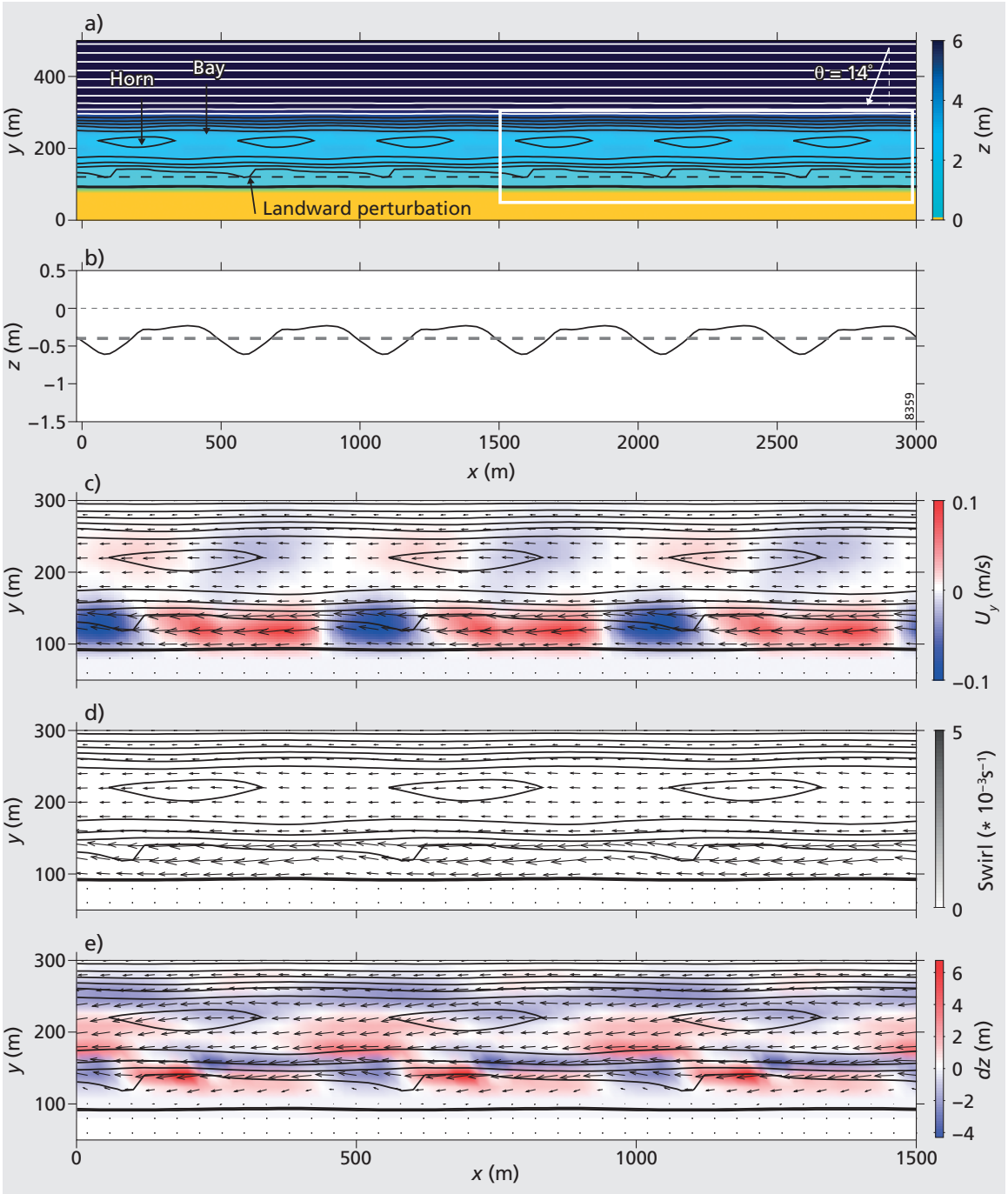

Figure 4.5 Reference case after 2 days of simulation, showing (a) the bathymetry, (b) the depth z along $y = 120$ m, where the thick dashed line indicates the mean depth and the thin dashed line indicates the mean water level. Zoomed in on box indicated in (a), showing (c) the cross-shore flow component U_y, and flow velocity $\vec{U}$ (arrows), (d) the swirling strength and $\vec{U}$ (arrows), and (e) dz showing accretion (red) and erosion (blue) patterns, and sediment transport fluxes $\vec{Q_s}$. Isobaths (0.5 m intervals) are contoured in the background.

and thus the forcing at the inner bar, to change. Accretionary areas at the inner bar coincide with more onshore-directed sediment transport directly updrift of the inner-bar perturbation, whereas erosional areas coincide with more offshore-directed sediment transport originating at the inner-bar perturbation.

These results indicate that the model is capable of reproducing the landward perturbations in the inner bar observed during the Idt coupling type. In contrast to other coupling types, with more shore-normal wave incidence, the Idt coupling type had thus far not been simulated. The robustness of this modelling result is further discussed in Section 4.4. The landward perturbations are erosional features, and their location coincide with the turning-point of the meandering alongshore current, where more onshore-directed flow and accretion turn to more offshore-directed flow and erosion. In that sense, the landward perturbation in the inner bar is comparable to the erosive mega-cusps in the shoreline at the base of rip channels, often observed in single-barred systems (e.g., see Komar, 1971; Thornton et al., 2007).

4.3.2 Influence of wave angle

Below, we characterise the change in processes at the inner bar for angles of wave incidence varying from 0° to 20°. Before doing so, we first present a simulation with a more shore-normal wave incidence than in the reference simulation to aid the interpretation of the results.

Simulation with $\theta = 5^\circ$

Figure 4.6 shows the model results for more shore-normally incident waves ($\theta = 5°$), after 2 days of simulation, similar to Figure 4.5. In this case, the depth perturbations in the inner bar are more pronounced and correspond to clear rip channels with rip-head bars onshore of the outer-bar horns (Figure 4.6a). This morphology corresponds to the Odr coupling type defined in Chapter 3 and the out-of-phase coupling modelled by Castelle et al. (2010a). Note the subtle mega-cusps in the shoreline, at the base of the rip channels. The depth variations along the inner bar (Figure 4.6b) show the rip channels with depths of approximately 0.7 m. A cell-circulation pattern characterises the flow over the inner bar, with onshore flow over the bar, offshore flow through the rip channels (Figure 4.6c), and feeder currents on either side of the rips. The non-zero angle of wave incidence induces an asymmetric cell-circulation with a downdrift deflection of the rip current. It is also downdrift of the rip channel, near the shoreline, where the rotational nature of the flow is most apparent. The swirling strength (Figure 4.6d) clearly captures this pronounced rotational flow over the inner bar, both downdrift of the rip channel as in the rip channel itself. The resulting sediment transport fluxes $\vec{Q}_s$ and accretion/erosion patterns (Figure 4.6e) at the inner bar show onshore sediment transport and accretion over the bar and offshore sediment transport through the rip, leading to the erosion of rip channels and the formation of rip-head bars. In contrast to the reference case, where the accretionary area was updrift of the inner-bar perturbation, here the onshore sediment transport flux is largest downdrift of the inner-bar rip (and outer-bar horn).

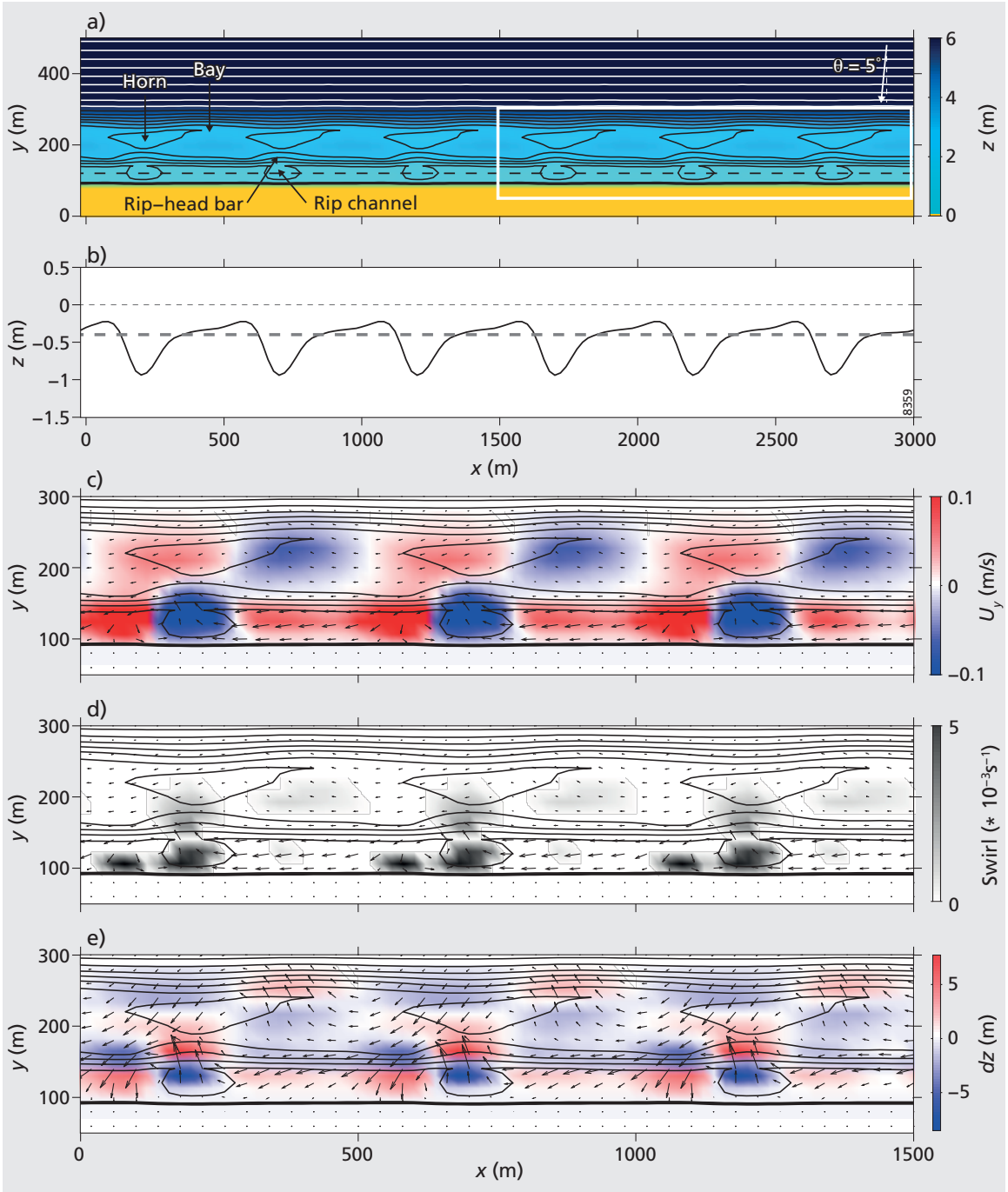

Figure 4.6 Simulation with $\theta = 5°$ after 2 days of simulation, showing (a) the bathymetry, (b) the depth z along $y = 120$ m, where the dotted line indicates the mean depth and the dashed line indicates the mean water level h. Zoomed in on box indicated in (a), showing (c) the cross-shore flow component U_y, and flow velocity $\vec{U}$ (arrows), (d) the swirling strength and $\vec{U}$ (arrows), and (e) dz showing accretion (red) and erosion (blue) patterns, and sediment transport fluxes $\vec{Q_s}$. Isobaths (0.5 m intervals) are contoured in the background.

Depth perturbations

Figures 4.5b and 4.6b indicated that inner-bar depth perturbations were more pronounced for a smaller angle of wave incidence ($\theta = 5°$) than for the reference case with $\theta = 14°$. Figure 4.7 shows the depth perturbations with respect to the alongshore-averaged bathymetry z_p and flow (arrows) along the inner bar, at $y = 120$ m, for the simulations with varying angles of wave incidence after 2 days of simulation. The negative z_p values correspond to the landward perturbations and rip channels in Figures 4.5 and 4.6, respectively. The most pronounced depth perturbations are found for the simulations with θ around 7° (Figure 4.7c), where relatively deep and narrow negative depth perturbations are formed, i.e. rip channels. This is somewhat surprising, as previous modelling exercises of single bar systems (e.g., Castelle and Ruessink, 2011) found that rip channels were more pronounced when formed during shore-normal wave incidence. For $\theta > 7°$, the negative depth perturbations decrease, but become increasingly wider. Similarly, the positive depth perturbations directly downdrift of the negative depth perturbations decrease, indicating an increasingly subdued inner-bar morphology. Towards $\theta = 20°$, almost all depth perturbations have disappeared. From $\theta = 0°$ to approximately $\theta = 10°$ the magnitude of the flow increases (the arrows become longer), while the flow pattern remains circulatory. For $\theta > 10°$ the flow pattern subsequently changes to a meandering alongshore current, becomes increasingly unidirectional and increases in magnitude. Notice that the depth perturbations are located further to the left (downdrift) for larger angles of wave incidence. This relates to the combination of the increased magnitude of the alongshore current and the concurrent alongshore migration of the outer bar, further discussed in Section 4.4.

Swirling strength

Figure 4.8 shows the flow pattern along the inner bar at $y = 120$ m for all θ simulations after 2 days of simulation, together with the swirling strength, to capture the change in rotational nature of the flow over the inner bar. A swirling motion of the flow over the inner bar can only be detected for angles of wave incidence up to $\approx 10°$. For larger angles, the rotational features disappear and a meandering alongshore current prevails, as in the reference case (Figure 4.5). In line with the depth variations (Figure 4.7), the maximum swirling strength is found for $\theta = 5°$ (Figure 4.8b). Surprisingly, the swirling strength (i.e. the intensity of the cell-circulation) is not largest for shore-normal incidence. Instead, the largest swirling strengths develop for waves with a slight oblique incidence ($\theta = 4$ - $6°$); the presence of an alongshore component in the mean flow seems to intensify both the flow through the (obliquely oriented) rip channels, and the swirling motion on the downdrift side of the rip channel (Figure 4.6). As θ approaches 10°, the feeder current directly downdrift of the rip channel becomes weaker and eventually disappears as it becomes overridden by the alongshore current. Similarly, for $\theta < 6°$, a more subtle swirling motion is detected updrift of the rip channel, over the bar, coinciding with the alongshore position of the outer-bar bay (e.g., at $(x, \theta) = (650\text{ m}, 5°)$, see also Figure 4.6d). Here, for $\theta < 3°$, the onshore-directed flow splits into two feeder channels towards the rip channels on

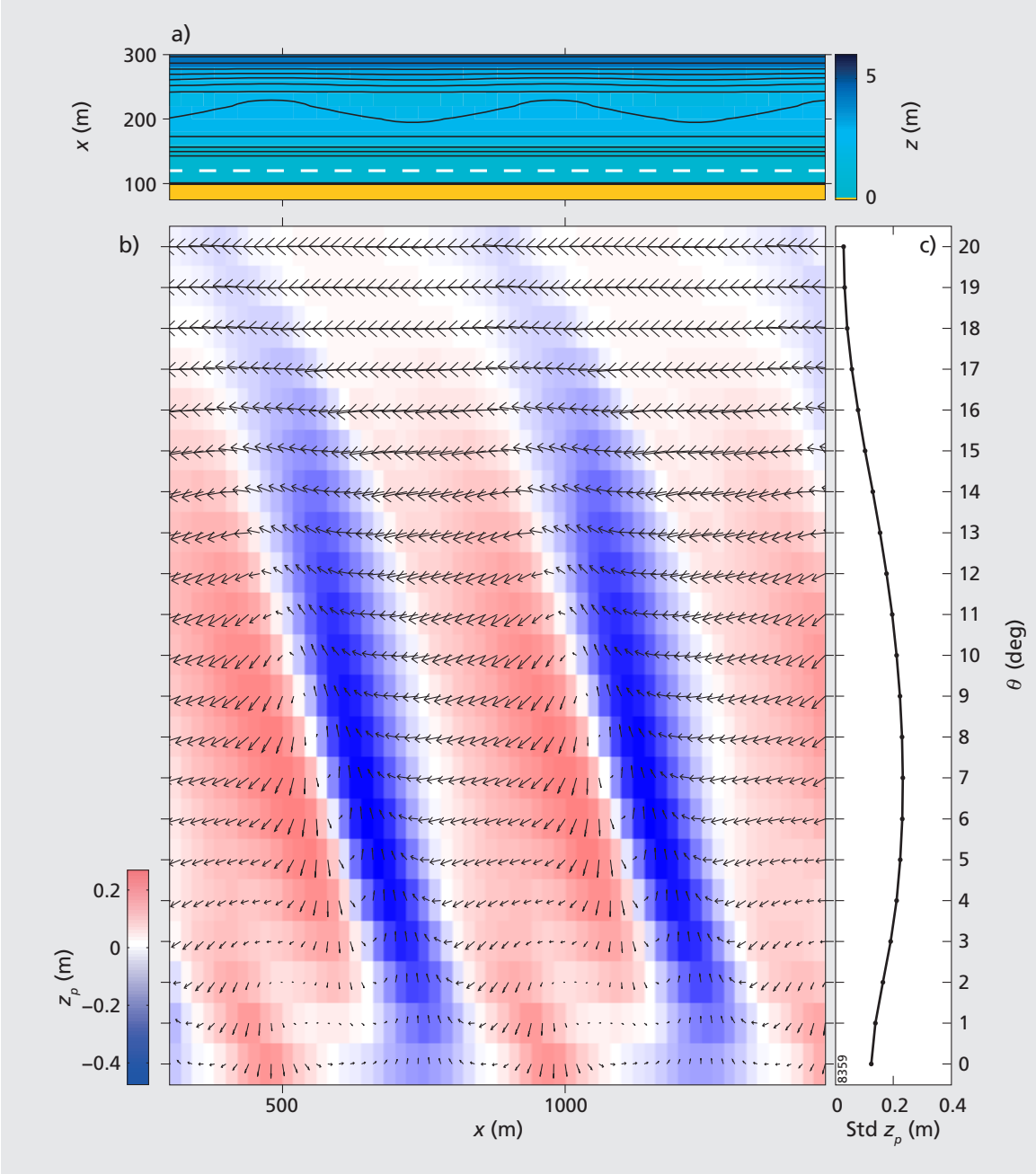

Figure 4.7 Model results, showing (a) the initial bathymetry, with isobaths (0.5 m intervals) contoured in the background, (b) flow velocity $\vec{U}$ (arrows) and the depth perturbations z_p (colour) along the inner bar at $y = 120$ m for all simulations after 2 days of simulation, and (c) the corresponding standard deviation of the depth z_p along the inner bar at $y = 120$ m.

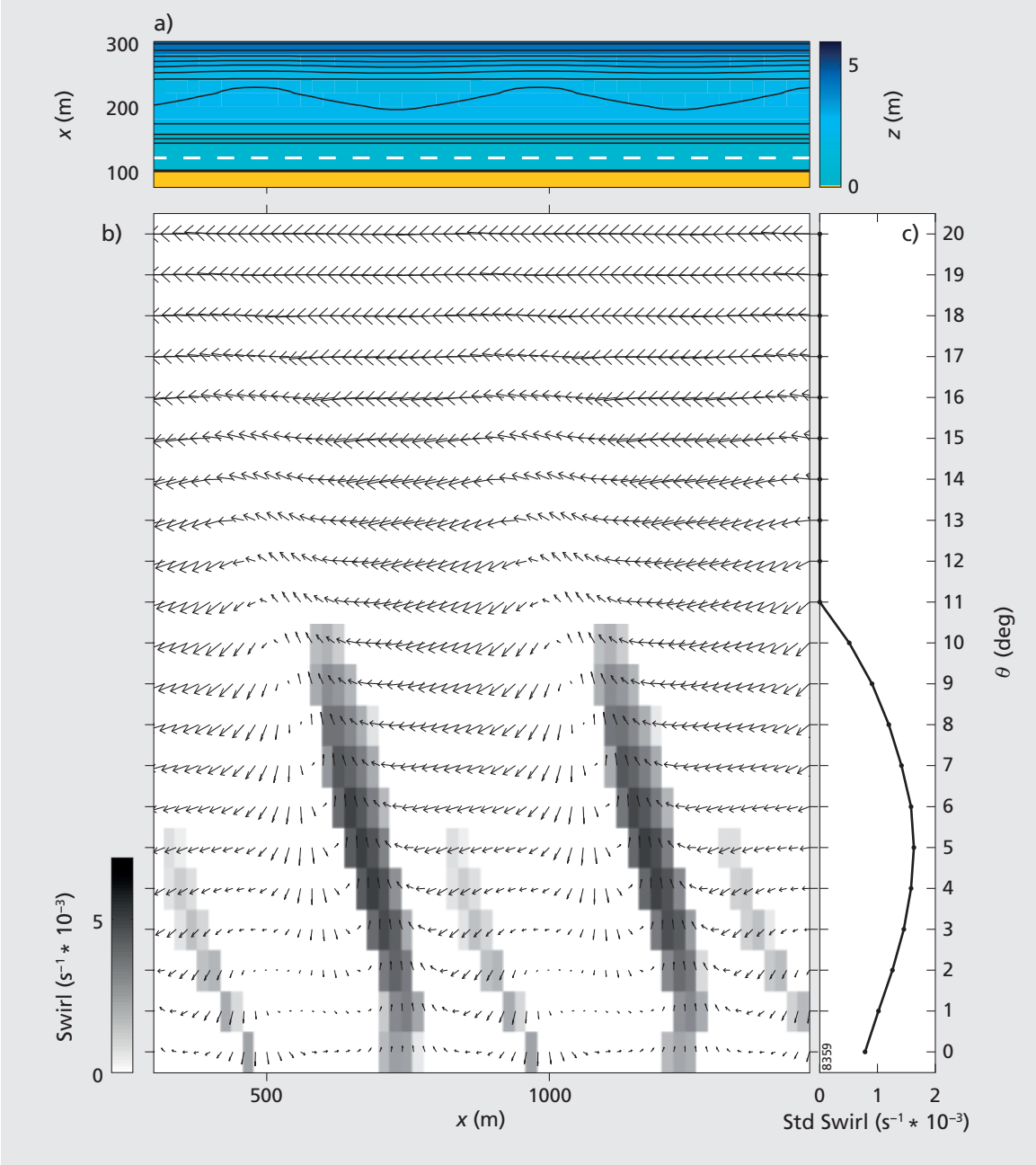

Figure 4.8 Model results, showing (a) the initial bathymetry, with isobaths (0.5 m intervals) contoured in the background, (b) flow velocity $\vec{U}$ (arrows) and swirling strength (shaded) along the inner bar at $y = 120$ m for all simulations after 2 days of simulation, and (c) the corresponding standard deviation of the swirling strength along the inner bar at $y = 120$ m.

either side. For $\theta > 2°$, the onshore-directed flow at this area becomes increasingly alongshore-directed and the splitting point shifts to the area directly downdrift of the more pronounced rip channel described above (e.g., at $(x, \theta) = (400 \text{ m}, 3°)$. Note that smaller outer-bar wavelengths or larger waves may result in stronger circulation patterns, which persist through larger angles of wave incidence than shown herein (see Castelle et al., 2010a).

Sediment transport

Figure 4.9 shows the accretion/erosion (dz) and sediment transport flux $\vec{Q}_s$ along the inner bar, at $y = 120$ m, for all simulations at $t = 2$ days. The erosional areas correspond to the coupled inner-bar perturbations. In agreement with the depth and flow variations, the erosion of the rip channels increases from $\theta = 0°$ to $\theta = 7°$. As the rip channel becomes more pronounced (Figure 4.7), an area of onshore sediment transport and accretion develops downdrift of the rip current, corresponding to the pattern in Figure 4.6e. For $\theta > 10°$, both the accretion downdrift of the rip channel and the erosion of the rip channel itself quickly decrease, and an area of onshore sediment transport and accretion starts to develop updrift of the inner bar perturbation. This accretion/erosion pattern corresponds to Figure 4.5e, which indicates the development of the inner-bar perturbation under more alongshore-directed sediment transport conditions. For even larger angles of wave incidence ($\theta > 17°$), the sediment transport direction becomes increasingly alongshore-uniform and bed level changes decrease. The weak erosional areas updrift of the rip channel for $\theta < 6°$ (e.g., at $(x, \theta) = (500 \text{ m}, 5°)$) correspond to the aforementioned swirling strength pattern (Figure 4.8), and indicate the development of subtle channels at the inner bar (see Figure 4.7).

In summary, for $\theta > 10°$ the Idt coupling type developed. In this case, the offshore-directed sections of the meandering current downdrift of the outer-bar horn eroded the inner terrace, causing the coupled inner-bar features to appear as landward perturbations of the terrace edge. For $\theta < 10°$ cell-circulation patterns governed the flow at the inner bar. In our simulations, where waves broke across the entire outer bar, this circulatory pattern led to the Odt coupling type, with offshore flow and the development of rip channels in the inner bar at the locations of the outer-bar horns, consistent with Castelle et al. (2010a). The most pronounced rip channels and circulatory flow patterns were found around $\theta \approx 7°$. These results confirm our hypothesis that the angle of wave incidence is crucial to the flow pattern and sediment transport at the inner bar, and thus the emerging coupling type.

4.4 Discussion

Our simulations show the importance of the angle of wave incidence over a crescentic outer bar for the inner-bar morphodynamics. In this section, we substantiate our results by discussing the influence of bar depth, including tidal variation in our reference simulation, and by further discussing model limitations.

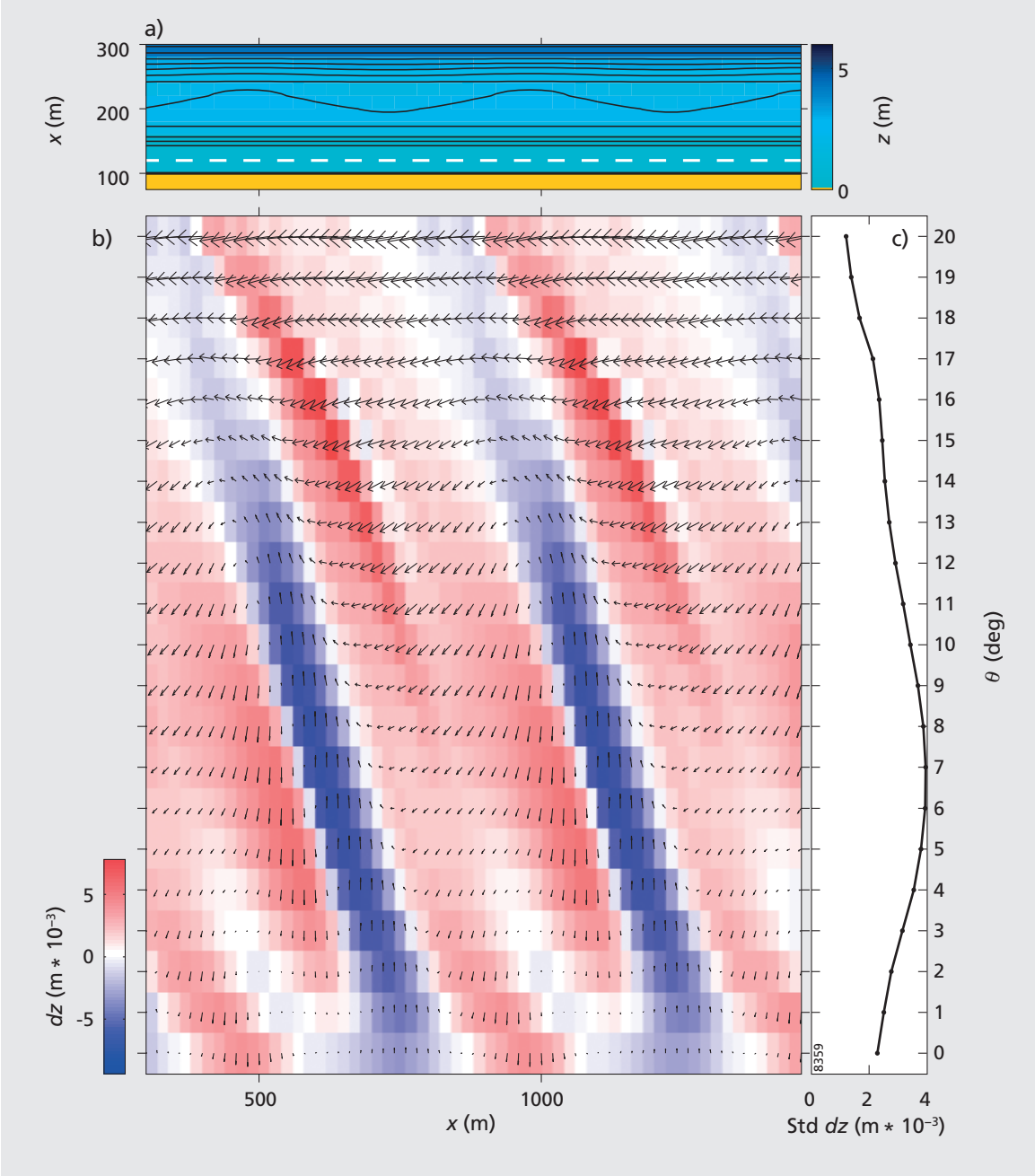

Figure 4.9 Model results, showing (a) the initial bathymetry, with isobaths (0.5 m intervals) contoured in the background, (b) sediment transport flux $\vec{Q}_s$ (arrows) and accretion/erosion dz (red/blue) along the inner bar at $y = 120$ m for all simulations after 2 days of simulation, and (c) the corresponding standard deviation of the accretion/erosion dz along the inner bar at $y = 120$ m.

4.4.1 Inner and outer bar depth D_i and D_o

Although the assimilation results using XBeachWizard provided a suitable estimate of the alongshore depth variation of the outer sandbar, the absolute depth depended strongly on the model settings used for the assimilation, see Appendix A for details. Accordingly, we reran a series of simulations where the depths of the inner and outer bars were varied within a realistic range, while keeping both the morphological variables (bar position, wavelength, cross-shore extent and alongshore depth-variation of the crescentic outer bar) and the hydrodynamic boundary conditions (H_s, θ, T_p, h) constant; after all, these are known. The range over which to vary the outer bar depth was obtained through the results of the XBeachWizard simulations, which yielded an average outer-bar depth of -1.7 m MSL, and the scarce amount of bathymetries (Ruessink et al., 2009) over the period 1999–2006, yielding outer-bar depths ranging from -2.5 to -1.5 m MSL. In the measured bathymetries the inner-bar depths ranged from approximately -1 to -0.2 m MSL, and visual inspection of snapshot video images and the corresponding tidal levels (to determine at what water level the inner bar emerged), yielded inner-bar depths of approximately -0.5 m MSL. In total we performed 42 simulations to assess the variability of the coupled morphology reproduced by the model, with outer-bar depths ranging from -2.5 to -1.3 m MSL, and inner-bar depths ranging from -1.0 to 0 m MSL.

All of the 42 simulations resulted in a meandering alongshore current, and a landward perturbation in the inner bar downdrift of the outer-bar horn (as in Figure 4.5). Both for smaller inner- and outer-bar depths, the (cross-shore) amplitude of the meanders increased. Similarly, the morphological response of the inner bar was more pronounced for smaller inner- and outer-bar depths than for larger depths, and eventually led to the inner bar reaching zero depth for small inner bar depths. Qualitatively, however, the resulting morphology was the same. For the given depth ranges, the inner- and outer-bar depths thus mainly determined the speed of the morphological evolution of the inner bar, and not the characteristics of the evolving bathymetry. For the simulations presented herein, we applied an outer bar depth D_o of -2.1 m MSL and inner bar depth D_i of -0.5 m MSL, where the choice for the outer-bar depth was a compromise between a realistic depth and realistic morphological response times.

4.4.2 Influence of a tidal water level variation

Despite variations in D_o and D_i giving consistent results, we additionally investigated the model predictions by taking tide into account, further bridging the gap towards model-data integration. For our simulations we used time-invariant wave-forcing, including a constant tidal water level ζ of 0 m. The water level variation in our observations of the Idt coupling type, however, show a tidal amplitude of approximately 0.5 m (Figure 4.3h). Furthermore, in the video images, the inner bar regularly emerged during low tide. Besides a variation in water depth and the potential introduction of tidal-induced currents, a tidal amplitude results in a variation of processes over a cross-shore profile, as the surf zone sweeps across the profile during a tidal

cycle (e.g., Masselink and Short, 1993), and in a temporal change in the magnitude of rip current velocities (e.g., Schmidt et al., 2005; Austin et al., 2010). Although numerous field studies of nearshore currents and sandbar morphodynamics at sites with a tidal range exist, numerical modelling efforts concerning the development of 3D sandbar behaviour under the influence of tides are scarce. Castelle et al. (2010a) suggested that the tide continuously changes the balance between wave breaking and refraction across the outer bar, which they found to be the two mechanisms to be important for differences in coupling types for shore-normally incident waves.

To investigate the influence of the tide, and to test whether the model still reproduces the Idt coupling type when tidal variation is included, we ran a number of simulations with different tidal amplitudes. We varied the tidal amplitude from 0.1 to 1 m (the spring tidal amplitude at our study site), with steps of 0.1 m, while applying a 12-hour tidal period and keeping all other boundary conditions the same as in the reference simulation, with $H_s = 1.1$ m, $\theta = 14°$ and $T_p = 9$ s. The difference $\Delta\overline{\zeta}$ between the mean of the high tides $\overline{\zeta_{high}}$ and the mean of the low tides $\overline{\zeta_{low}}$ in the observation period (Figure 4.3h) was 1.0 m, corresponding to a tidal amplitude of 0.5 m. As the inner bar has a depth D_i of 0.5 m in our simulations, the bar increasingly emerges during a tidal cycle (thus becoming increasingly intertidal) for tidal amplitudes larger than 0.5 m. In Section 4.3 we showed that the development of the landward perturbations in the inner bar coincided with erosional areas downdrift of the outer bar horns. Figure 4.10 shows the 4-day evolution of the accretion and erosion (dz), together with flow velocity $\vec{U}$, along the inner bar at $y = 120$ m for the simulation with a tidal amplitude ζ of 0.5 m. During the first 1.5 days, the landward perturbations at the inner bar only develop just before and after low tide (e.g., just before and after $t = 0.4$ days), when both the magnitude and the meandering nature of the alongshore flow become more pronounced. In between these moments, during high tide, the flow is more alongshore-uniform and erosional areas are lacking. After $t = 1.5$ days, the perturbation has become sufficiently pronounced and continues to develop when submerged (i.e., at a minimum water depth). For larger tidal amplitudes, this minimum depth would be reached less frequently during the tidal cycle. For all tidal amplitudes simulated herein, however, our model reproduced the Idt coupling type, similar to the bathymetry in Figure 4.5a. Figure 4.11a shows the sum $\Sigma|dz_{\mathrm{neg}}|$ of the erosional areas along the inner bar, at $y = 120$ m, during the entire simulation for each tidal amplitude, where a tidal amplitude of 0 corresponds to the reference simulation. This shows that larger tidal amplitudes indeed decrease the total amount of erosion along the inner bar during a tidal cycle, and thus hinder the growth of the inner-bar features, consistent with the findings of Dubarbier and

Figure 4.10 (following page) Tidal simulation with a tidal amplitude of 0.5 m with (a) the bathymetry just before 4 days of simulation (indicated by the dashed lines in (b) and (c)), with isobaths (0.5 m intervals) contoured in the background, (b) the temporal evolution of dz (colour) and flow velocity $\vec{U}$ (arrows) along the inner bar at $y = 120$ m, and (c) the time series of the tidal water level ζ. The 0-contour lines in (b) indicate the erosional areas.

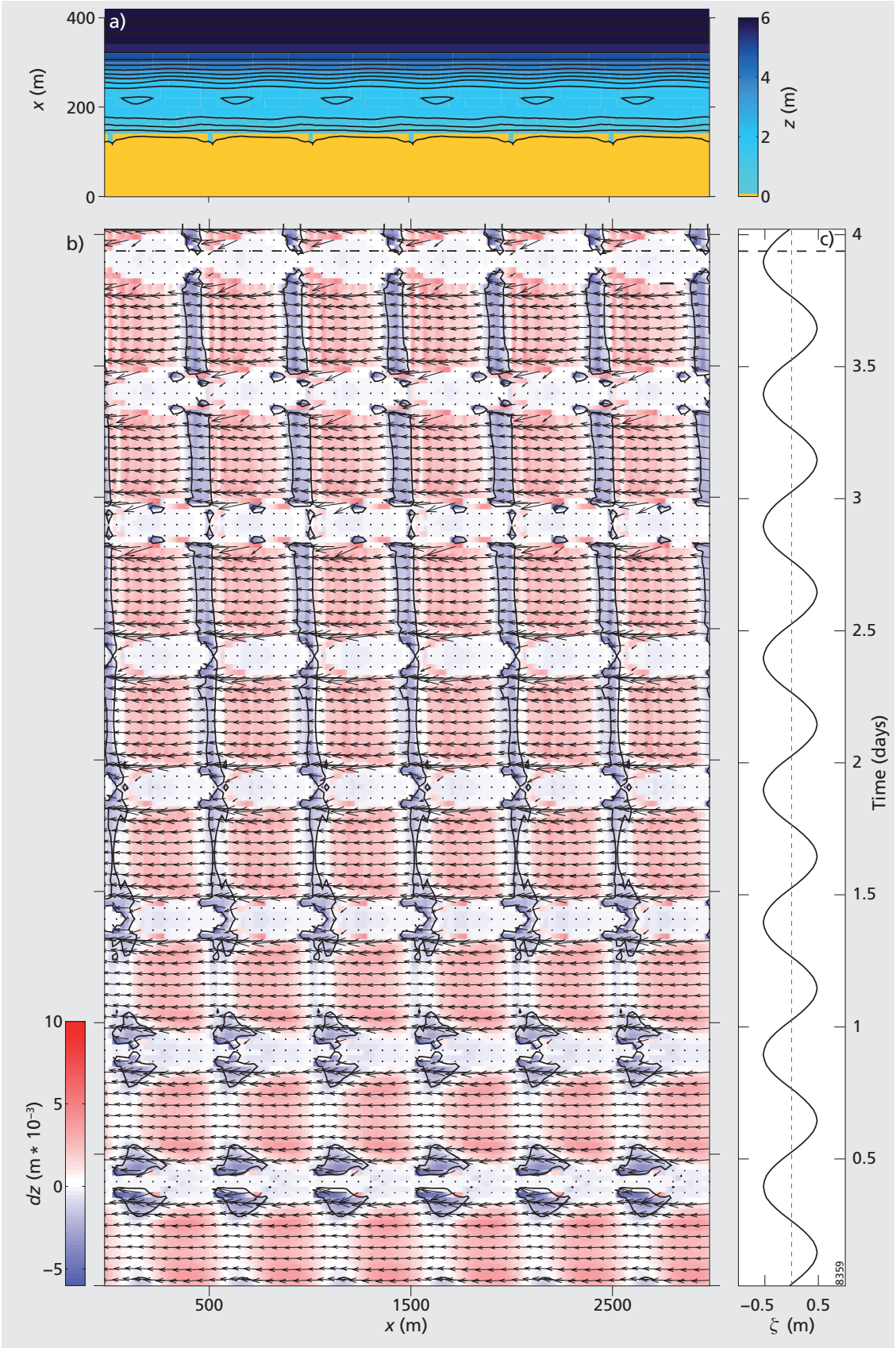
a)
b)
c)
400
200
0
x (m)
6
4
2
0
z (m)
10
5
0
−5
dz (m * 10⁻³)
500
1500
2500
x (m)
−0.5
0.5
ζ (m)
4
3.5
3
2.5
2
1.5
1
0.5
Time (days)
8359

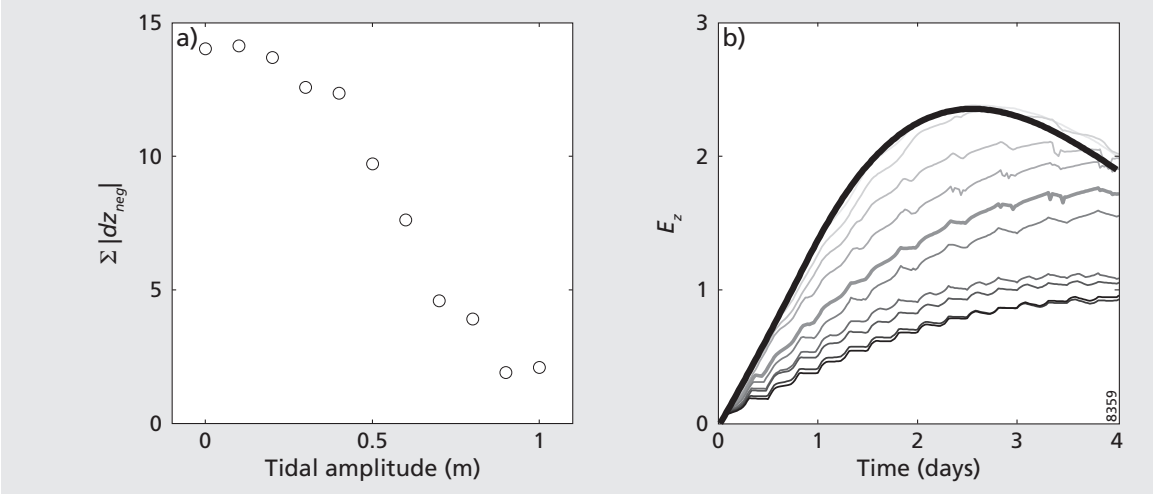

Figure 4.11 Tidal influence on inner-bar coupling, showing (a) the total amount of erosion at the inner bar $\Sigma|dz_{\mathrm{neg}}|$ as a function of the tidal amplitude, and (b) the temporal evolution of the potential energy E_z of the inner bar morphology for simulations with different tidal amplitudes. The thick black line corresponds to the reference simulation, darker (lighter) shades of gray correspond to larger (smaller) tidal amplitudes ranging from $0.1-1.0$ m, and the thick gray line corresponds to the simulation with a tidal amplitude of 0.5 m shown in Figure 4.10.

Castelle (2011). This is further illustrated in Figure 4.11b, which shows the temporal evolution, for each tidal simulation, of the potential energy density E_z of the morphology with respect to the alongshore-averaged profile z_{mean} over the cross-shore extent of the inner bar area from $y_a = 100$ to $y_b = 140$ m, similar to Garnier et al. (2006) and Vis-Star et al. (2008):

$$E_z = \sqrt{\int_0^{L_x} \int_{y_a}^{y_b} \left(z(x,y,t) - z_{\mathrm{mean}}(x,y,t)\right)^2 \mathrm{d}x\,\mathrm{d}y} \tag{4.6}$$

, where L_x is the alongshore extent of the computational domain. Although the smaller tidal amplitudes (< 0.5 m) show a decrease in E_z for $t > 2$ days, larger tidal amplitudes (> 0.5 m) generally lead to a more subdued (i.e. smaller E_z) Idt coupling type morphology of the inner bar. Moreover, the stepwise development of E_z indicates the increasingly discontinuous morphological development of the intertidal inner bar morphology for larger tidal amplitudes.

4.4.3 Model robustness and limitations

The nonlinear modelling exercise presented herein relies on a number of simplifying assumptions. We neglected the 3-D structure of wave-driven circulations (we assume depth-averaged flow), and wave group-scale forcing. The latter is thought to influence the free development of rip currents and rip channel morphology (Reniers et al., 2004). However, our study focusses on the development of inner-bar morphology

forced by the morphological template of the already-crescentic outer bar (i.e., finite-amplitude behaviour), and not on the free development of an initially alongshore-uniform nearshore morphology in response to a given set of offshore wave conditions. If the inner-bar morphology were to develop freely, larger alongshore spacings of the inner-bar features would be expected for increasing angles of wave incidence, as demonstrated by, among others, Smit et al. (2008) and Deigaard et al. (1999) for constant offshore wave forcing. Our results, however, showed no change in inner-bar spacing (see Figure 4.7b), verifying our assumption that the inner-bar morphology is indeed governed by the presence of an alongshore-variable outer bar.

Overall, the numerical model was capable of reproducing the observed Idt coupling type. The model slightly overpredicted the alongshore migration of the outer-bar patterns and, therefore, the inner-bar features. Figure 4.10 shows an alongshore migration of the inner-bar features of $\approx$ 100 m over the 4-day modelling period, whereas both the inner-bar and outer-bar patterns in the observations hardly exhibit any alongshore migration (Figures 4.3a-d). The systematic overestimation of rip channel migration rates with nonlinear morphodynamic models has already been pointed out by Falqués et al. (2008). Furthermore, an inner bar with an initial degree of alongshore variability, as in the observations, may respond differently to a given forcing than an initial perfectly alongshore-uniform inner bar, as in the model (e.g., Tiessen et al., 2011; Smit et al., 2012, and Chapter 2). Similarly, using time-variant wave forcing potentially results in different bar morphodynamics than when using mean values (Castelle and Ruessink, 2011).

4.5 Conclusions

We applied a non-linear model with data-based, time-invariant forcing to test our hypothesis that, for a given crescentic outer-bar, the angle of wave incidence θ is crucial for the inner-bar morphodynamics. Obliquely incident waves ($\theta > 10^{\circ}$) over a crescentic outer bar lead to cross-shore undulations of the inner terrace edge that are coupled to the outer bar morphology, confirming our hypothesis that this type of coupling develops during oblique wave incidence. In this case, a meandering alongshore current and more alongshore-directed sediment transport dominates. The offshore-directed sections of the meandering current, downdrift of the outer-bar horn, erode the inner terrace, resulting in the development of landward perturbations of the terrace edge coupled to the outer-bar horns. For more shore-normal wave incidence ($\theta < 10^{\circ}$), on the other hand, cell-circulation patterns govern the flow at the inner bar, leading to coupled rip channels that are incised through the inner terrace. In agreement with both the hypothesis and our observations from a natural double-barred beach, the modelling exercise shows that the angle of wave incidence is crucial to the flow pattern, sediment transport, and thus the emerging coupling type at the inner bar.

Acknowledgements

TDP and BGR acknowledge financial support by the Netherlands Organisation for Scientific Research (NWO), under contract 818.01.009. BC acknowledges financial support through the BARBEC project (ANR N2010 JCJC 602 01). We thank Martijn Henriquez for his help on computing the swirling strength.

5 Conclusions and perspectives

5.1 Conclusions

The general aim of this thesis was to increase the understanding of the finite-amplitude behaviour of crescentic sandbars in a double-barred system. Using both over 9 years of daily observations from the Gold Coast, Australia and a non-linear numerical model, several important aspects of the behaviour of a double sandbar system were presented herein. Below, I first summarise how the research goals stated in Chapter 1 were answered, leading to the main conclusions of this thesis. I thereupon merge and discuss these findings to form a coherent view of the finite-amplitude behaviour of crescentic sandbars in a double-barred system in Section 5.2. While doing so, I also address several research perspectives.

In Chapter 1, I stated the three research goals I aimed to answer in this thesis. Below, I summarise the findings related to each research goal.

1. *Establish the morphodynamic states that characterise a double sandbar system.* An important first step in addressing the overall aim of this thesis was to characterise the typical development of the alongshore variability within a double-barred system. As outlined in Section 1.2.1, Short and Aagaard (1993)'s conceptual bar-state model provides a convenient framework for describing *when* such alongshore variability is encountered. To this end, I developed a method to objectively classify the inner- and outer-bar states from the Gold Coast images in Chapter 2. Besides the bar states distinguished by Wright and Short (1984), two additional bar states were found. The first type was characterised by highly oblique rip channels with a more-or-less uniform bar, which I referred to as the erosive transverse bar and rip (eTBR) state. The second additional bar type was characterised by a terrace-shaped bar with quasi-rhythmic alongshore undulations of the terrace edge, which I referred to as the rhythmic low-tide terrace (rLTT) state. Just as the LTT state, the rLTT state was only reached by the inner bar.

   During the 9 years studied, the outer bar was predominantly alongshore variable, being in the TBR state 37% of the time and in the RBB state 24% of the time. The outer bar reached the alongshore-uniform LBT state 14% of the time, where it remained with a median duration of 9 days before regaining alongshore variability, which remained with a median duration of 13 (RBB) to 24 (TBR) days. The eTBR state was the least observed outer-bar state (5% in time), and with a median duration of 3 days it was also the most ephemeral bar state. Despite the limited amount of episodes during which the outer bar reached the D state (7 in total), it was observed 18% in time. This relates to the subdued morphology of the outer bar during this state, leading to an inactive bar and,

hence, a large median residence time of 49 days. The inner bar was generally more downstate and had shorter residence times for each state than the outer bar. Overall, during the 9 years, the rLTT state was observed most frequently (44% in time), with a median duration of 7 days. However, the dominant inner-bar state and residence time were found to depend on the state of the outer bar. For the dissipative outer-bar state, rip channels dominated the inner bar morphology with TBR as the most frequent inner-bar state (60% in time). In this case, the median residence time of the inner TBR state was 9 days, as opposed to a median of 6 days for all outer-bar states. For intermediate outer bar states, on the other hand, the inner rLTT state was most dominant (52% in time).

The outer bar generally advanced sequentially through the states LBT–RBB–TBR–eTBR–LBT, with occasional abrupt transitions to the dissipative state during high-energetic events with mean wave heights $\bar{H}_{\mathrm{rms}}$ above 2 m. Although moderately-energetic events (where $\bar{H}_{\mathrm{rms}} = 1 - 2$ m) led to abrupt state transitions of the outer bar, they did not necessarily correspond to upstate transitions. Similarly, low-energetic periods (where $\bar{H}_{\mathrm{rms}} = 0.5 - 1$ m) did not necessarily lead to downstate transitions. Instead, the angle of wave incidence with respect to shore-normal θ determined whether the outer bar straightened or not; downstate transitions during moderately-energetic wave events were mainly limited to mean absolute wave angles $|\bar{\theta}| < 30°$, whereas upstate transitions during low-energetic periods were mostly found for $|\bar{\theta}| > 20°$, highlighting the role of alongshore currents in the straightening of crescentic sandbars. For this bar straightening under oblique wave incidence, the eTBR state formed the upstate transition from TBR to LBT. Whereas the morphodynamics of the outer bar could be related to the offshore wave conditions, the inner-bar dynamics were largely governed by the state of the outer bar. As more wave energy reached the inner bar during the dissipative outer-bar state, the inner bar behaviour more resembled that of a single-barred system, with its frequent separation from the shoreline and the persistent development of rip channels. Besides the inner-bar state being governed by the outer bar, the terrace edge of the inner rLTT state during intermediate outer-bar states often contained an alongshore rhythmicity similar to that of the outer bar, implying some sort of morphological coupling.

2. *Determine the importance of morphological coupling for the overall behaviour of a double sandbar system.*
   In Chapter 3, I further investigated the apparent morphological coupling between the inner and outer sandbars observed in Chapter 2, and quantified *when* sandbars coupled. Using cross-correlation on the image-derived inner- and outer-bar patterns, I found coupling to be a common phenomenon, at 40% of the observations, with the predominance of in-phase coupling (85%) over out-of-phase coupling (15%). The coupled inner- and outer-bar features were not always exactly in- or out-of-phase, but, instead, often contained an alongshore offset ranging from 0 to 100 m. In correspondence with the dominance of the

inner-bar rLTT state found in Chapter 2, the coupled inner-bar features mainly consisted of perturbations in the low-tide terrace; coupled rip channels were less common. I distinguished 5 types of morphological coupling, according to whether the bars were coupled in- or out-of-phase (I or O), the outer bar proceeded downstate or upstate (d or u), and whether the inner-bar morphology was terraced or with rips (t or r). The most frequent coupling type was the Idt type, an outer crescentic bar with landward perturbations of the inner terrace coupled to the alongshore positions of the outer-bar horns.

As a first step towards *why* different coupling types developed, I related the observed trends to a set of representative coupling events. This led to the hypothesis that the large mean angle of wave incidence at the study site determined the predominance of both in-phase coupling and the preference for undulations in the inner terrace over rip channels. In correspondence with previous numerical studies, rip currents in the inner bar were found for near shore-normally incident waves over a crescentic outer bar. Depending on the wave height and the depth variation of the outer bar, circulation patterns invoked rip channels that either developed in-phase (the Idr coupling type) or out-of-phase (the Odr coupling type) with the outer-bar geometry, without an alongshore offset. The dominant oblique wave incidence at the study site, however, inhibited the frequent development of either of these coupling types. I hypothesised that for obliquely incident waves over an existing crescentic outer bar, circulation patterns at the inner bar become inferior to the magnitude of the alongshore current. Instead, the alongshore current follows the crescentic shape of the outer bar and veers landward at the horns, forming landward perturbations in the inner terrace down-current of the outer-bar horns, resulting in the Idt coupling type. In general, the coupled inner-bar perturbations of the Idt coupling type had a down-current offset of 30 m. This alongshore current along the inner bar seemingly prevented the outer-bar horns from welding to the inner bar. Smaller wave heights with corresponding weaker alongshore currents, however, allowed the crescentic outer bar to reach the TBR state as it welded to the terraced inner bar, resulting in the Odt coupling type. Sufficiently energetic, obliquely incident waves caused the outer bar to straighten and its horns to migrate alongshore (the outer eTBR state). This resulted in the upstate coupling type Out, with an alongshore offset of the coupled inner-bar terrace rhythmicities of up to 100 m in up-current direction, or, if the straightening persisted, decoupling of the bars.

3. *Analyse how the angle of wave incidence affects the coupling processes within a double sandbar system.*
   In Chapter 4 I set out to test the hypothesis formed in Chapter 3 as to *why* different angles of wave incidence lead to the development of different coupling types. To this end, I applied a non-linear 2DH numerical model with time-invariant forcing for angles of wave incidence ranging from 0° to 20°. Instead of a purely synthetic modelling approach, I bridged the gap between numerical

modelling and field observations by forcing the model with realistic bathymetric data, which I derived from the video observations using an assimilation model. As such, the boundary conditions for the simulations were based on a representative 4-day period during which the development of an Idt coupling type was observed in Chapter 3. Besides the model's acknowledged capability of reproducing the coupled morphology that forms under more shore-normal wave angles, it proved to be capable of reproducing the observed Idt coupling type, which formed under oblique wave incidence.

In agreement with the hypothesis, the modelling exercise showed that varying angles of wave incidence over an outer crescentic bar caused the coupling processes at the inner bar to change. For $\theta > 10^{\circ}$ a meandering alongshore current eroded the inner terrace downstream of the outer-bar horns, where more onshore-directed flow and accretion turned to more offshore-directed flow and erosion. This resulted in landward perturbations of the terrace edge, consistent with the observations of the Idt coupling type. As such, the landward perturbations of the inner terrace for the Idt coupling type are erosional features. For $\theta < 10^{\circ}$, cell-circulation patterns governed the flow at the inner bar. In the simulations, where waves broke across the entire outer bar, this circulatory pattern led to the Odr coupling type, with offshore flow and the development of rip channels in the inner bar at the locations of the outer-bar horns, consistent with Castelle et al. (2010a). The most pronounced rip channels and circulatory flow patterns were found around $\theta \approx 7^{\circ}$. These results confirm my hypothesis that the dominant Idt coupling type develops during oblique wave incidence, and that the angle of wave incidence is crucial to the flow pattern, sediment transport, and thus the emerging coupling type at the inner bar.

To summarise, the individual sandbars in a double-barred system should not be studied as independent features, but, instead, the interaction within the composite sandbar system should be taken into account. Coupling is an inherent property of the double sandbar system studied here, as the alongshore variability in the inner bar is coupled to that in the outer bar for some 40% of the approximately 9-year study period. Accordingly, the rhythmic LTT, which is not found in single-bar systems, is the modal inner-bar state. Coupling is predominant when the outer bar is alongshore variable, both in position and depth, except for excessively large offshore angles of incidence (here, $\gtrsim 30^{\circ}$) or wave heights (here, $\gtrsim 2$ m) leading to outer-bar straightening and sandbar de-coupling. In addition to offshore wave height and depth variation along the outer bar, the offshore angle of wave incidence is crucial to the type of coupling that emerges. It strongly controls the type of flow pattern over the inner bar, with a change from cell-circulation patterns for approximately shore-normal waves to an alongshore meandering current as the angle increases to $10 - 20^{\circ}$. The latter type of currents lead to the development of the coupling type dominating the present data set – the in-phase coupling with an alongshore offset, Idt.

5.2 Discussion and perspectives

Generality
The results presented in this thesis were based on over 9 years of daily observations from the Gold Coast, Australia. Although this meets the suggested requirements in Chapter 1 of frequent and long-term monitoring for improving the understanding of morphological sandbar behaviour, it remains unknown to what extent the observed behaviour represents the behaviour of other double-barred beaches. Further work is necessary to test the generality of all findings presented here. The obtained results and the developed and applied methodology provide a framework for studying and describing similar data sets of multiple sandbar systems. In general, I expect intersite variability to arise from differences in sandbar mobility, which, in turn, is ascribed to sandbar volume, grain size, bottom slope, tidal range, and wave climate (e.g., see Wright and Short, 1984; Masselink and Short, 1993; Shand et al., 1999; Pape et al., 2010). Besides identifying the role of these potential variables through intersite comparison, numerical modelling becomes essential in testing the concepts formed (see, e.g., Smit et al., 2012).

Previous attempts to relate the occurrence of bar states to the coinciding or preceding (averaged) wave conditions, predominantly the wave energy, have indicated that each bar state may *exist* under a wide range of conditions (e.g., Ranasinghe et al., 2004; Wright et al., 1985). In Chapter 2, I quantified when outer-bar states *changed* in relation to the preceding wave conditions. Besides illustrating how the wave conditions affected bar-state transitions, this also gave insight into the response time of a sandbar. For example, a certain event that led to the straightening of a crescentic bar with a continuous trough (RBB), did not necessarily lead to the straightening of an attached bar (TBR), despite a change in morphology. Probably, if the same event persisted for a sufficient amount of time, the TBR state would also straighten. More generally, as also suggested by Pape et al. (2010), intersite differences in sandbar behaviour are expected to depend on the ratio between the response time of a sandbar and the variability of the wave climate.

The main focus of the results presented in Chapter 3 (and 4) was on events of sandbar coupling. I realise that at other sites coupling may be less frequent, and that the question why sandbars *do not* couple can be seen as equally important. As coupling results from the outer bar acting as a forcing template for the inner-bar morphology (Castelle et al., 2010a), the obvious aspect to consider is the outer-bar morphology. Of the 60% of the time that the sandbars did not couple, 32% can be explained by the lack of alongshore variability of the outer bar (Chapter 2); either LBT (14%) or D (18%). The remaining 28% of the time the outer bar was alongshore variable, but the bar patterns were not coupled. As suggested by Ruessink et al. (2007a), but not addressed here, the distance with respect to the inner bar may play a role. A numerical and physical modelling study by Ranasinghe et al. (2006) showed that, for given wave conditions, the offshore distance of a shoal to the shoreline determined the inshore flow pattern, where a deeper shoal was found to induce weaker inshore currents. On natural beaches, the offshore distance of a bar

generally positively correlates with the bar depth (e.g., Ruessink and Kroon, 1994). A certain alongshore depth variation of an outer bar therefore has a stronger effect on the alongshore variability of inshore flow patterns when situated more onshore, i.e. in shallower water. The bars in the initial bathymetry used for the simulations in Chapter 4 were 100 m apart, corresponding to the mean distance between the bars ar the Gold Coast. In the modelling exercise of Smit et al. (2008), for example, the sandbars were 200 m apart. There, no coupling was (explicitly) observed. Besides the outer-bar morphology, and an extension of the suggestion above, the inner-bar behaviour depends on its response time and the variability of the wave climate. As such, the shorter residence times of the inner-bar states with respect to those of the outer bar (Chapter 2) indicate a shorter response time of the inner bar. This may cause the inner and outer bar morphologies to deform independently of each other for a given set of time-varying wave conditions. A numerical model with different initial inner-bar morphologies, and time-variant wave forcing could shed light on this aspect of morphological coupling behaviour (see also Drønen and Deigaard, 2007; Garnier et al., 2008a; Castelle and Ruessink, 2011; Tiessen et al., 2011; Smit et al., 2012). Moreover, from this, it would be interesting to assess changes in the ratio between self-organisation processes and outer-bar forced development of the inner bar (see also Castelle et al., 2010b).

Data-model integration
Bathymetric surveys of crescentic sandbar systems are scarce. Modelling the finite-amplitude behaviour of nearshore bars, however, requires correct estimates of the initial bathymetric state. I used the assimilation model XBeachWizard (Van Dongeren et al., 2008) to estimate depth variations from the video images. The intensity of the breaker zone obtained from the time-exposure images was the only source of input for the assimilation model, and proved to give uncertainties as to the high-intensity areas represented. Although previous work has been devoted to unravel how the observed foam relates to the e.g. roller dissipation (Aarninkhof and Ruessink, 2004; Alexander and Holman, 2004), further investigation into the relation between the observed foam and the measured wave properties on a natural beach would likely benefit the use of this assimilation technique at other sites with scarce amounts of data (see e.g., Haller and Catalán, 2009). Moreover, it is expected that the inclusion of multiple proxies for the bathymetry, such as wave celerity, will enhance the assimilation results (Van Dongeren et al., 2008). In fact, it may be useful to combine information from multiple remote sensing platforms (e.g., Catalán et al., 2011), such as spatially extensive wave celerity maps from X-band radar (Bell and Osler, 2011) and cross-shore wave height profiles from terrestrial laser scanners (Belmont et al., 2007; Blenkinsopp et al., 2012). With adequate use of remotely-sensed information, it will become possible to set up real-time operational nearshore model systems. Such systems could benefit lifeguards to assess swimming safety in the near future or coastal managers to better assess coastal safety and the timing of nourishments. This directly couples back to the societal relevance of alongshore sandbar variability, mentioned in Chapter 1.

Finite-amplitude behaviour and cross-shore modelling
This thesis has focussed on the alongshore variability of a double sandbar system. Although cross-shore (alongshore-uniform) bar variability was not specifically analysed herein, the effect of the outer bar on the composite sandbar system implicitly includes a cross-shore aspect. In Chapter 2 it was shown that the inner bar morphodynamics depended strongly on the outer bar state; the inner bar became more dynamic and more upstate when the outer bar reached the dissipative (D) state after a high-energetic event. During intermediate outer-bar states, however, the inner bar was generally a shore-attached terrace of which the alongshore variability was largely governed by the outer-bar morphology. Similar to this bimodal behaviour of the alongshore variability of the inner bar, Lippmann et al. (1993) observed increased cross-shore variability of the inner-bar after the disappearance of the outer bar at Duck, N.C., U.S.A.. In addition to the change in sandbar behaviour, Castelle et al. (2007b) observed abnormally high erosion rates of the beach at the Gold Coast during the outer-bar decay. This indicates the cross-shore interaction between the different morphodynamic zones in the nearshore. Moreover, this stresses the need to establish an awareness of the state of the composite sandbar system when analysing sandbar behaviour within a multi-barred system, both in the case of alongshore- as cross-shore oriented studies.

What is more, the increase in three-dimensionality in the outer bar coincides with a reduced alongshore-averaged distance between the two bars (Short and Aagaard, 1993) as the outer bar migrates onshore more rapidly than the inner bar (Ruessink et al., 2009). To what extent the reduced distance modifies sandbar coupling results of Castelle et al. (2010a,b) and the present Chapter 4 is difficult to say. In fact, recent research (Plant et al., 2006; Splinter et al., 2011) has indicated that alongshore variations in bar crest position affect the alongshore-uniform behaviour. It was found that the horizontal cell-circulation coinciding with the growth of alongshore variability facilitates onshore migration under low-energetic conditions. As such, understanding the alongshore variable behaviour will lead to improved understanding of cross-shore behaviour.

Analogously, a decrease in three-dimensionality in the outer bar coincides with offshore migration of the outer bar. This offshore migration has been suggested to be driven by the increased undertow over the bar during high-energetic events. Whether undertow leads to the straightening of the bar, however, remains unknown. The observations in Chapter 2 showed that sandbars do not necessarily straighten during storms, with large wave heights, but that obliquely incident waves play a crucial role in the straightening of the bar. The transition to LBT by means of the eTBR state highlights the role of high-angle waves and presumably the alongshore current in bar straightening. During this transition, it seemed as though the bar initially straightened and became more alongshore-uniform before migrating offshore. In the simulations of Chapter 4, where I used a 2DH non-linear model, the outer bar already showed the tendency to straighten under oblique wave incidence. Preliminary model results (Figure 5.1) show the capability of the model to straighten crescentic sandbars under moderately-energetic, obliquely incident waves. There was, however, no

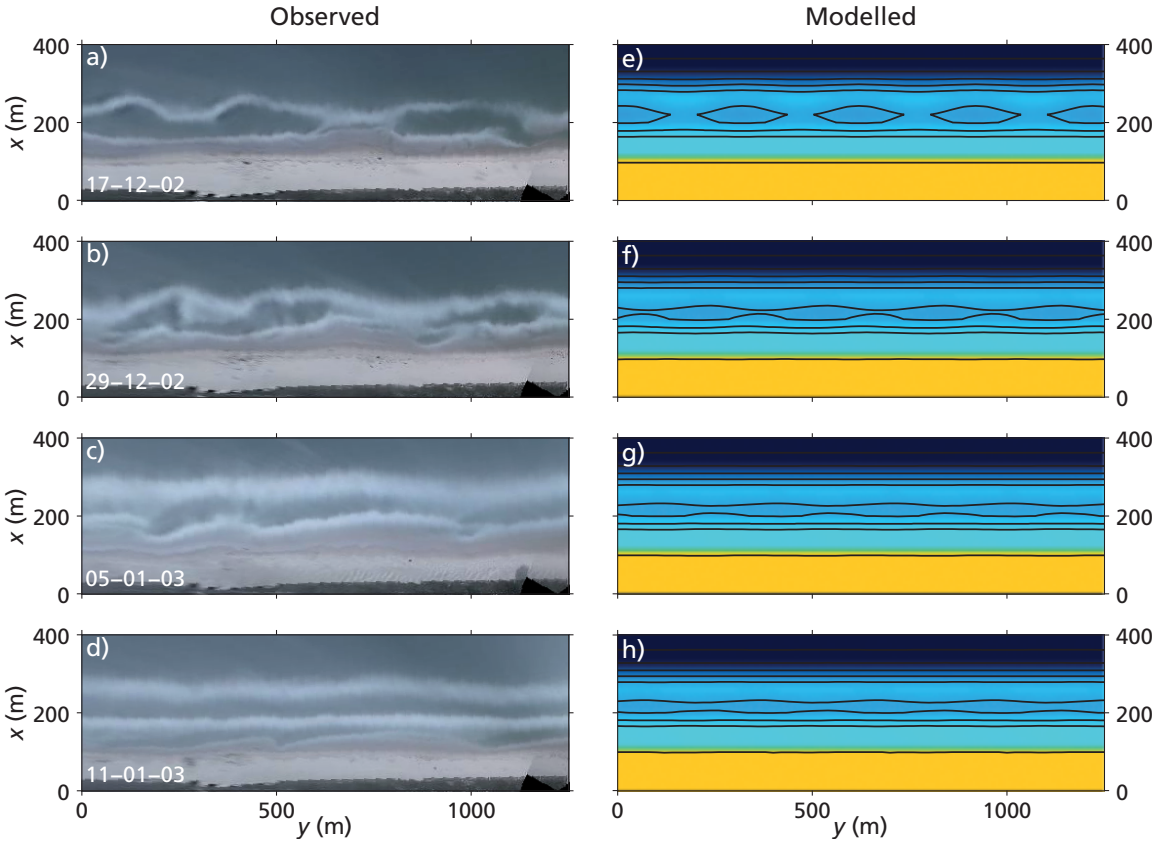

Figure 5.1 Example of observed (a-d) and modelled (e-h) morphology during bar straightening.

net migration of the outer bar, which may be a result of the exclusion of undertow. Whereas circulatory flow was found to facilitate onshore migration (Splinter et al., 2011) during downstate transitions, the gradual transition eTBR – LBT may suggest that undertow becomes more dominant when the bar straightens and cell-circulation patterns disappear, allowing the bar to migrate offshore. Process-based models that focus on cross-shore migration (e.g., Hoefel and Elgar, 2003; Ruessink et al., 2007b, 2012) or on alongshore variability (e.g., Reniers et al., 2004; Calvete et al., 2005; Drønen and Deigaard, 2007; Castelle and Coco, 2012) alone, have become quite mature. The key challenge will be to integrate both model concepts into a single model that can adequately simulate the complete dynamics of double sandbar systems.

Appendix A Application of XBeachWizard

A.1 Deriving roller energy dissipation D_r from images

The data-model assimilation method XBeachWizard permits the estimation of the nearshore subtidal bathymetry based on video-derived observations of roller dissipation D_r, wave celerity c and shoreline position (Van Dongeren et al., 2008). For this study, D_r estimates were the only available source of information and were derived from the time-exposure video images under the assumption that the high-intensity areas of wave breaking in the time-exposure video images are a proxy for D_r (see Aarninkhof and Ruessink (2004) for motivation).

Quantification of D_r from the video images, which largely followed Aarninkhof and Ruessink (2004), is described here. Firstly, a planview time-exposure image was created and rotated, such that the barlines and the alongshore axis of the image were approximately parallel. Secondly, a background intensity level I_{off} was removed from the image (Figures A.1a and f), defined as the average intensity within the offshore region where waves never broke during the study period, such that offshore areas with no wave breaking corresponded to zero intensity. Thirdly, we used a technique developed by Alexander and Holman (2004) to remove noise from the intensity signal, in which each cross-shore intensity profile is described in terms of a background intensity level I_0, a trend m_I and a Gaussian $G(x)$ type curve for each intensity peak

$$G(x) = A_G e^{-\left(\frac{x-\mu_G}{\sigma_G}\right)^2}, \tag{A.1}$$

where A_G, μ_G and σ_G represent a measure for the height, mean location and width of a dissipation peak, respectively. Different from the application of this technique by Aarninkhof and Ruessink (2004), we predefined the locations μ_G of dissipation peaks (and thus the number of peaks N_G) to coincide with the position of the extracted barlines (Section 3.2.2), leading to the following Gaussian approximation I_G of the video-based cross-shore intensity profile:

$$I_G(x) = I_0 + m_I x + G_i(x) + G_o(x), \tag{A.2}$$

where $G_i(x)$ and $G_o(x)$ are the Gaussian curves describing the dissipation peak over the inner and outer bar, respectively. For each intensity profile, I_0, m_I, and A_G and σ_G for each bar were computed using nonlinear least-squares data fitting with the Gauss-Newton method. The wave breaking related component $I_b(x)$ of $I_G(x)$ excludes the background intensity level $I_0 + m_I(x)$ and is thus given by

$$I_b(x) = G_i(x) + G_o(x). \tag{A.3}$$

Fourthly, we took heuristic measures to further improve the first estimation of the intensity maps $I_b(x, y)$, shown in Figure A.1b. I_0 and m_I sometimes contained large, sudden alongshore fluctuations (Figures A.1c and d, respectively), which would lead to an unrealistic D_r map. These alongshore fluctuations were removed by fitting a linear trend through the (despiked) values of I_0 and m_I at each alongshore position (Figures A.1c and d), and subsequently refitting Eq. (A.2) with predefined I_0 and m_I (Figure A.1e). We often found that Eq. (A.2) overestimated intensities in the outer trough. The high-intensity area landward of the inner bar, due to the visibility of sand through the water column, caused σ_{G_i} to be overestimated and, consequently, non-zero intensities in the outer trough. We therefore constrained the widths of the inner and outer dissipation peaks to maximum values of $\sigma_{G_{i,max}} = 15$ m and $\sigma_{G_{o,max}} = 30$ m (Figure A.1h), and limited the cross-shore extent of the intensity profile to be fitted to $\mu_{G_o} - \sigma_{G_{o,max}} < x < \mu_{G_i} + \sigma_{G_{i,max}}$. The maximum height of an intensity peak $A_{G_{max}}$ was set to 200 for both bars (Figure A.1i), resulting in the final $I_b(x, y)$ shown in Figure A.1j. Only images containing an outer bar with an alongshore-continuous trough were used, as the dissipation over shore-attached horns is not described well by Eq. (A.2). Visual quality control ensured the use of undistorted images (due to e.g. shadows or drops on the lens).

The final step of the preprocessing involved quantitative scaling of the corrected image intensities to obtain the roller dissipation map $D_O(x, y)$. The wave properties, measured at 2 km offshore at 18 m water depth, were transformed to the image boundary (10 m water depth) using the Battjes and Janssen (1978) wave transformation model. Each cross-shore dissipation profile $I_b(x)$ was normalised by its own standard deviation and scaled with the incoming wave energy flux to obtain the final video-derived measure of roller dissipation

$$D_O(x, y) = \left(\frac{I_b(x, y)}{\int_x \int_y I_b \mathrm{d}x\mathrm{d}y} \right) \int_y E c_g \cos\theta \mathrm{d}y, \tag{A.4}$$

where E is the wave energy, c_g is the wave group velocity, and θ is the wave angle, all at the offshore boundary of the model.

A.2 Model settings

The main parameter controlling D_r in the wave dissipation module of XBeach is the breaker parameter γ. It controls the cross-shore distribution of the breaking-wave dissipation, which is the source term for D_r. There was very limited measured depth, so there really was no clear opportunity to compare observed and modelled cross-shore dissipation patterns. We make an attempt with the only available bathymetric data (June 12, 2002) in Figure A.2, which compares alongshore-averaged video-derived D_O and modelled D_m roller dissipation for varying values of γ at different tidal stages. Note that the D_O maps were derived from 6 June 2002, the last day of wave breaking over the outer bar before the bathymetry was measured. Consequently, the computations were done with the measured wave data corresponding to the time of the

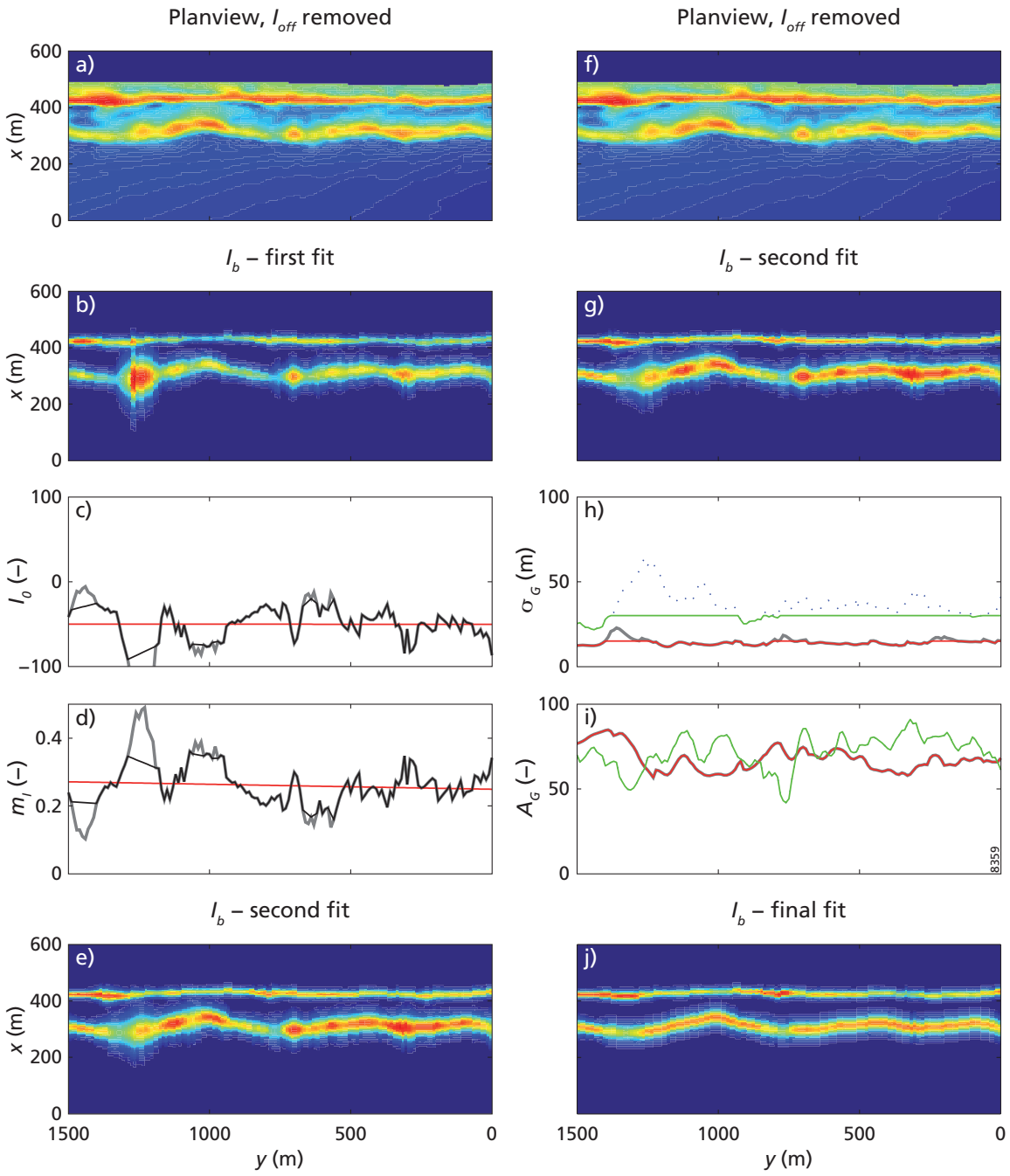

Figure A.1 Example of image preprocessing, with (a and f) the rotated planview image from 21 January 2006 05:00 GMT after removal of I_{off}, (b) the initial $I_b(x, y)$, the linear fits (solid red line) applied to the (despiked, black line) (c) $I_0(y)$ and (d) $m_I(y)$, (e and g) $I_b(x, y)$ after applying the linear fits in (c) and (d), (h) $\sigma_{G_o}(y)$ (red) and $\sigma_{G_i}(y)$ (green) after constraining the values obtained after the second fit in (g) for the outer (dots) and inner (solid black) bars, respectively (i) $A_G(y)$, and (j) the final $I_b(x, y)$. In the intensity maps, the y-axis represents cross-shore distance x (m), and dark blue (bright red) corresponds to 0 (maximum) intensity. The gray lines in (c) and (d) depict the non-despiked I_0 and m_I corresponding to (b), respectively.

images. All plots indicate an overestimated, landward (seaward) shifted D_r for the outer (inner) bar. Although each setting shows varying skill in space (inner and outer bar) and time (tide), we obtained the best results with $\gamma = 0.80$.

The model domain used for each XBeachWizard run ranged 1500 m alongshore with a grid size of $dy = 10$ m, and 600 m offshore with a grid spacing of $dx = 5$ m, up to approximately 10 m water depth. For each run we used all available images (typically about 9 per day), and for each image XBeachWizard was run for 30 minutes in stationary mode, using the measured tidal elevation z_s, root-mean-square wave height H_{rms}, peak period T_p and wave direction θ as boundary conditions. The depth $z(x, y)$ estimated at the end of these 30 minutes was used in the Kalman-filtering approach detailed in Van Dongeren et al. (2008) to estimate the starting depth for the next image. This also resulted in uncertainty estimates $\sigma(x, y)$ for each $z(x, y)$. Each run was initialised with the bathymetry of 12 June 2002, where missing data beyond the measurement area was filled with the alongshore averaged profile.

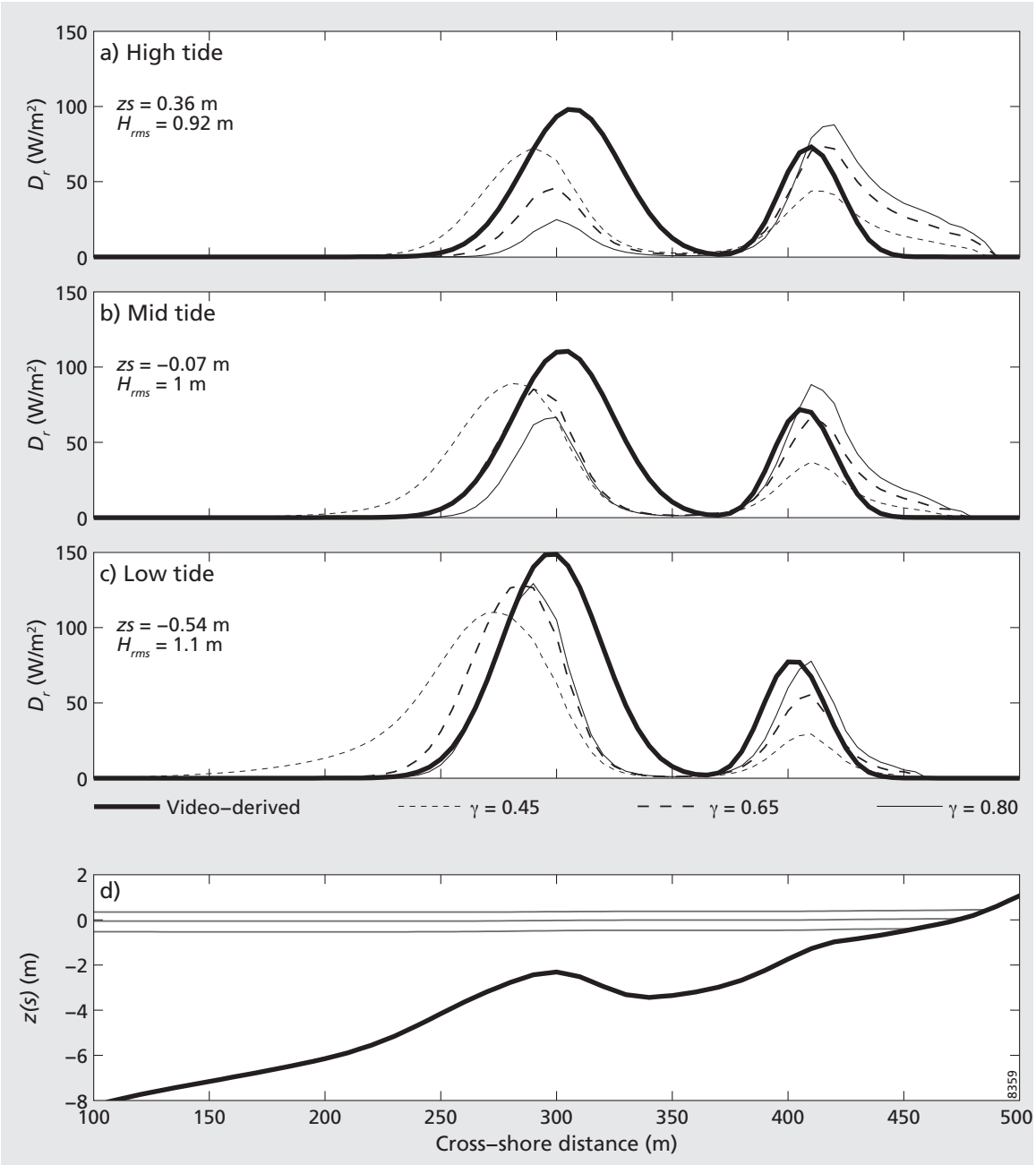

Figure A.2 Comparison of the video-derived dissipation D_O (black solid line) and computed dissipation D_m for $\gamma = 0.45$ (thin dashed line), 0.65 (thick dashed line) and 0.8 (solid line). The alongshore-averaged (over a distance of 1000 m) cross-shore dissipation profiles were compared during (a) high tide (6 June 2002 01:00 GMT), (b) mid tide (6 June 2002 04:00 GMT) and (c) low tide (6 June 2002 06:00 GMT). The alongshore-averaged cross-shore bottom profile and the three tidal water levels are shown in (d).

References

Aarninkhof, S. G. J. and B. G. Ruessink (2004), Video observations and model predictions of depth-induced wave dissipation. IEEE Transactions on Geoscience and Remote Sensing 42, 2612 – 2622.

Aarninkhof, S. G. J., I. L. Turner, T. D. T. Dronkers, M. Caljouw and L. Nipius (2003), A video-based technique for mapping intertidal beach bathymetry. Coastal Engineering 49, 275–289.

Aarninkhof, S. G. J., B. G. Ruessink and J. A. Roelvink (2005), Nearshore subtidal bathymetry from time-exposure video images. Journal of Geophysical Research 110, C06011.

Adrian, R. J., K. T. Christensen and Z.-C. Liu (2000), Analysis and interpretation of instantaneous turbulent velocity fields. Experiments in Fluids 29, 275–290.

Alexander, P. S. and R. A. Holman (2004), Quantification of nearshore morphology based on video imaging. Marine Geology 208, 101 – 111.

Allen, M. and J. Callaghan (1999), Extreme wave conditions for the South Queensland coastal region. Tech. Rep., Queensland government, Environmental Protection Agency. Available on-line: ⟨http://www.epa.qld.gov.au/register/p00361aa.pdf⟩.

Almar, R., B. Castelle, B. G. Ruessink, N. Sénéchal, P. Bonneton and V. Marieu (2010), Two- and three-dimensional double-sandbar system behaviour under intense wave forcing and a meso-macro tidal range. Continental Shelf Research 30, 781 – 792.

Armaroli, C. and P. Ciavola (2011), Dynamics of a nearshore bar system in the northern Adriatic: A video-based morphological classification. Geomorphology 126, 201–216.

Austin, M. J., T. M. Scott, J. W. Brown, J. A. Brown, J. MacMahan, G. Masselink and P. E. Russell (2010), Temporal observations of rip current circulation on a macro-tidal beach. Continental Shelf Research 30, 1149 – 1165.

Bailard, J. A. (1981), An energetics total load sediment transport model for a plane sloping beach. Journal of Geophysical Research 86, 10938–10954.

Battjes, J. and J. Janssen (1978), Energy loss and set-up due to breaking of random waves. In: Proc. 16th Int. Conf. on Coastal Engineering, ASCE, New York, 569–587.

Battjes, J. A. (1975), Modeling of turbulence in the surf zone. In: Proc. Symposium on Modeling Techniques, ASCE, 1050–1061.

Bell, P. and J. Osler (2011), Mapping bathymetry using X-band marine radar data recorded from a moving vessel. Ocean Dynamics 61, 2141–2156.

Belmont, M. R., J. M. K. Horwood, R. W. F. Thurley and J. Baker (2007), Shallow angle wave profiling lidar. Journal of Atmospheric and Oceanic Technology 24, 1150–1156.

Blenkinsopp, C. E., I. L. Turner, M. J. Allis, W. L. Peirson and L. E. Garden (2012), Application of LiDAR technology for measurement of time-varying free-surface profiles in a laboratory wave flume. Coastal Engineering 68, 1–5.

Boak, L., J. McGrath and L. Jackson (2000), IENCE – a case study – the northern Gold Coast beach protection strategy. In: Proceedings of the 27th International Conference on Coastal Engineering, ASCE, Reston, VA, vol. 276, 3710–3717.

Booij, N., R. C. Ris and L. H. Holthuijsen (1999), A third-generation wave model for coastal regions 1. model description and validation. Journal of Geophysical Research 104, 7649–7666.

Bowen, A. J. and D. L. Inman (1971), Edge waves and crescentic bars. Journal of Geophysical Research 76, 8662–8671.

Bowman, D. and V. Goldsmith (1983), Bar morphology of dissipative beaches: An empirical model. Marine Geology 51, 15 – 33.

Brander, R. W. and J. H. MacMahan (2011), Future challenges for rip current research and outreach. In: S. Leatherman and J. Fletemeyer (Eds.), Rip currents: Beach safety, physical oceanography, and wave modeling, CRC Press, Boca Raton, 1–29.

Brivois, O., D. Idier, J. Thiébot, B. Castelle, G. L. Cozannet and D. Calvete (2012), On the use of linear stability model to characterize the morphological behaviour of a double bar system. Application to Truc Vert beach (France). Comptes Rendus Geoscience 344, 277 – 287.

Browne, M., D. Strauss, R. Tomlinson and M. Blumenstein (2006), Objective beach-state classification from optical sensing of cross-shore dissipation profiles. IEEE Transactions on Geoscience and Remote Sensing 44, 3418–3426.

Calvete, D., N. Dodd, A. Falqués and S. M. van Leeuwen (2005), Morphological development of rip channel systems: Normal and near-normal wave incidence. Journal of Geophysical Research 110, C10006.

Castelle, B. and G. Coco (2012), The morphodynamics of rip channels on embayed beaches. Continental Shelf Research 43, 10 – 23.

Castelle, B. and B. G. Ruessink (2011), Modeling formation and subsequent nonlinear evolution of rip channels: time-varying versus time-invariant wave forcing. Journal of Geophysical Research 116, F04008.

Castelle, B., P. Bonneton and R. Butel (2006), Modeling of crescentic pattern development of nearshore bars: Aquitanian Coast, France. Comptes Rendus Geoscience 338, 795 – 801.

Castelle, B., P. Bonneton, H. Dupuis and N. Sénéchal (2007a), Double bar beach dynamics on the high-energy meso-macrotidal French Aquitanian Coast: A review. Marine Geology 245, 141–159.

Castelle, B., I. Turner, B. Ruessink and R. Tomlinson (2007b), Impact of storms on beach erosion: Broadbeach (Gold Coast, Australia). Journal of Coastal Research SI50, 534–539.

Castelle, B., B. G. Ruessink, P. Bonneton, V. Marieu, N. Bruneau and T. D. Price (2010a), Coupling mechanisms in double sandbar systems, Part 1: Patterns and physical explanation. Earth Surface Processes and Landforms 35, 476–486.

Castelle, B., B. G. Ruessink, P. Bonneton, V. Marieu, N. Bruneau and T. D. Price (2010b), Coupling mechanisms in double sandbar systems, Part 2: Impact on alongshore variability of inner-bar rip channels. Earth Surface Processes and Landforms 35, 771–781.

Castelle, B., V. Marieu, G. Coco, P. Bonneton, N. Bruneau and B. G. Ruessink (2012), On the impact of an offshore bathymetric anomaly on surfzone rip channels. Journal of Geophysical Research 117, F01038.

Catalán, P., M. Haller, R. Holman and W. Plant (2011), Optical and microwave detection of wave breaking in the surf zone. IEEE Transactions on Geoscience and Remote Sensing 49, 1879 –1893.

Coco, G. and D. Calvete (2009), The use of linear stability analysis to characterize the variability of multiple sandbar systems. In: Proceedings of Coastal Dynamics 2009, paper no. 53.

Coco, G. and A. B. Murray (2007), Patterns in the sand: From forcing templates to self-organization. Geomorphology 91, 271–290.

Damgaard, J., N. Dodd, L. Hall and T. Chesher (2002), Morphodynamic modelling of rip channel growth. Coastal Engineering 45, 199–221.

De Vriend, H. J. (1991), Mathematical modelling and large-scale coastal behaviour. Part 1: Physical processes. Journal of Hydraulic Research 29 (6), 727–740.

Dean, R. G. (1991), Equilibrium beach profiles: Characteristics and applications. Journal of Coastal Research 7, 53–84.

Deigaard, R., N. Drønen, J. Fredsøe, J. H. Jensen and M. P. Jørgensen (1999), A morphological stability analysis for a long straight barred coast. Coastal Engineering 36, 171–195.

Drønen, N. and R. Deigaard (2007), Quasi-three-dimensional modelling of the morphology of longshore bars. Coastal Engineering 54, 197 – 215.

Dubarbier, B. and B. Castelle (2011), Numerical modeling investigation of the influence of tide on the formation and subsequent nonlinear evolution of rip channels. Journal of Coastal Research SI64, 1018–1022.

Falqués, A., G. Coco and D. Huntley (2000), A mechanism for the generation of wave-driven rhythmic patterns in the surf zone. Journal of Geophysical Research 105, 24071–24087.

Falqués, A., N. Dodd, R. Garnier, F. Ribas, L. MacHardy, P. Larroudé, D. Calvete and F. Sancho (2008), Rhythmic surf zone bars and morphodynamic self-organization. Coastal Engineering 55, 622 – 641.

Ferrer, P., R. Certain, J. P. Barusseau and M. Gervais (2009), Conceptual modelling of a double crescentic barred coast (Leucate beach, France). In: Proceedings Coastal Dynamics 2009. Tokyo, Japan.

Garnier, R., D. Calvete, A. Falques and M. Caballeria (2006), Generation and nonlinear evolution of shore-oblique-transverse sand bars. Journal of Fluid Mechanics 567, 327–360.

Garnier, R., D. Calvete, N. Dodd and A. Falqués (2008a), Modelling the interaction between transverse and crescentic bar systems. In: C. M. Dohmen-Jansen and S. J. M. H. Hulscher, eds., River, Coastal and Estuarine Morphodynamics: RCEM 2007, vol. 2, Taylor and Francis Group, London, 931–937.

Garnier, R., D. Calvete, A. Falqués and N. Dodd (2008b), Modelling the formation and the long-term behavior of rip channel systems from the deformation of a longshore bar. Journal of Geophysical Research 113, C07053.

Garrett, C. and B. Toulany (1981), Variability of the flow through the strait of belle isle. Journal of Marine Research 39, 163 – 189.

Goldsmith, V., D. Bowman and K. Kiley (1982), Sequential stage development of crescentic bars: HaHoterim beach, southeastern Mediterranean. Journal of Sedimentary Petrology 52(1), 233–249.

Grunnet, N. M. and B. Ruessink (2005), Morphodynamic response of nearshore bars to a shoreface nourishment. Coastal Engineering 52, 119–137.

Haller, M. C. and P. A. Catalán (2009), Remote sensing of wave roller lengths in the laboratory. Journal of Geophysical Research 114, C07022.

Hino, M. (1975), Theory on formation of rip-current and cuspidal coast. In: Proc. 14th Conf. Coastal Eng., Am. Soc. Civ. Eng., 901919.

Hoefel, F. and S. Elgar (2003), Wave-induced sediment transport and sandbar migration. Science 299, 1885–1887.

Hoekstra, P., K. T. Houwman, A. Kroon, P. Van Vessem and B. G. Ruessink (1994), The NOURTEC experiment of Terschelling: process-oriented monitoring of a shoreface nourishment (1993–1996). In: A. Arcilla, M.J.F. Stive, N.C. Kraus (Eds.), Proc. 1st Int. Conf. on Coastal Dynamics '94, ASCE, New York, 402–416.

Holland, K., R. Holman, T. Lippmann, J. Stanley and N. Plant (1997), Practical use of video imagery in nearshore oceanographic field studies. IEEE Journal of Oceanic Engineering 22, 81–91.

Holman, R. (2001), Pattern formation in the nearshore. In: Seminara, G., Blondeaux, P. (Eds.), River, Coastal and Estuarine Morphodynamics, Springer-Verlag, New York, 141–162.

Holman, R. A. and A. J. Bowen (1982), Bars, bumps, and holes: Models for the generation of complex beach topography. Journal of Geophysical Research 87, 457–468.

Holman, R. A. and J. Stanley (2007), The history and technical capabilities of Argus. Coastal Engineering 54, 477–491.

Holman, R. A., G. Symonds, E. B. Thornton and R. Ranasinghe (2006), Rip spacing and persistence on an embayed beach. Journal of Geophysical Research 111, C01006.

Hom-ma, M. and C. Sonu (1962), Rhythmic patterns of longshore bars related to sediment characteristics. In: Proc. 8th Int. Conf. on Coast. Eng., ASCE, New York, 248–278.

King, C. A. M. and W. W. Williams (1949), The formation and movement of sand bars by wave action. The Geographical Journal 113, 70–85.

Klein, M. D. and H. M. Schuttelaars (2006), Morphodynamic evolution of double-barred beaches. Journal of Geophysical Research 111, C06017.

Komar, P. D. (1971), Nearshore cell circulation and the formation of giant cusps. Geological Society of America Bulletin 82 (9), 2643–2650.

Komar, P. D. (1998), Beach Processes and Sedimentation. New Jersey: Prentice Hall, 2nd edn.

Komar, P. D. and C. C. Rea (1976), Erosion of Siletz spit, Oregon. Shore and Beach 44, 9–15.

Kuriyama, Y. (2002), Medium-term bar behavior and associated sediment transport at Hasaki, Japan. Journal of Geophysical Research 107, 3132.

Lippmann, T. and R. Holman (1989), Quantification of sand bar morphology: a video technique based on wave dissipation. Journal of Geophysical Research 94, 995–1011.

Lippmann, T. C. and R. A. Holman (1990), The spatial and temporal variability of sand bar morphology. Journal of Geophysical Research 95, 11575–11590.

Lippmann, T. C., R. A. Holman and K. K. Hathaway (1993), Episodic, nonstationary behavior of a double bar system at Duck, North Carolina, U.S.A., 1986-1991. Journal of Coastal Research SI15, 49–75.

MacMahan, J., J. Brown, J. Brown, E. Thornton, A. Reniers, T. Stanton, M. Henriquez, E. Gallagher, J. Morrison, M. J. Austin, T. M. Scott and N. Senechal (2010), Mean lagrangian flow behavior on an open coast rip-channeled beach: A new perspective. Marine Geology 268, 1 – 15.

Masselink, G. and A. D. Short (1993), The effect of tide range on beach morphodynamics and morphology: A conceptual beach model. Journal of Coastal Research 9, 785–800.

Orzech, M. D., E. B. Thornton, J. H. MacMahan, W. C. O'Reilly and T. P. Stanton (2010), Alongshore rip channel migration and sediment transport. Marine Geology 271, 278–291.

Orzech, M. D., A. J. H. M. Reniers, E. B. Thornton and J. H. MacMahan (2011), Megacusps on rip channel bathymetry: Observations and modeling. Coastal Engineering 58, 890 – 907.

Pape, L., N. G. Plant and B. G. Ruessink (2010), On cross-shore migration and equilibrium states of nearshore sandbars. Journal of Geophysical Research 115, F03008.

Patterson, D. A. (2007), Sand transport and shoreline evolution, northern Gold Coast, Australia. Journal of Coastal Research SI50, 147–151.

Phillips, O. M. (1977), The dynamics of the upper ocean. Cambridge University Press, Cambridge, U.K.

Plant, N. G., K. T. Holland and R. A. Holman (2006), A dynamical attractor governs beach response to storms. Geophysical Research Letters 33, L17607.

Price, T. D., J. Rutten and B. G. Ruessink (2011), Coupled behaviour within a double sandbar system. Journal of Coastal Research SI64, 125–129.

Quartel, S. (2009), Temporal and spatial behaviour of rip channels in a multiple-barred coastal system. Earth Surface Processes and Landforms 34, 163–176.

Ranasinghe, R., G. Symonds, K. Black and R. Holman (2004), Morphodynamics of intermediate beaches: a video imaging and numerical modelling study. Coastal Engineering 51, 629–655.

Ranasinghe, R., I. L. Turner and G. Symonds (2006), Shoreline response to multifunctional artificial surfing reefs: A numerical and physical modelling study. Coastal Engineering 53, 589–611.

Reniers, A. J. H. M., J. A. Roelvink and E. B. Thornton (2004), Morphodynamic modeling of an embayed beach under wave group forcing. Journal of Geophysical Research 109, C01030.

Ribas, F., E. Ojeda, T. D. Price and J. Guillén (2010), Assessing the suitability of video imaging for studying the dynamics of nearshore sandbars in tideless beaches. IEEE Transactions on Geoscience and Remote Sensing 48 (6), 2482–2497.

Ribas, F., H. E. de Swart, D. Calvete and A. Falqués (2012), Modeling and analyzing observed transverse sand bars in the surf zone. Journal of Geophysical Research 117, F02013.

Roelvink, D., A. Reniers, A. van Dongeren, J. van Thiel de Vries, R. McCall and J. Lescinski (2009), Modelling storm impacts on beaches, dunes and barrier islands. Coastal Engineering 56, 1133–1152.

Ruessink, B., G. Ramaekers and L. van Rijn (2012), On the parameterization of the free-stream non-linear wave orbital motion in nearshore morphodynamic models. Coastal Engineering 65, 56–63.

Ruessink, B. G. and A. Kroon (1994), The behaviour of a multiple bar system in the nearshore zone of Terschelling, the Netherlands: 1965-1993. Marine Geology 121, 187–197.

Ruessink, B. G., K. M. Wijnberg, R. A. Holman, Y. Kuriyama and I. M. J. van Enckevort (2003), Intersite comparison of interannual nearshore bar behavior. Journal of Geophysical Research 108, 3249.

Ruessink, B. G., G. Coco, R. Ranasinghe and I. L. Turner (2007a), Coupled and noncoupled behavior of three-dimensional morphological patterns in a double sandbar system. Journal of Geophysical Research 112, C07002.

Ruessink, B. G., Y. Kuriyama, A. J. H. M. Reniers, J. A. Roelvink and D. J. R. Walstra (2007b), Modeling cross-shore sandbar behavior on the timescale of weeks. Journal of Geophysical Research 112, F03010.

Ruessink, B. G., L. Pape and I. L. Turner (2009), Daily to interannual cross-shore sandbar migration: observations from a multiple sandbar system. Continental Shelf Research 29, 1663–1677.

Scarfe, B., T. R. Healy and H. G. Rennie (2009), Research-based surfing literature for coastal management and the science of surfing: a review. Journal of Coastal Research 25, 539–557.

Schmidt, W. E., R. T. Guza and D. N. Slinn (2005), Surf zone currents over irregular bathymetry: Drifter observations and numerical simulations. Journal of Geophysical Research 110, C12015.

Sénéchal, N., T. Gouriou, B. Castelle, J. P. Parisot, S. Capo, S. Bujan and H. Howa (2009), Morphodynamic response of a meso- to macro-tidal intermediate beach based on a long-term data set. Geomorphology 107, 263–274.

Sénéchal, N., S. Abadie, E. Gallagher, J. MacMahan, G. Masselink, H. Michallet, A. Reniers, B. G. Ruessink, P. Russell, D. Sous, I. Turner, F. Ardhuin, P. Bonneton, S. Bujan, S. Capo, R. Certain, R. Pedreros and T. Garlan (2011), The ECORS–Truc Vert'08 nearshore field experiment: presentation of a three-dimensional morphologic system in a macro-tidal environment during consecutive extreme storm conditions 61, 2073–2098.

Shand, R. D. (2003), Relationships between episodes of bar switching, cross-shore bar migration and outer bar degeneration at wanganui, new zealand. Journal of Coastal Research 19, 157–170.

Shand, R. D., D. G. Bailey and M. J. Shepherd (1999), An inter-site comparison of net offshore bar migration characteristics and environmental conditinos. Journal of Coastal Research 15, 750–765.

Shand, R. D., D. G. Bailey, P. A. Hesp and M. J. Shepherd (2003), Conceptual beach-state model for the inner bar of a storm-dominated, micro/meso tidal range coast at Wanganui, New Zealand. In: Proceedings of Coastal Sediments 2003. Miami, U.S.A.

Short, A. (2006), Australian beach systems - nature and distribution. Journal of Coastal Research 22, 11–27.

Short, A. D. (1979), Three dimensional beach-stage model. Journal of Geology 87, 553–571.

Short, A. D. (1999), Handbook of Beach and Shoreface Morphodynamics. Chichester: Wiley.

Short, A. D. and T. Aagaard (1993), Single and multi-bar beach change models. Journal of Coastal Research SI15, 141–157.

Small, C. and R. J. Nicholls (2003), A global analysis of human settlement in coastal zones. Journal of Coastal Research 19, 584–599.

Smit, M., A. Reniers and M. Stive (2012), Role of morphological variability in the evolution of nearshore sandbars. Coastal Engineering 69, 19 – 28.

Smit, M. W. J., A. J. H. M. Reniers, B. G. Ruessink and J. A. Roelvink (2008), The morphological response of a nearshore double sandbar system to constant wave forcing. Coastal Engineering 55, 761–770.

Sonu, C. J. (1972), Field observation of nearshore circulation and meandering currents. Journal of Geophysical Research 77, 3232–3247.

Sonu, C. J. (1973), Three-dimensional beach changes. Journal of Geology 81, 42–64.

Splinter, K. D., R. A. Holman and N. G. Plant (2011), A behavior-oriented dynamic model for sandbar migration and 2DH evolution. Journal of Geophysical Research 116, C01020.

Strauss, D. and R. Tomlinson (2009), Modelling transitions between barred beach states on a straight coast. In: Proceedings Coastal Dynamics. Tokyo, Japan.

Thiébot, J., D. Idier, R. Garnier, A. Falqués and B. G. Ruessink (2012), The influence of wave direction on the morphological response of a double sandbar system. Continental Shelf Research 32, 71–85.

Thornton, E., J. MacMahan and A. Sallenger, Jr. (2007), Rip currents, mega-cusps, and eroding dunes. Marine Geology 240, 151–167.

Tiessen, M. C. H., N. Dodd and R. Garnier (2011), Development of crescentic bars for a periodically perturbed initial bathymetry. Journal of Geophysical Research 116, F04016.

Turner, I. L., S. G. J. Aarninkhof, T. D. T. Dronkers and J. McGrath (2004), CZM applications of Argus coastal imaging at the Gold Coast, Australia. Journal of Coastal Research 20, 739–752.

Turner, I. L., S. G. J. Aarninkhof and R. A. Holman (2006), Coastal imaging applications and research in Australia. Journal of Coastal Research 22, 37–48.

Van Dongeren, A., N. Plant, A. Cohen, J. A. Roelvink, M. C. Haller and P. Catalán (2008), Beach Wizard: Nearshore bathymetry estimation through assimilation of model computations and remote observations. Coastal Engineering 55, 1016 – 1027.

Van Enckevort, I. M. J. and B. G. Ruessink (2001), Effect of hydrodynamics and bathymetry on video estimates of nearshore sandbar position. Journal of Geophysical Research 106, 16969–16979.

Van Enckevort, I. M. J. and B. G. Ruessink (2003), Video observations of nearshore bar behaviour. Part 2: alongshore non-uniform variability. Continental Shelf Research 23, 513–532.

Van Enckevort, I. M. J. and K. M. Wijnberg (1999), Intra-annual changes in bar plan shape in a triple bar system. In: Proceedings Coastal Sediments '99, ASCE, New York, 1094–1108.

Van Enckevort, I. M. J., B. G. Ruessink, G. Coco, K. Suzuki, I. L. Turner, N. G. Plant and R. A. Holman (2004), Observations of nearshore crescentic sandbars. Journal of Geophysical Research 109, C06028.

Van Leeuwen, S. M., N. Dodd, D. Calvete and A. Falqués (2006), Physics of nearshore bed pattern formation under regular or random waves. Journal of Geophysical Research 111, F01023.

Vis-Star, N., H. D. Swart and D. Calvete (2008), Patch behaviour and predictability properties of modelled finite-amplitude sand ridges on the inner shelf. Nonlinear Processes in Geophysics 15, 943–955.

Webb, A. R. (2002), Statistical pattern recognition. John Wiley and Sons Ltd.

Wijnberg, K. M. and R. A. Holman (2007), Video-observations of shoreward propagating accretionary waves. In: Proceedings of the RCEM 2007, Enschede, The Netherlands, 737–743.

Wijnberg, K. M. and A. Kroon (2002), Barred beaches. Geomorphology 48, 103–120.

Wright, L. D. and A. D. Short (1984), Morphodynamic variability of surf zones and beaches: a synthesis. Marine Geology 56, 93–118.

Wright, L. D., A. D. Short and M. O. Green (1985), Short-term changes in the morphodynamic states of beaches and surf zones: an empirical predictive model. Marine Geology 62, 339–364.

Zhou, J., R. J. Adrian, S. Balachandar and T. M. Kendall (1999), Mechanisms for generating coherent packets of hairpin vortices in channel flow. Journal of Fluid Mechanics 387, 353–396.

Samenvatting

Kustnabije zandbanken zijn veelvoorkomende morfologische verschijnselen langs vele zandige, golf-gedomineerde kusten. Deze zandbanken kenmerken zich als ruggen van zand in waterdiepten tot ongeveer tien meter diep, die parallel langs de kust liggen. Afhankelijk van de golfcondities kan zich in zandbanken een afwisseling in diepte en kustdwarse positie ontwikkelen met een merkwaardige kustlangse periodiciteit, zogenoemde crescentische zandbanken. Golfgedreven stromingen zorgen ervoor dat deze zandbankpatronen voortdurend veranderen, verdwijnen of opnieuw verschijnen. Het merendeel van het huidige onderzoek heeft zich gericht op het ontstaan van crescentische patronen en in mindere mate op het gedrag van bestaande crescentische zandbanken met een eindige hoogte.

Naast hun intrigerende morfologische verschijning, zijn zandbanken ook van significant maatschappelijk belang. Golven die vanuit zee de kust naderen, breken vaak op de ondieper gelegen zandbanken, waardoor de golven een groot deel van hun verwoestende kracht verliezen voordat deze het strand en de duinen bereiken. In een systeem van twee zandbanken, met een meer landwaarts gelegen binnenste bank en meer zeewaarts gelegen buitenste bank, kan de crescentische morfologie van de buitenste bank resulteren in morfologische variaties van zowel de binnenste bank als het strand, met een periodiciteit die gekoppeld is aan de morfologie van de buitenste bank. Dit kan leiden tot hevige, gelokaliseerde strand- en duinerosie, met ernstige materiële schade als gevolg. Naast de directe verdediging tegen strand- en duinerosie door golven, vormen zandbanken een buffer van zand in de kustnabije zone. De bescherming van laaggelegen kustgebieden, zoals het westen van Nederland, omvat veelal technische ingrepen bestaande uit het onderhoud van deze natuurlijke buffer door middel van zandsuppleties. Het beter begrijpen en kunnen voorspellen van zandbankengedrag zal derhalve efficiëntere suppletieprogramma's faciliteren, zowel qua tijd als geld. Het doel van dit proefschrift is om onze kennis van crescentische patronen in een systeem van twee zandbanken te vergroten, met de nadruk op morfologische koppeling.

Om dit doel te bereiken heb ik gebruik gemaakt van negen jaar aan dagelijkse videobeelden en golf- en waterstandgegevens van een strand aan de oostkust van Australi: Surfers Paradise, The Gold Coast, Queensland, Australië. Uit deze videobeelden heb ik de zandbankposities afgeleid (hoofdstuk 2) en het voorkomen van morfologische koppeling gekwantificeerd (hoofdstuk 3). Morfologische koppeling blijkt een inherente eigenschap te zijn van het hier bestudeerde zandbankensysteem, daar de kustlangse variabiliteit van de binnenste bank gedurende 40% van de tijd gekoppeld is aan die van de buitenste bank. Deze koppeling domineert wanneer de meer zeewaarts gelegen zandbank kustlangse variaties vertoont in zowel diepte als positie. Golven met een kleine invalshoek ten opzichte van de kustlijn ($\lessapprox 30°$) en een beperkte golfhoogte ($\lessapprox 2$ m) versterken deze variaties, terwijl schuin invallende golven en grote golfhoogtes deze variaties doen verminderen en morfologische koppeling doen verdwijnen. Behalve het belang van de golfhoogte en de kustlangse variabiliteit

van de buitenste bank, blijkt vooral de invalshoek van de golven cruciaal te zijn voor het type koppeling dat zich ontwikkelt.

Door gebruik te maken van een 2DH niet-lineair morfodynamisch model, wordt in hoofdstuk 4 aangetoond dat de invalshoek van de golven in sterke mate het stromingspatroon boven de binnenste bank en dus het koppelingstype bepaalt. In het geval van een gegeven crescentische buitenste bank ontstaat er bij kleine invalshoeken een circulatiepatroon met zeewaarts-gerichte muistromen, terwijl grotere invalshoeken leiden tot het ontstaan van een meanderende kustlangse stroming. Dit laatste stromingspatroon leidt tot de ontwikkeling van het dominante koppelingstype in onze datareeks, waarbij kustdwarse ondulaties van de binnenste bank gekoppeld zijn aan de morfologie van de buitenste bank. Deze resultaten benadrukken dat de individuele zandbanken in een systeem van twee (of meerdere) zandbanken niet onafhankelijk van elkaar moeten worden beschouwd, maar dat de interactie binnen het integrale systeem in acht moeten worden genomen bij het bestuderen van een dergelijk zandbankensysteem.

About the author

Timothy Price was born to a British father and German mother on 2 July 1982 in the city of Utrecht. Timothy attended secondary school (Atheneum) at the Niftarlake College in Maarssen. After his 'gap year', during which he visited Indonesia, Australia, Mexico and the USA, Timothy started studying Physical Geography at Utrecht University. It was during these studies that he developed his interest for coastal morphodynamics and nearshore sandbars in particular. After writing a BSc thesis on subtidal sandbars, he began his MSc studies with field research focussing on the intertidal sandbars at Egmond aan Zee. This was also the first time he would get to work with (Argus) video images of the nearshore zone. During a six-month internship at the ICM in Barcelona, he continued to work on nearshore sandbars, using the Argus video system. Timothy was awarded his Master's degree in the field of coastal dynamics in September 2007. He then worked for a short while at a consultancy before starting his four-year PhD project in October 2008.

List of publications

Peer-reviewed papers

Price, T. D., Castelle, B., Ranasinghe, R., Ruessink, B.G. (submitted), Coupled sandbar patterns and obliquely incident waves. Journal of Geophysical Research.

Price, T.D. and Ruessink, B.G. (in press), Observations and conceptual modelling of morphological coupling in a double sandbar system. Earth Surface Processes and Landforms, doi:10.1002/esp.3293.

Price, T.D. and Ruessink, B.G. (2011), State dynamics of a double sandbar system. Continental Shelf Research, 31, 659–674

Castelle, B., Ruessink, B.G., Bonneton, P., Marieu, V., Bruneau, N., Price, T.D. (2010), Coupling mechanisms in double sandbar systems, Part 2: Impact on alongshore variability of inner-bar rip channels. Earth Surface Processes and Landforms, 35, 771–781

Castelle, B., Ruessink, B.G., Bonneton, P., Marieu, V., Bruneau, N., Price, T.D. (2010), Coupling mechanisms in double sandbar systems, Part 1: Patterns and physical explanation. Earth Surface Processes and Landforms, 35, 476–486

Ribas, F., Ojeda, E., Price, T.D. Guillén, J. (2010), Assessing the suitability of video imaging for studying the dynamics of nearshore sandbars in tideless beaches. IEEE Transactions on Geoscience and Remote Sensing, 48 (6), 2482–2497

Price, T.D. and Ruessink, B.G. (2008), Morphodynamic zone variability on a microtidal barred beach. Marine Geology, 251, 98–109.

Conference papers

Price, T.D., Castelle, B., Ruessink, B.G. (2012). Straightening of nearshore sandbars by obliquely incident waves: observations and modelling. Paper presented at International Conference on Coastal Engineering, 2012, Santander.

Birrien, F. Castelle, B., Dailloux, D., Marieu, V., Rihouey, D., Price, T.D. (2012). Observation video de la dynamique des mega-criossants de plage: plages d'Anglet (Pays Basque). Paper presented at XII$^{\text{èmes}}$ Journées Nationales Génie Côtier - Génie Civil, 2012, Cherbourg.

Price, T.D., Rutten, J., Ruessink, B.G. (2011), Coupled behaviour within a double sandbar system. Journal of Coastal Research, SI64 (International Coastal Symposium, 2011, Szczecin), 125–129.

Price, T.D., Ruessink, B.G. (2011). Coupled sandbar patterns: breaker lines and depth variations. Paper presented at Young Coastal Scientists and Engineers Conference, 2011, Liverpool.